ANALYTICAL MODELING OF MATERIAL CONSTITUTIVE BEHAVIORS AND PROCESS MECHANICS IN PRECISION MACHINING AND ADDITIVE MANUFACTURING

A Dissertation
Presented to
The Academic Faculty

by

Jinqiang Ning

In Partial Fulfillment
of the Requirements for the Degree
DOCTOR OF PHILOSOPHY in the
GEORGE W. WOODRUFF SCHOOL OF MECHANICAL ENGINEERING

Georgia Institute of Technology
DECEMBER 2019

ANALYTICAL MODELING OF MATERIAL CONSTITUTIVE BEHAVIORS AND PROCESS MECHANICS IN PRECISION MACHINING AND ADDITIVE MANUFACTURING

Approved by:

Dr. Steven Y. Liang, Advisor
School of Mechanical Engineering
Georgia Institute of Technology

Dr. Shreyes N. Melkote
School of Mechanical Engineering
Georgia Institute of Technology

Dr. Hamid Garmestani
School of Material Science and Engineering
Georgia Institute of Technology

Dr. Ting Zhu
School of Mechanical Engineering
Georgia Institute of Technology

Dr. Thomas Kurfess
School of Mechanical Engineering
Georgia Institute of Technology

Date Approved: [October 21, 2019]

To my wife, my parents, and my wife's parents,

Thank you for your enormous support.

ACKNOWLEDGEMENTS

First, I would like to thank my academic advisor Dr. Steven Y. Liang for providing me the support and guidance through my Ph.D. study at Georgia Tech. It has been a great experience to learn from him for his dedication to research and work with him on the advanced research topics. I will not be here without his support and guidance. I would like to thank my committee member Dr. Hamid Garmestani, Dr. Thomas Kurfess, Dr. Shreyes N. Melkote, and Dr. Ting Zhu for their valuable comments and suggestions that kept me on track.

Next, I would like to thank my former advisor Dr. Yuxiang Liu at Worcester Polytechnic Institute for his encouragement to pursue graduate study and career advice. I would like to thank Dr. Yong Huang at the University of Florida and Dr. Karl Hartwig at the Texas A&M University, Daniel E. Sievers, Dr. Peter Bocchini at Boeing, Pei Wang at AStar for providing me the research materials. I would like to thank Vihn Nguyen and Maxwell R. Praniewicz for their help in experiments. I would like to thank Dr. Yixuan Feng, Dr. Yanfei Lu, Dr. Xia Ji, Dr. Feng Li for their helpful discussion on my study and research. I would like to thank my friends at Georgia Tech and other universities for their help with inspiration and encouragement. I would also like to thank the great people in the Montgomery machining mall, the graduate office of mechanical engineering department, and university library for their generous help during my time at Georgia Tech.

Last but not least, I would like to thank my wife Xuan Ning, my parents and my wife's parents for their enormous support during my time in graduate school.

TABLE OF CONTENTS

LIST OF TABLES

LIST OF FIGURES

LIST OF SYMBOLS AND ABBREVIATIONS

AM	Additive Manufacturing
CMM	Coordinate Measurement Machine
DED	Direct Energy Deposition
DMD	Direct Metal Deposition
ECAE	Equal Channel Angular Extrusion
FEA	Finite Element Analysis
J-C Model	Johnson-Cook Constitutive Model
LDS	Laser Displacement Sensor
LENS	Laser Engineered Net Shaping
LMD	Laser Metal Deposition
MAM	Metal Additive Manufacturing
PBF	Powder Bed Fusion
PBMAM	Powder Bed Metal Additive Manufacturing
PFMAM	Powder Feed Metal Additive Manufacturing
P-L Model	Power-Law-Plasticity model
PSZ	Primary Shear Zone
SDZ	Secondary Deformation Zone
SLM	Selective Laser Melting
SPD	Severe Plastic Deformation
UFG Ti	Ultra-fine-grained Pure Titanium
XRD	X-ray Diffraction
Z-A Model	Zerilli-Amstrong constitutive model

$\dot{\varepsilon}_{xx}{}^{*}$	Elastoplastic Strain
$\dot{\varepsilon}_{xx}, \dot{\varepsilon}_{yy}$	Elastic Strains
$\dot{\varepsilon_{AB}}, \dot{\varepsilon_{int}}$	Strain Rate at Primary Shear Zone and Secondary Deformation Zone
θ_L	Dimensionless Temperature due to Heat Source
θ_s	Dimensionless Temperature due to Heat Sinks
A_i	Area of Heat Sink
C_0	Strain Rate Constant
F_c	Cutting Force
F_s	Shear Force at Primary Shear Zone
F_t	Thrust Force
$G_{xh}, G_{zh}, G_{xzh}, G_{xv}, G_{zv}, G_{xzv}$	Green's Function
H_f	Latent Heat
K_{ij}	Operation Function
N_s	Normal Force at Primary Shear Zone
Q_{cond}	Boundary Heat Loss from Conduction
Q_{conv}	Boundary Heat Loss from Convection
Q_{rad}	Boundary Heat Loss from Radiation
T_0	Room Temperature
T_i	Temperature of Heat Sink
T_l	Liquidus Temperature
T_m	Melting Temperature
T_s	Solidus Temperature
V_c	Chip Velocity
V_s	Shear Velocity

c_p	Powder Specific Heat
c_s	Solid Specific Heat
k_{AB}	Calculated Shear Stress at Primary Shear Zone using Constitutive Model
k'_{AB}	Calculated Shear Stress at Primary Shear Zone using Mechanics Model
k_g	Gas Thermal Conductivity
k_{int}	Calculated Shear Stress at Secondary Deformation Zone using Constitutive Model
k_p	Powder Thermal Conductivity
k_s	Solid Thermal Conductivity
l_{AB}	Length of Primary Shear zone
n_{eq}	Strain Hardening Constant
$\dot{q}$	Volumetric Heat Source
t_1	Depth of Cut
t_2	Chip Thickness
t_L	Layer Thickness
$\varepsilon_{AB}, \varepsilon_{int}$	Strain at Primary Shear Zone and Secondary Deformation Zone
$\varepsilon_{xx}^R, \varepsilon_{yy}^R, \varepsilon_{zz}^R, \varepsilon_{xz}^R$	Residual Strain
σ_N	Calculated Normal Stress at Secondary Deformation Zone using Mechanics Model
σ'_N	Calculated Normal Stress at Secondary Deformation Zone using Constitutive Model
$\sigma_{xx}^R, \sigma_{yy}^R, \sigma_{zz}^R, \sigma_{xz}^R$	Residual Stress
$\sigma_{xx}^{therm}, \sigma_{yy}^{therm}, \sigma_{zz}^{therm}, \sigma_{xz}^{therm}$	Thermal Stress

τ_{int}	Calculated Shear Stress at Secondary Deformation Zone using Mechanics Model
ΔT	Temperature Change
h	Enthalpy (Metal Additive Manufacturing)
h	Plastic Modulus (Metal Additive Manufacturing)
h	The Length of Secondary Shear zone/Tool-chip Contact Length (Precision machining)
h	Heat Convection Coefficient (Metal Additive Manufacturing)
$\mathrm{x}, \mathrm{y}, \mathrm{z}$	Coordinate
ε	Emissivity
θ	The angle between Resultant Force and Primary Shear Zone (Precision Machining)
θ	Dimensionless Temperature (Metal Additive Manufacturing)
λ	Friction Angle at Secondary Deformation Zone
ρ	Density
A	Yield Strength
B	Strength Coefficient
C	Strain Rate Coefficient
D	Flexural Rigidity
F	Shear Force at Secondary Deformation Zone
H	Hatch Space
N	Normal Force at Secondary Deformation Zone
P	Laser Power
R	Resultant Force (Precision Machining)
R	Distance from Heat Source (Metal Additive Manufacturing)
V	Laser Scan Velocity (Metal Additive Manufacturing)

V	Cutting Velocity (Precision Machining)
m	Thermal Softening Coefficient (Precision Machining)
m	Number of Heat Sinks (Metal Additive Manufacturing)
n	Strain Hardening Coefficient
t	Time
u	Internal Energy
v	Poisson's Ratio
w	Distortion (Metal Additive Manufacturing)
w	The Width of Cut (Precision Machining)
α	Rake Angle (Precision Machining)
α	Thermal Expansion Coefficient (Metal Additive Manufacturing)
δ	Strain Rate Constant
ε	Powder Bed Porosity (Metal Additive Manufacturing)
η	Power Absorption
κ	Thermal Diffusivity
ξ	Time-related Integration Variable
σ	Stefan-Boltzmann constant (Metal Additive Manufacturing)
ψ	Hybrid Function
ϕ	Shear Angle

SUMMARY

Manufacturing transforms raw materials into finished products, which can be broadly classified into two categories: subtractive manufacturing and additive manufacturing. Subtractive manufacturing is a process by which the products are manufactured by successive removal of materials form a solid bulk of material such as machining, grinding, polishing, etc. Subtractive manufacturing has been widely used in the manufacturing industry because of its fast process speed, high accuracy, and applicability to a wide range of materials. Additive manufacturing is a process by which the products are manufactured by layer-by-layer addition of materials from powder or wire forms of material. The powder-based metal additive manufacturing can then be classified into two categories according to different types of feedstocks, namely powder bed metal additive manufacturing (PBMAM) and powder feed metal additive manufacturing (PFMAM). PBMAM is also known as powder bed fusion (PBF), and selective laser melting (SLM). PFMAM is also known as direct energy deposition (DED), direct metal deposition (DMD), and laser engineered net shaping (LENS). Additive manufacturing can produce geometrically complex parts in a single unit or small batch with effective cost. This work studies the precision machining and metal additive manufacturing through analytical modeling with experimental validations.

Material constitutive behaviors and process mechanics are important components in the fundamental understanding of precision machining and metal additive manufacturing. Analytical modeling of the materials constitutive behaviors using process mechanics is needed to improve the quality of the produced part and optimize the cost and

efficiency of the manufacturing processes. Analytical models were developed without resorting to finite element analysis (FEA) or any simulations based on iterative calculations and thus have promising short computational time. However, the fundamental understanding of the machining process and the metal additive manufacturing process has not been fully achieved yet. The constitutive model parameters have not been fully reported in the previous works especially for new materials such as ultra-fine-grained metals, which are increasingly finding usefulness in biomedical applications due to its excellent mechanical properties and biocompatibility. Physics-based analytical models were developed for the prediction of force and temperature in precision machining and the determination of materials constitutive model parameters, specifically the Johnson-Cook model (J-C model) constants. J-C model is widely used in the modeling of machining processes because it is effective, simple, and easy-to-use. The materials strain hardening effect, strain rate hardening effect, and thermal softening effect were considered in the model. The physics-based analytical models were also developed for the prediction of temperature, thermal stress, residual stress, porosity and distortion in metal additive manufacturing processes including PBMAM and PFMAM.

In the modeling of precision machining process, an analytical methodology was developed to inversely determine the Johnson-Cook flow stress model parameters based on a chip formation model in orthogonal cutting configuration and iterative gradient search method. The materials flow stresses and cutting forces were calculated using J-C model and mechanics model. The minimization between the calculated forces yields an estimation of J-C model constants. The iterative gradient search method, specifically the Kalman Filter algorithm, was employed to ensure high computational efficiency. Another analytical

thermal model was developed for the prediction of machining temperature in orthogonal cutting configuration. The machining temperatures at two deformation zones, namely primary shear zone (PSZ) and secondary deformation zone (SDZ), were calculated by minimizing the difference between calculated flow stresses using the J-C model and mechanics model. The machining process of ultra-fine-grained pure titanium (UFG Ti) was used as a case study with developed models. The UFG Ti was prepared by severe plastic deformation (SPD) method, namely equal channel angular extrusion (ECAE), in which the raw materials underwent multiple passes through a rigid die with right angle at elevated temperature levels. The J-C model constants, machining temperatures, machining forces were calculated for the UFG Ti.

In the modeling of the metal additive manufacturing process, analytical models were developed for the prediction of temperature, molten pool behavior, powder bed porosity, part porosity, in-situ thermal deformation, thermal stress, residual stress, and part distortion respectively. Difference heat source models have been reported and employed for temperature prediction in metal additive manufacturing, including the moving point heat source, moving semi-elliptical heat source, moving uniform heat source, and moving line heat source model. However, those models were developed without the consideration of boundary heat transfer and thus were only applicable for a semi-infinite medium. An advanced analytical thermal model was developed based on the point moving heat source solution and an original heat sink solution to consider the laser heat input and boundary heat loss due to convection, conduction, and radiation. The developed model was validated in different metal additive manufacturing processes including PBMAM and PFMAM. The analytical thermal model was further developed for temperature conditions during heating

and cooling stages. The heat source model was activated during the heat stage and deactivated during cooling stage while the heat sink model was activated all the time. With the capability of temperature prediction, the in-situ thermal deformation and part porosity were predicted. A die-substrate assembly model was employed with analytical thermal model to predict the in-situ deflection during PFMAM, in which the difference of temperature, thermal stress, and strain between part and substrate were calculated. An advancing front approach was employed with the analytical thermal model to predict the part porosity due to lack-of-fusion in PBMAM. Finally, the part distortion was predicted with the calculation of residuals stress. The residual stress and residual strain were calculated from an elastoplastic relaxation procedure, also known as McDowell's algorithm. The part distortion was calculated from a surface displacement model, also known as Love's model.

The analytical models were developed without resorting to FEM or any iteration-based simulation and thus have promising short computational time. The applicability and effectiveness of the analytical modeling methodology on different manufacturing processes with various materials were studied and validated. With a complete understanding of the manufacturing processes, and developed models have improved prediction accuracy. The high computational accuracy and high prediction accuracy allow the process modeling for large scale parts, and process-parameters planning and optimization through inverse analysis, which significantly improved the usefulness of the analytical modeling in real applications.

In the future, the developed models can be employed in the study of advanced manufacturing processes such as laser-assisted manufacturing and ultrasonic vibration-

assisted manufacturing, and manufacturing processes of new materials such as other UFG metals, composite materials. The further development of those analytical models would eliminate the need for model assumptions and experimental calibration, which further improves prediction accuracy and implementation convenience, and also extends their applicability to complex processes with geometrically complex products.

CHAPTER 1. INTRODUCTION

1.1 Overview of Subtractive Manufacturing and Additive Manufacturing

Manufacturing process transforms the raw material into a finished product with desired geometry and functionality. It is the key to today's industrial competitiveness. Manufacturing processes can be broadly classified into two categories, namely subtractive manufacturing and additive manufacturing. Subtractive manufacturing is a process that successively removes materials from solid bulk material. Machining is one of the commonly used subtractive manufacturing process including turning, drilling, milling, etc. The schematic views of the machining operations are illustrated in Figure 1, in which the tool-workpiece interfaces are highlighted [1]. The machining process has fast speed, high dimensional accuracy, and a wide range of applicability to different materials. Additive manufacturing is a process that adds materials in a layer by layer manner with different feed systems. Metal additive manufacturing (MAM) is the additive manufacturing for metals, which can produce geometrically complex parts in a single unit or a small batch with effective cost due to reduced materials waste [2,3]. Laser power and metal powders are widely used in the MAM, which can be classified into two categories: powder bed metal additive manufacturing (PBMAM), and powder feed metal additive manufacturing (PFMAM), in which a piston-roller powder feed system and coaxial powder feed system are employed respectively. The schematic views of the PBMAM and PFMAM are illustrated in Figure 2 (a) and Figure 2 (b) respectively. PBMAM is also known as powder bed fusion (PBF), selective laser melting (SLM), and selective laser sintering (SLS).

PFMAM is also known as directed metal/energy deposition (DMD/DED), laser metal deposition (LMD), laser engineered net shaping (LENS) and laser cladding.

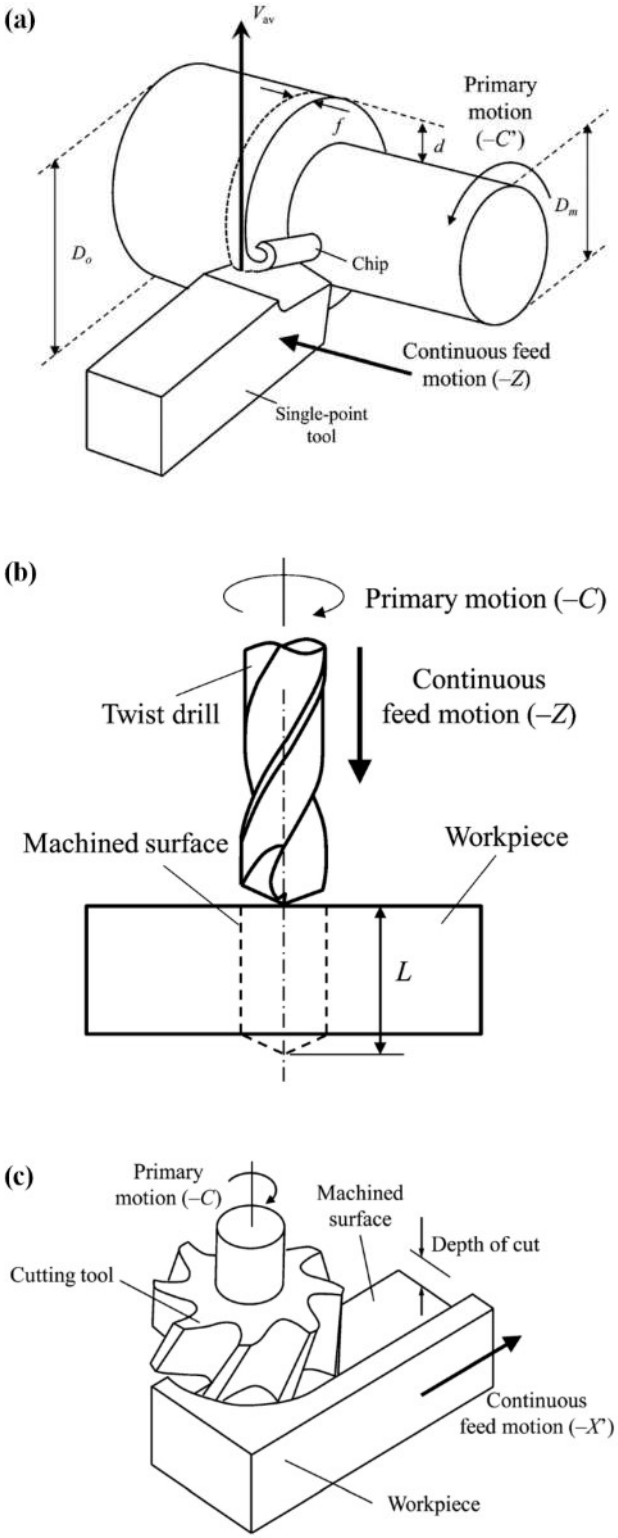

Figure 1 Schematic drawing of machining operations in (a) turning, (b) drilling, and (c) milling [1].

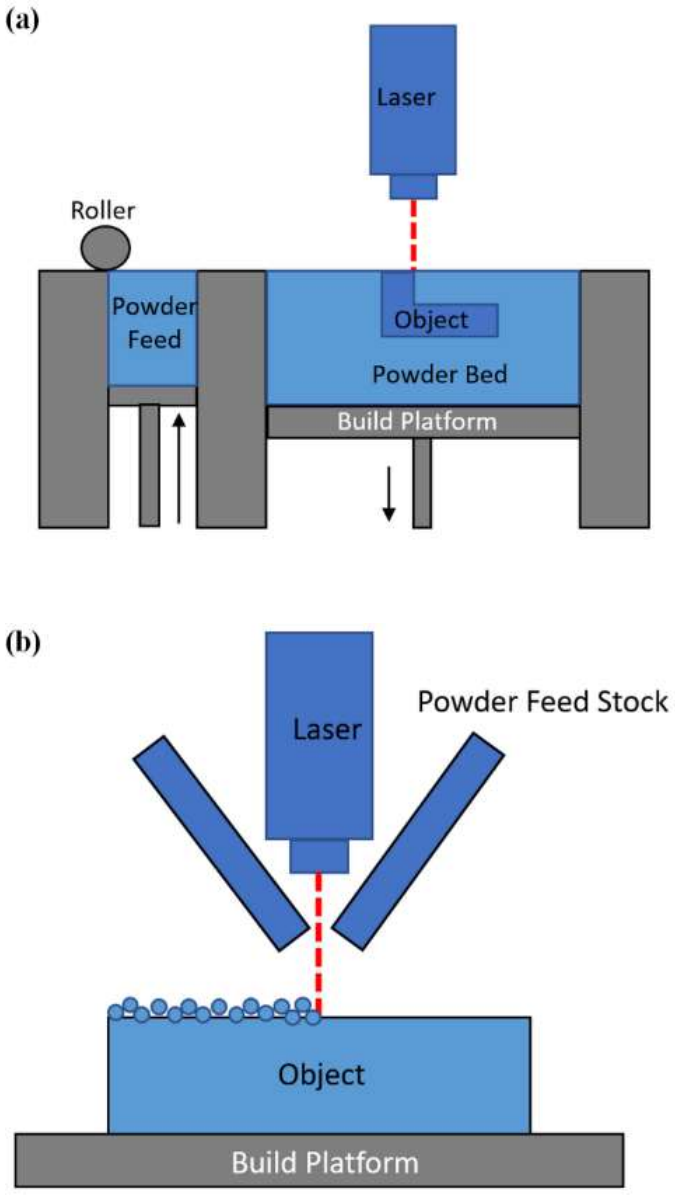

Figure 2 Schematic drawing of laser-assisted (a) powder bed metal additive manufacturing and (b) powder feed metal additive manufacturing.

The predictive capability in subtractive manufacturing and additive manufacturing allows the process planning and optimization through inverse analysis without the need for extensive experiments from trial and error. Optimization algorithms are commonly used

with those models in the inverse analysis to improve computational efficiency. Numerous works have been made in the development and improvement of models for the manufacturing processes including finite element analysis (FEA)-based numerical models and physics-based analytical models. The material constitutive relation and process mechanics were employed in the development of predictive models.

1.2 Motivation

In subtractive manufacturing, especially the machining process, numerical models and analytical models are readily available for the predictions of machining forces, machining temperatures, surface roughness, machining induced residual stress, and part distortion for the commonly used metal materials such as stainless steel, aluminum alloy, nickel alloy, titanium alloy, etc. However, the applicability of the existing models on new materials such as ultra-fine-grained metals has not been fully developed. The constitutive model parameters of those materials have not been reported. In additive manufacturing, numerical models are mainly used for the predictions of the temperature profile, residual stress, part porosity, and part distortion. The analytical models remained unavailable for the prediction of additive manufacturing processes, because of the complexity and incomplete understanding of the physics. Although numerical models have made considerable progress on the predictions of machining and additive manufacturing processes, the expensive computational cost is a major drawback, which prevents the prediction of large-scale process, and the process planning and optimization through inverse analysis. Therefore, the continuous improvement of existing analytical models and the development of new analytical models become critical.

1.3 Research Goal and Objectives

The objectives of the study are (1) to improve the fundamental understanding of materials constitutive behavior and process mechanics in precision machining and metal additive manufacturing, (2) to developed physics-based analytical models using process mechanics for the prediction of mechanical behavior of precision machining and metal additive manufacturing.

CHAPTER 2. LITERATURE REVIEW

2.1 Modeling Works in Precision Machining

Machining is a widely used subtractive manufacturing process that can achieve high dimensional tolerance with fast speed and wide range of applicability. Analytical models and numerical models were developed for the prediction of machining forces, machining temperatures, and residual stress. The review focuses on analytical modeling because of its high prediction accuracy and high computational efficiency.

2.1.1 Materials Constitutive Model

Material constitutive models describe materials behavior under various strain, strain rate, and temperature conditions. Constitutive models are needed in analytical modeling and numerical modeling of the machining process. Power-Law-Plasticity model (P-L model), Johnson-Cook constitutive model (J-C model), and Zerilli-Amstrong constitutive model (Z-A model) are commonly used constitutive models in the machining process.

P-L model is one of the simplest constitutive models considering strain and strain rate effects. This model is expressed as

$$\sigma = K\varepsilon^n \dot{\varepsilon}^m \tag{1}$$

where σ is materials flow stress, K is the strength coefficient, ε is strain, $\dot{\varepsilon}$ is strain rate, n is strain hardening exponent, m is strain rate exponent.

Z-A model is developed based on the dislocation dynamic concept. The strain, strain rate, and thermal effects are considered with thermal activation analysis in this model [4]. Materials with different crystal structures such as face-centered cubic structure (FCC), body-centered cubic structure (BCC), and hexagonal close-packed structure (HCP) have different constitutive models. The Z-A models for materials with BCC structure (Equation 2) and materials with FCC structure (Equation 3) are expressed as follows.

$$\sigma = C_0 + C_1 \exp\left(-C_3 T + C_4 T \ln(\dot{\varepsilon})\right) + C_5 \varepsilon^n \tag{2}$$

$$\sigma = C_0 + C_2 \sqrt{\varepsilon} \exp\left(-C_3 T + C_4 T \ln(\dot{\varepsilon})\right) \tag{3}$$

where C_0 to C_5 and n are six materials constants, σ is material flow stress, ε is strain, $\dot{\varepsilon}$ is strain rate. The typical BCC metals at room temperature are iron, chromium, niobium, vanadium, etc.; the typical FCC metals at room temperature are aluminum, copper, lead, nickel, platinum, silver, etc.

J-C model is one of the constitutive models widely used in analytical modeling of force, temperature, and residual stress in machining because it is effective, simple and easy-to-use. J-C model is a semi-empirical model that predicts materials flow stress at high strains, high strain rates, and elevated temperatures with considerations of strain hardening effect, strain rate hardening effect, and thermal softening effect [5]. J-C model is expressed as the following.

$$\sigma = (A + B\varepsilon^n)\left[1 + C\ln\left(\frac{\dot{\varepsilon}}{\dot{\varepsilon}_0}\right)\right]\left[1 - \left(\frac{T - T_r}{T_m - T_r}\right)^m\right] \tag{4}$$

where A, B, C, m, n are five materials constants. A is the yield stress, B is the strength coefficient, C is the strain rate coefficient, n is the strain hardening coefficient, m is the thermal softening coefficient. Other terms are explained in the following. σ is the materials flow stress; ε is the plastic strain; $\dot{\varepsilon}$ is the plastic strain rate; $\dot{\varepsilon_0}$ is the reference plastic strain rate; T is the temperature of the workpiece material; T_r is the reference temperature; T_m is the material melting temperature.

Different methodologies have been developed to identify the constitutive model constants. Those approaches can be broadly classified into three categories, namely experimental method, numerical method, and analytical method. Split Hopkinson Pressure Bar (SHPB) test is a commonly used experimental method in the identification of constitutive model constants [6], in which quasi-static tests under different temperatures and dynamics tests at different strain rates are conducted [7-9]. As shown in Figure 3, a stress wave is caused by a strike impacting at the far end of the incident bar. This compressive wave propagates through the bar causing fully elastic deformation. When the wave reaches the end of the incident bar, the wave is partially transmitted into the specimen causing plastic deformation and partially reflected as a tensile wave, and partially transmitted into the transmitter bar. Flow stresses are investigated at various strains, strain rates, and temperatures. Constitutive model constants are characterized by the flow stresses, strain rates, and temperatures recorded from experiments. The main drawback of experimental approaches is the requirement of the complex and costly experimental system.

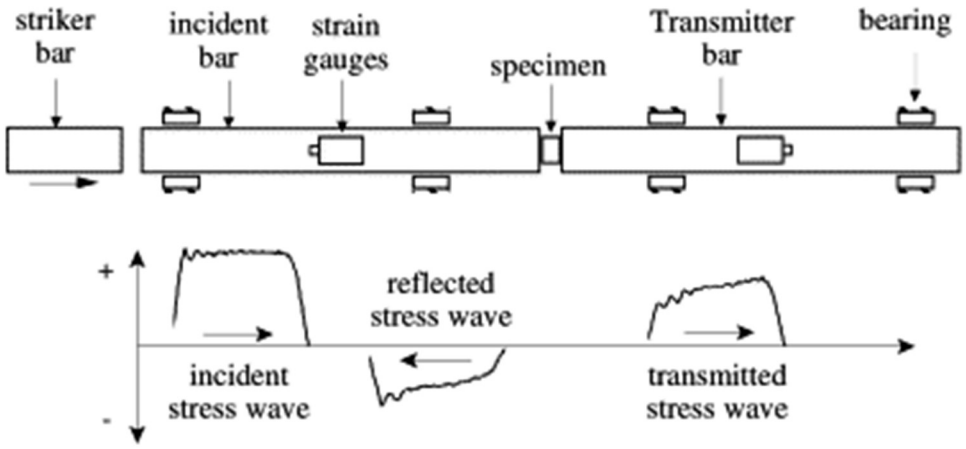

Figure 3 Schematic drawing of SHPB test setup and stress wave propagation [7].

Numerical models were employed in the determination of constitutive model constants. Majzoobi et al. presented an approach combining experimental tensile test and FEA-based numerical modeling with a comparison on specimen deformation profile to identify the constitutive model constants [10,11]. Dorogoy et al. presented another approach combining experiment and FEA-based numerical modeling to identify the constitutive model constants using shear compression specimen [12]. Similar approaches were developed to identify the constitutive model constants in the machining process [13-15], in which the machining force, machining temperature, residual stress, and chip morphology were fully or partially used for comparison between experimental measurement and modeling results. The machining forces, temperature distribution, residual stress, and chip morphology could be measured by a piezoelectric dynamometer, thermal imaging (infrared) camera, thermocouple, x-ray diffraction, and micrometer respectively. Although numerical models eliminate the need for complex and expensive experiments under various process conditions, the expensive computational cost is still the major drawback.

Analytical models were employed in the determination of constitutive model constants. A chip formation model was developed and presented in the orthogonal cutting configuration by Oxley based on the process mechanics of the machining process [16]. Özel et al. developed an analytical model to inversely identify the constitutive model constants based on experimental measurements of machining forces and chip thickness [17]. The interfacial friction between chip and tool rake face was considered as improvement to the original chip formation model. Tounsi et al. developed another analytical model to inversely identify the constitutive model constants based on the experimental measurement of strains, stresses, and temperatures [18]. The least-square approximation technique was employed to improve the computational efficiency of the developed model. Close agreements were reported on the identify constitutive model constants from analytical models upon validation to the experimental results from SHPB tests. The analytical models have high prediction accuracy with significant computational advantages, comparing to numerical models.

2.1.2 Force Modeling in Orthogonal Machining

Analytical models were developed for the prediction of machining forces based on the chip formation models. The important parameters in the orthogonal cutting process including shear angle ϕ, and strain-rate constants C_0 and δ were determined for the calculation of machining forces. As shown in Figure 4, C_0 is the ratio of shear plane length to the thickness of the primary shear zone ($l/\Delta s_2$) and δ is the ratio of the thickness of secondary shear zone to chip thickness ($\Delta s_1/t_2$). The cutting process variables including cutting speed, depth of cut, width of cut, and workpiece material properties of density, thermal conductivity, specific heat, and materials melting temperature were used as model

inputs. The constitutive model was used for the calculation of flow stresses. The following assumptions were enforced in the chip formation model: (1) a perfectly sharp cutting tool, (2) plane strain condition and steady-state condition, (3) straight-line represented primary shear zone (PSZ) plane near the center of the shear plane field, (4) uniform strains and uniform temperatures at the primary shear zone (PSZ) and the secondary deformation zone (SDZ). The schematic drawing of the chip formation model in the orthogonal cutting configuration is illustrated in Figure 5, where α is the rake angle, ϕ is the shear angle, λ is average friction angle at tool chip interface, θ is the angle between resultant cutting force R and primary shear zone AB. t_1 t_2 are the depth of cut and the chip thickness respectively. V, V_s, V_c are cutting velocity, shear velocity and chip velocity respectively. w is the cutting width that is not shown.

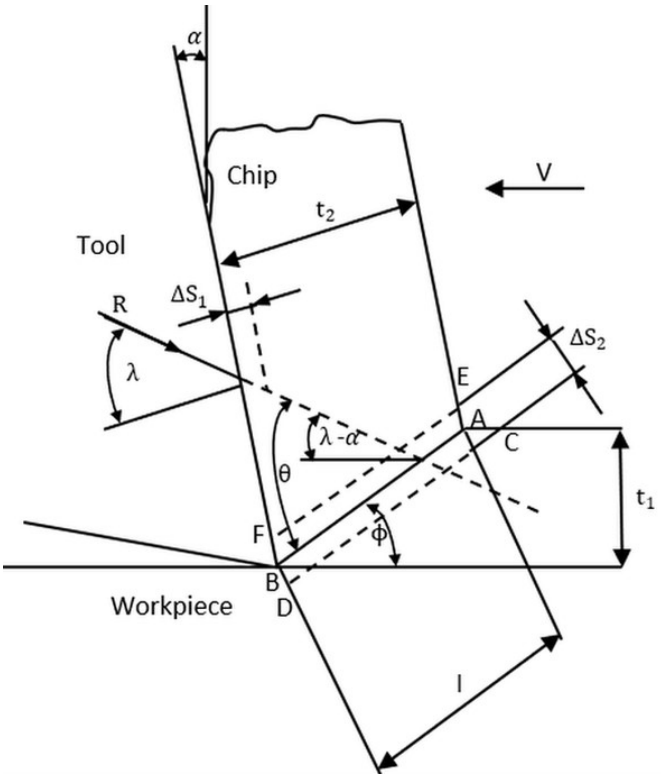

Figure 4 Parallel side shear zone model.

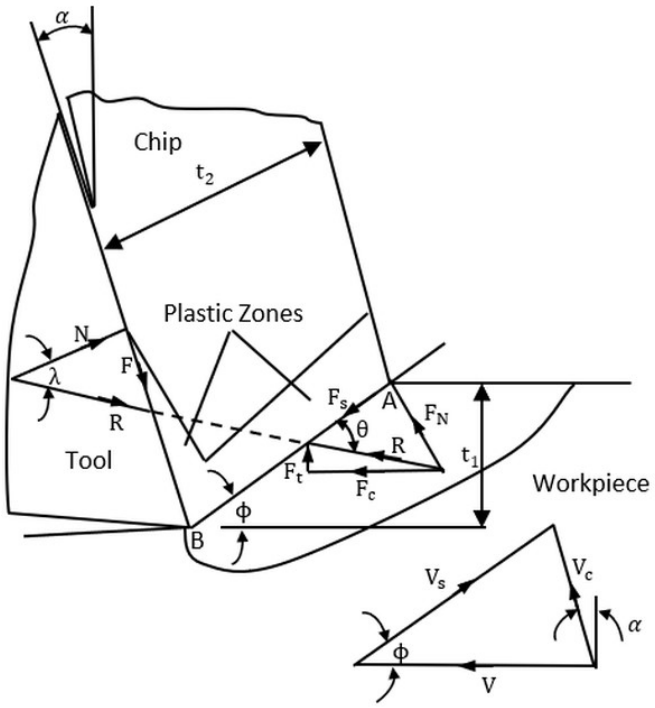

Figure 5 Schematic drawing of chip formation model in the orthogonal cutting configuration.

Lalwani et al. modified the chip formation model in the machining force prediction [19]. J-C model was employed for the calculation of materials flow stress. The shear angle and two strain-rate constants were inversely determined with iterations by minimizing the difference between stresses calculated using process mechanics and the J-C model at two deformation zones. The machining temperatures were calculated as intermediate variables. Adibi-Sedeh et al. modified the chip formation model by explicitly solving the temperature at PSZ based on the energy balance between plastic work due to shear deformation and generated heat [20]. The calculated temperatures were used in the prediction of machining forces. Machining temperatures at two deformation zones were calculated as intermediate variables using the modified chip formation model. However, the machining temperatures

at two deformation zones were calculated as constant values based on the model assumption.

2.1.3 Thermal Modeling in Orthogonal Machining

Komanduri et al. developed an analytical model to predict the temperature distribution at the chip formation zone by modeling two heat sources at PSZ and SDZ respectively [21-23]. The heat source due to the shear deformation at PSZ was considering using a moving heat source solution with boundary conditions defined by appropriate image sources as illustrated in Figure 6. The heat source due to the friction between tool and chip at SDZ was considering based on the equivalence between two heat source solutions, namely a moving heat source in the chip and stationary heat source in the tool as illustrated in Figure 7.

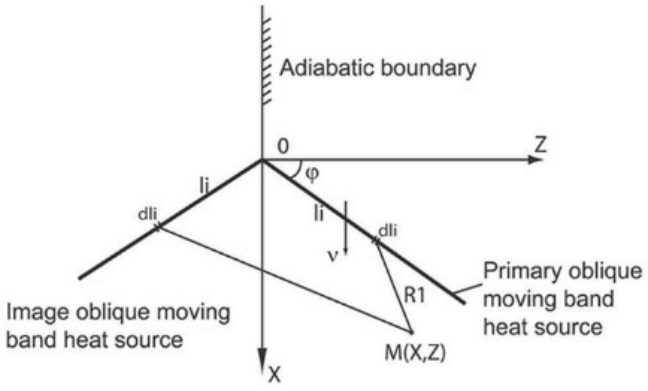

Figure 6 Heat transfer model for the shear plane heat source in a semi-infinite medium with an appropriate image heat source [24].

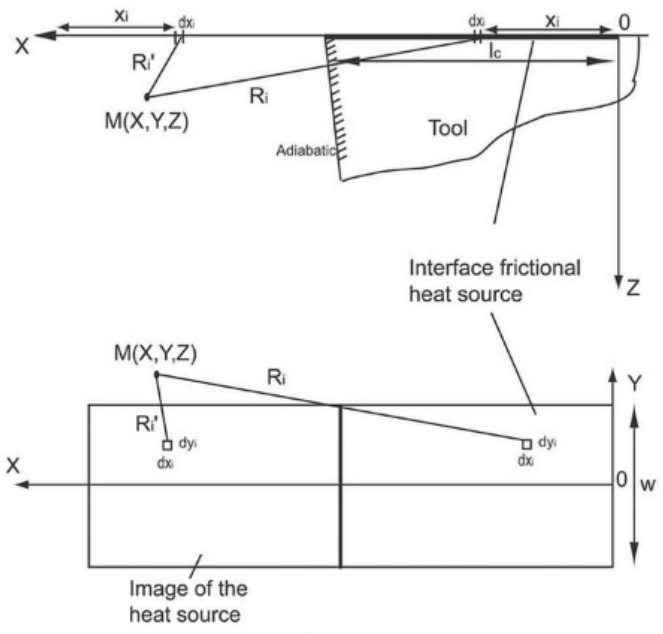

Figure 7 Heat transfer model for the frictional heat source at SDZ (top) on the chip side as a moving band heat source and (bottom) on the tool side as a stationary rectangular heat source [24].

Karpat et al. employed the analytical heat source model in the prediction of machining temperatures and machining forces [24]. An improved model was developed considering the influences of tool flank wear in the predictions of machining temperature and forces [25]. Aydin et al. compared the machining temperatures calculated from the chip formation model and heat source model [26]. Experimental validation confirmed improved prediction accuracy with the heat source model.

2.1.4 Modeling of Other Quantities in Machining

Analytical models were also developed for the prediction of chip formation, machining induced residual stress and distortion. Bai et al. presented an analytical model for the prediction of chip formation in orthogonal cutting considering the chip segregation frequency [27]. Pan et al. presented an analytical model for the prediction of residual stress

induced by the machining process [28], in which the mechanical load-induced stress and thermal load-induced stress were calculated by Boussinesq equations and Timoshenko thermoelectricity theory, the residual stress was calculated using an elastic-plastic relaxation procedure. Fergani et al. presented an analytical model for the prediction of residual stress induced deformation using a surface displacement model [29]. Recent advances have been made in the analytical modeling of laser-assisted machining and vibration-assisted machining [30].

2.1.5 Ultra-Fine-Grained Titanium

Ultra-fine-grained pure titanium (UFG Ti) is increasingly finding usefulness in lightweight engineering applications and biomedical applications [31,32]. UGF Ti is favored as medical implant material and has a great potential to replace the widely used Ti-6Al-4V alloy because of its sufficient mechanical strength, manufacturability, and biocompatibility with human tissues. UFG Ti has a yield strength (640 MPa) which is comparable to that of Ti-6Al-4V alloy (795 MPa) [33]. For comparison, coarse-grained pure titanium has a yield strength of 380 MPa. Machinability of UFG Ti is similar to that of coarse-grained pure titanium based on experimental studies of surface roughness, cutting forces, tool wear and chip morphology [34,35]. In addition, the alloying elements of aluminum (Al) and vanadium (V) are considered toxic and thus non-biocompatible with human tissues [36]. UFG Ti is commonly prepared by a severe plastic deformation (SPD) process, namely Equally Channel Angular Extrusion (ECAE) as illustrated in Figure 8.The details of ECAE can be found in the literature [37-39], in which the potential scale of the process and influence of the process conditions including process route, process

temperature, and rolling process were investigated. The analytical modeling of the machining process will use UFG Ti as a case study.

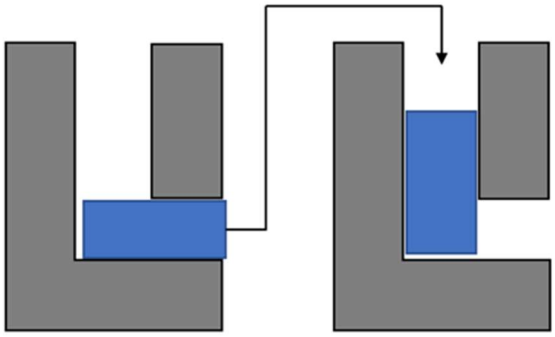

Figure 8 Schematic drawing of equal channel angular extrusion process.

2.2 Modeling Works in Metal Additive Manufacturing

Metal additive manufacturing is a widely used additive manufacturing process for metals, which can produce geometrically complex parts with effective cost. However, undesired residual stress [40], part porosity [41], and part distortion [42,43] are the frequently observed defects, which were caused by the repeated rapid heat and solidification. Numerical models and analytical models were developed for the predictions of the metal additive manufacturing processes. The review focuses on analytical modeling because of its high prediction accuracy and high computational efficiency.

2.2.1 Thermal Modeling in Metal Additive Manufacturing

Numerical models were developed for the prediction of the temperature profile in the metal additive manufacturing process. Roberts et al. developed a numerical model using element birth and death technique to predict the three-dimensional temperature profile in selective laser melting (SLM) [44]. Fu et al. developed another numerical model to predict

temperature profile and molten pool dimensions in SLM using bulk material properties and powder material properties respectively [45]. Improved accuracy was reported for predictions using powder material properties upon validation to experimental measurements on molten pool dimensions. Labudovic et al. developed a numerical model to predict the temperature profile and molten pool dimensions in DMD, in which a thin wall structure was built for analysis [46]. Hao et al. developed a numerical model to predict the temperature profile in laser cladding with inversely determined parameters for the spherical heat source [47]. The inverse modeling approach reduced the model complexity and thus improved computational efficiency. Criales et al. investigated the influence of material properties and process parameters on the temperature prediction in SLM [48]. Papadakis et al. developed a computational-reduced model with quantified heat in each scanning vector as input [49]. Improved computational efficiency was reported in the literature. Although numerical models have made considerable progress in temperature prediction in MAM, the high computational cost is still the major drawback, which prevents the temperature prediction for the large-scale part and process parameter planning with inverse analysis [49,50].

Analytical models were developed without resorting to FEA or any iteration-based simulations, which allows the fast prediction of manufacturing processes and the process planning and optimization through inverse analysis. Rosenthal developed a line moving heat source solution for the temperature prediction in welding the infinite thin plate [52]. Tan et al. developed an analytical model based on the line moving heat source solution to predict the temperature profile in laser cladding of thin-wall structure, in which two image heat sources were employed to transform the moving coordinate to the absolution

coordinate [53]. Van Elsen et al. summarized three moving heat source solutions based on a moving coordinate with the origin at the heat source location, namely moving point heat source, moving semi-ellipsoidal heat source, and moving uniform heat source [54]. Semi-infinite medium and isotropic, homogeneous materials were assumed. The moving heat source solutions were originally proposed by Carslaw and Jaeger [55]. Semi-analytical models were developed to address the neglection of part geometry in the aforementioned models. Peyre et al. developed a semi-analytical model to predict the temperature in DMD, in which an analytical model and a FEM model were used to predict the deposition geometry and temperature distribution respectively [56]. Yang et al. developed another semi-analytical model to predict the temperature in SLM, in which an analytical model and a FEM model were used to characterize the moving heat source and impose heat transfer boundary condition respectively [57]. However, the developed analytical models assumed the semi-infinite medium for the workpiece, which neglected the influence of part dimensions on the temperature distribution. The semi-analytical models address the neglection of part dimensions with FEM, which resulted in an unoptimized computational efficiency.

2.2.2 Porosity Modeling in Metal Additive Manufacturing

Numerical models were developed for porosity prediction in metal additive manufacturing. Bruna-Rosso et al. developed an FEA thermal model to plot the molten pool geometry on a part cross-sectional area along the scan path, from which the lack-of-fusion porosity was calculated [58]. Mukherjee et al. developed a similar FEA thermal model to plot the molten pool geometry on a part cross-sectional area normal to the scan path, from which the lack-of-fusion porosity was calculated [59]. Recent advances in

numerical modeling have taken powder size distribution and powder packing into consideration [60,61], which allows the prediction of defects such as porosity in MAM. Körner et al. presented a FEM model to investigate the single-track formation and part porosity in a 2D configuration during PBMAM, in which the powder bed packing was considered using a rain model [62]. Xiang et al. presented another FEM model to investigate the single-track formation and part porosity in 3D configuration during PBMAM, in which the powder bed packing was considered using the discrete element method [63]. Tan et al. developed a numerical model to investigate the porosity evolution in low energy regime and high energy regime in single-track scans [64]. Bayat et al. developed an FEA model to investigate the porosity evolution in multi-track/multi-layer scans [65]. Although numerical models have made considerable progress in the prediction of porosity, the expensive computational cost is still a major drawback.

Statistical methods were employed to correlate the process parameters and experimental part porosity with regression analysis. The developed regression models were used to predict the part porosity under a wider range of process parameters. AlFaify et al. performed regression analysis using ANOVA analysis to correlate the part porosity measured by metallographic analysis and process parameters of laser power, scan velocity, layer thickness and hatch space in PBMAM [66]. Tapia et al. performed a regression analysis using the spatial Gaussian method to correlate the part porosity measured by the Archimedes method and process parameters [67]. Khanzadeh et al. performed a regression analysis using the self-organizing map algorithm to correlate the part porosity measured by x-ray tomography and process parameters [68]. Garg et al. performed a regression analysis using the genetic algorithm to correlate the open porosity on the part surface and process

parameters [69]. Regression model required a large number of experimental measurements for calibration, which requires extensive experimental works and considerable cost.

Tang et al. calculated the lack-of-fusion area by plotting the transverse sectional areas of molten pool geometry on the cross-sectional area of the part. The part porosity was calculated by multiplying the lack-of-fusion region and powder bed porosity [70]. However, the powder bed porosity was adopted from literature as a constant, which neglected the powder size distribution and powder packing and thus might cause erroneous results. In addition, the molten pool dimensions were calculated by the line heat source model, as originally proposed by Rosenthal, which neglected the heat transfer boundary condition and absorption. A complete analytical model for porosity prediction in MAM is not available yet.

2.2.3 Residual Stress Modeling in Metal Additive Manufacturing

Fergani et al. presented an analytical model to predict the residual stress in metal additive manufacturing using an elastoplastic relaxation process [71]. The temperature profile and thermal stress were calculated using a moving heat source solution and thermoelasticity theory.

2.2.4 Distortion Modeling in Metal Additive Manufacturing

The predictive capability of part distortion eliminates the need for extensive experimental works with considerable cost based on trial and error. FEA-based numerical models have been widely used in the prediction of part distortion in MAM. Denlinger et al. and Biegler et al. presented similar numerical models to predict the distortion of the thin

wall structure in PFMAM [72,73]. Zaeh et al. presented another numerical model to predict the distortion of a twin-cantilever structure in PBMAM [75]. The twin-cantilever structure was favored in the distortion investigation of MAM because of its easily measurable and predictable distortion. Afazov et al. presented a computationally efficient numerical model to predict the distortion of turbine blade structure in PBMAM, in which the distortion of multiple layer deposition was calibration with experimental measurement on a twin cantilever part as a basic unit [76]. Li et al. presented another computational efficiency numerical model to predict the distortion of a thin sheet structure in PBMAM, in which the thermal-mechanical analysis was performed at microscale, mesoscale and macroscale respectively [77]. Paul et al. presented a numerical model to predict the distortion of cylindrical structure in PFMAM, in which the thermal shrinkage of the single-track scan was calculated as a basic unit [78]. Although the developed numerical models have made considerable progress in the prediction of part distortion, the expensive computational cost is still the major drawback.

2.3 Experimental Measurement in Manufacturing Processes

Experimental measurements of temperature and force in machining, and temperature, part porosity, residual stress, and part distortion in additive manufacturing were discussed in this section. The experimental techniques were summarized and evaluated in detail as given in Table 1. Those methods can be broadly classified as follows: destructive method/non-destructive method, contact method/non-contact method, in-situ measurement/post-process measurement. The challenges in the machining temperature measurement are the complex contact phenomena at the tool-workpiece interface and restricted accessibility during the high-speed process. Machining forces are easily

measurable but affected by the vibration during the process [79]. The challenges in the temperature measurement in metal additive manufacturing are the restricted accessibility inside the part and elevated temperature levels [80]. X-ray diffraction is a non-destructive method for surface measurement but a destructive method for in-depth measurement that required the removal of the material with machining and polishing [81]. Porosity and part distortion in metal additive manufacturing are relatively easier to measure with non-contact methods [82].

Table 1 Experimental techniques in precision machining and metal additive manufacturing.

Study	Quantity	Experimental method	Comments
Precision Machining	Temperature at PSZ	Embedded thermocouple	In-situ measurement, contact method, destructive method.
		Infrared Camera	In-situ measurement, non-contact method, non-destructive method.
	Temperature at SDZ	Tool-work thermocouple	In-situ measurement, contact method, non-destructive method.
	Force	Piezoelectric Dynamometer	In-situ measurement, contact method, non-destructive method.
Metal Additive Manufacturing	Temperature profile	Embedded thermocouple	In-situ measurement, contact method, destructive method.
		Infrared Camera	In-situ measurement, non-contact method, non-destructive method.
		Microstructure analysis	Post-process measurement, non-contact method, destructive method.
	Residual stress	X-ray Diffraction	Post-process measurement, non-contact method, non-destructive method for surface measurement, destructive method for in-depth measurement.

Table 1 continued.

Metal Additive Manufacturing	Part porosity	Metallographic analysis	Post-process measurement, non-contact method, destructive method.
		X-ray computed tomography	Post-process measurement, non-contact method, non-destructive method.
		Ultrasonic technique	Post-process measurement, non-contact method, non-destructive method.
		Density measurement	Post-process measurement, contact method, non-destructive method.
	Part distortion	Coordinate measurement machine	Post-process measurement, contact method, non-destructive method.
		Laser displacement sensor	In-situ measurement, non-contact method, non-destructive method.
		Digital Image Correlation	In-situ measurement, non-contact method, non-destructive method.

CHAPTER 3. ANALYTICAL MODELING OF PRECISION MACHINING

3.1 Inverse Identification of Material Constitutive Model Parameters

This section presented an inverse methodology for the identification of material constitutive parameters, specifically J-C model constants. The presented methodology was developed based on the analytical modeling of the machining process in orthogonal cutting configuration, as illustrated in Figure 9, where α and ϕ denote shear angle and tool rake angle respectively. The following assumptions were enforced in the machining model: plane strain condition, steady-state condition, perfectly sharp cutting tool.

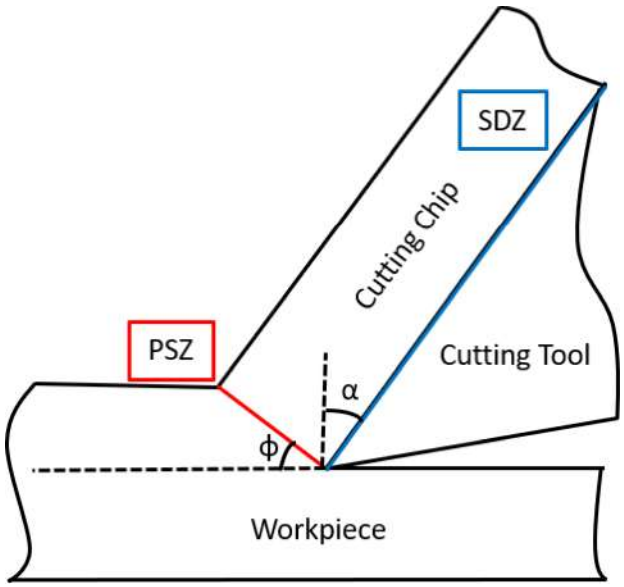

Figure 9 Schematic drawing of orthogonal cutting.

The chip formation model was widely used in the prediction of the machining process in the orthogonal cutting configuration as shown in Figure 10, in which the

machining forces were model outputs, the machining temperatures were intermediate variables. The iterative calculations resulted in a nonoptimal computational efficiency.

A modified chip formation model was employed in the prediction of machining forces, in which the machining temperature was explicitly solved from the energy balance equation. The J-C model constants were inversely determined by minimizing the difference between calculated machining forces and experimental machining forces. The algorithm of the inverse identification of J-C model constants with machining force measurement is shown in Figure 11. The materials properties, process parameters, a given set of J-C model constants were model inputs. The cutting force and thrust force were model outputs. The set of J-C model constants were chosen with the minimal difference from machining force comparison.

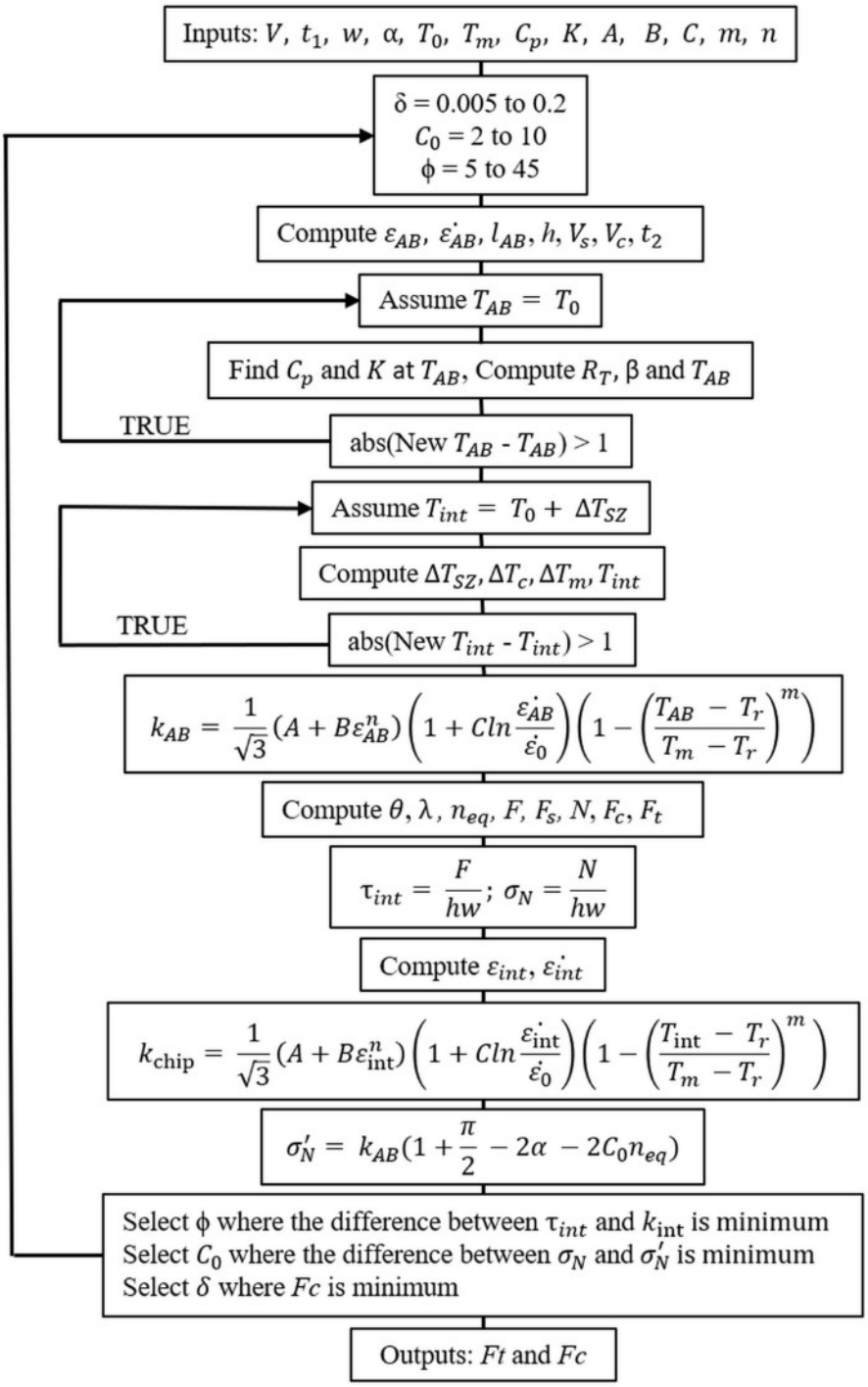

Figure 10 Algorithm of the chip formation model.

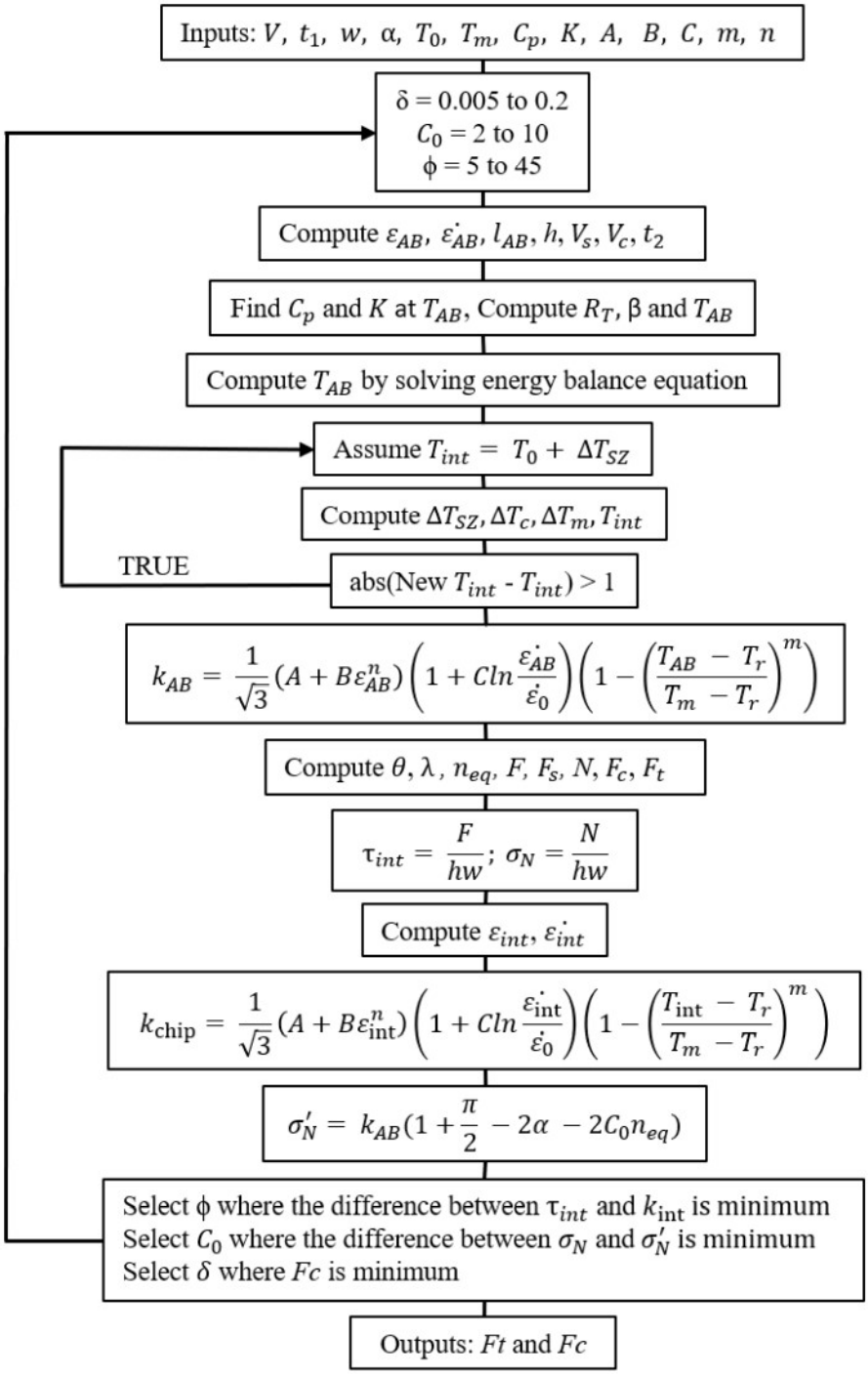

Figure 11 Algorithm of modified chip formation model with primary shear zone temperature calculated using the energy balance equation.

The presented model was validated with AISI 1045 steel and 42CrMo4 steel. The machining process conditions were adopted from literature as given in Table 2, where e

denotes experimental value, c denotes calculated value. The inversely identified J-C model constants were validated to those measured from SHPB tests. Close agreements were observed upon validation as illustrated in Table 4. In addition, the calculated J-C model constants were validated in the machining force prediction under different process conditions as illustrated in Figure 12 and Figure 13, where Fce, Fcc, Fte, Ftc denote experimental cutting force, experimental thrust force, calculated cutting force, calculated thrust force respectively. Good agreements were observed from the force validation.

Table 2 Orthogonal cutting conditions and process variables at the primary shear zone and secondary deformation zone of AISI 1045 steel (w = 1.2mm) [26].

Test	V(m/min)	t_1 (mm)	Fc^e(N)	Ft^e(N)	Fc^c(N)	Ft^c(N)	$T_{AB}{}^c$(°C)	T_{int} ^{c}(°C)
1	200	0.15	-7	607	500	590.06	397.69	339.53
2	200	0.15	5	583	402	484.84	228.81	282.80
3	200	0.3	-7	1125	740	1069.4	630.39	331.76
4	200	0.3	5	976	493	885.09	349.29	278.64
5	300	0.15	-7	623	478	564.69	356.47	337.91
6	300	0.15	5	539	326	466.24	201.91	282.98

Table 3 Orthogonal cutting conditions and process variables at the primary shear zone and secondary deformation zone of 42CrMo4 steel (w = 3mm, α = -5°) [83].

Test	V(m/min)	t_1 (mm)	Fc^e(N)	Ft^e(N)	Fc^c(N)	Ft^c(N)	$T_{AB}{}^c$(°C)	T_{int} ^{c}(°C)
1	60	0.1	981	797	883.18	740.34	384.72	665.52
2	60	0.15	1430	960	1234.9	976.11	399.93	718.01
3	60	0.25	2052	1391	1915.9	1425.6	419.44	791.59
4	120	0.1	940	780	781.05	581.17	409.11	753.58
5	120	0.15	1300	942	1099	768.28	421.25	805.24
6	120	0.25	1761	1059	1725	1130.2	430.38	872.41

Table 4 Validation of inversely determined Johnson-Cook model constants [7, 84].

Parameter	SHPB (AISI1045)	Model (AISI1045)	SHPB (42CrMo4)	Model (42CrMo4)
A(MPa)	553.1	553	612	612
B(MPa)	600.8	600	436	436
C	0.0134	0.0134	0.008	0.008
m	1	1	1.46	1.46
n	0.234	0.234	0.15	0.15
T_m (°C)	1460	1460	1527	1527

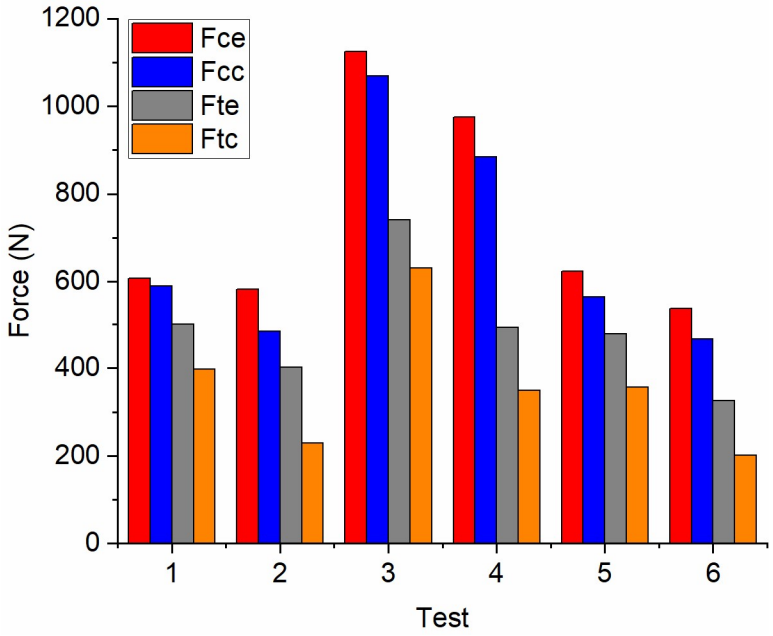

Figure 12 Experimental validation of machining forces of AISI 1045 [85].

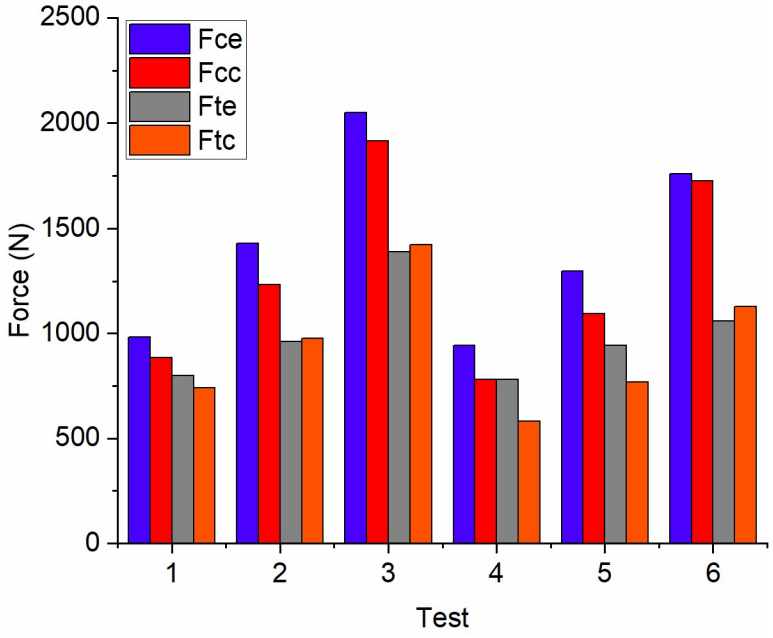

Figure 13 Experimental validation of machining forces of the 42CrMo4 alloy [85].

However, the exhaustive search methodology is still computationally expensive. Therefore, a gradient search method based on Kalman Filter was employed to improve the computational efficiency. In addition, the temperatures at the PSZ and SDZ are experimentally measured as model inputs. The algorithm of the modified chip formation model is illustrated in Figure 14. The algorithm of the gradient search method is illustrated in Figure 15.

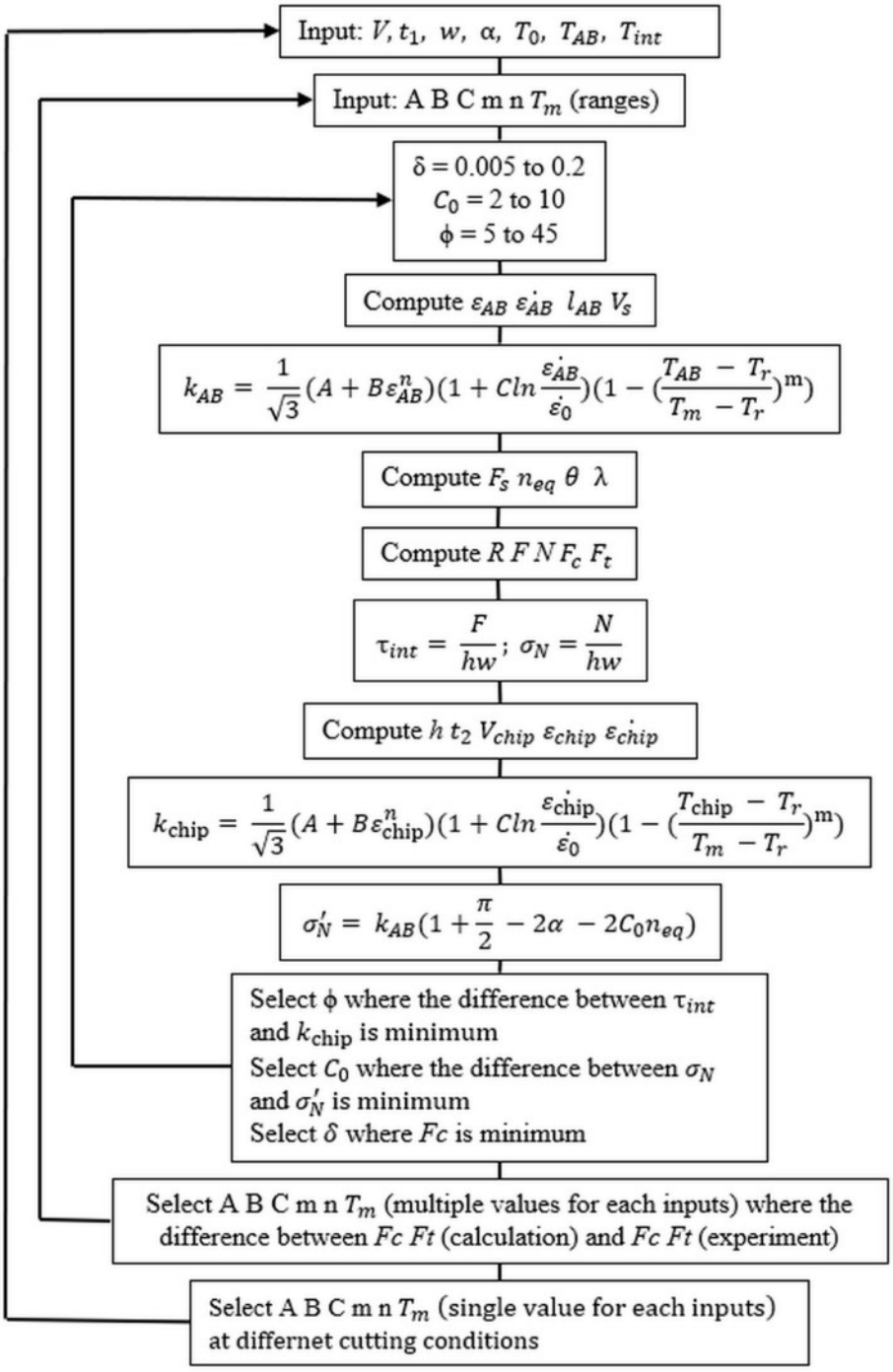

Figure 14 Algorithm of the modified chip formation model with experimental measurements of machining temperatures and forces.

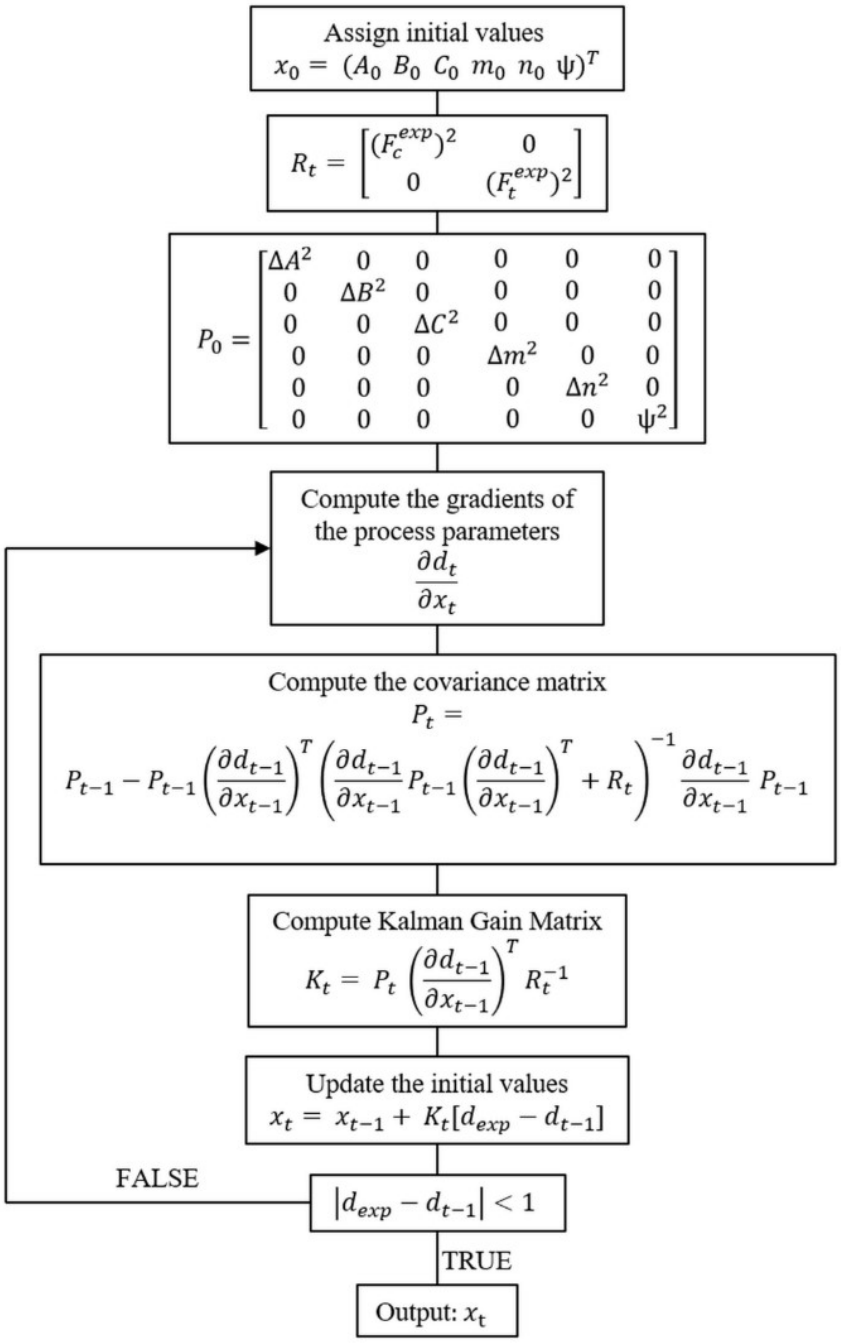

Figure 15 Algorithm of the gradient search method in the inverse identification of Johnson-Cook model constants.

The presented methodology was validated with AISI 1045 steel and AL 6082-T6 alloy. The process conditions, machining forces, and machining temperatures are given in Table 5. The convergence patterns of J-C constants of AISI 1045 steel and AL 6082-T6

alloy in the identification are shown in Figure 16 and Figure 17 respectively. The material melting temperatures were also identified, and thus material properties were not needed as model inputs, which must be obtained from extensive materials property tests.

Table 5 Orthogonal cutting condition, machining force measurement, and machining temperature measurement of AISI 1045 steel and AL 6082-T6 alloy [24, 26].

Material	Test	t_0 (mm)	w (mm)	α (degs)	V (m/s)	T_{AB} (°C)	T_{int} (°C)	F_c (N)	F_t (N)
AISI 1045	1	0.15	1.6	5	3.33	313.12	815.74	583	402
	2	0.3	1.6	-7	3.33	383.1	992.44	1125	740
	3	0.3	1.6	5	3.33	300.77	941.15	976	493
AL6082-T6	1	0.4	3	8	4	205	464	795	300
	2	0.2	3	8	6	188	493	456	204
	3	0.4	3	8	6	198	508	768	276

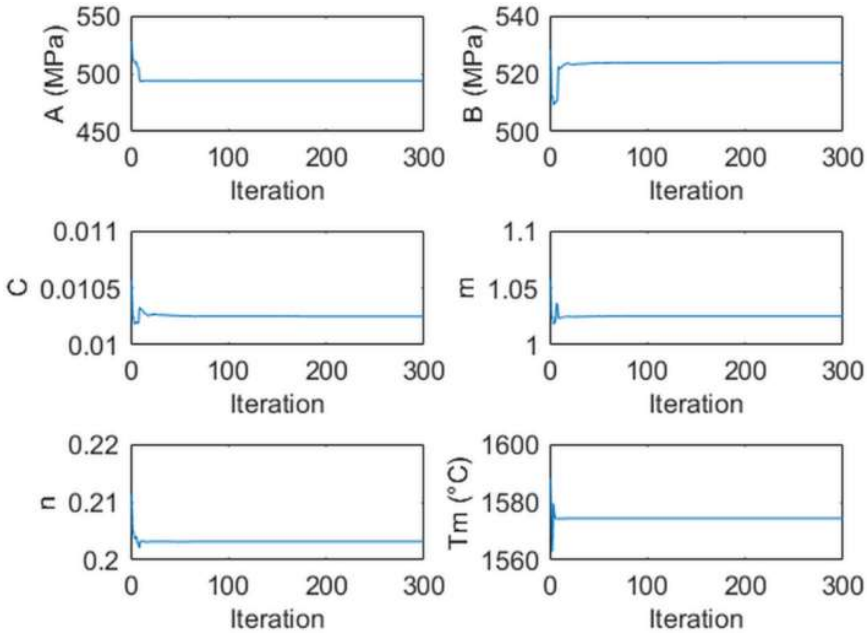

Figure 16 Convergence patterns in identifying the J-C model constants of AISI 1045 steel with test 1 in 300 iterations [86].

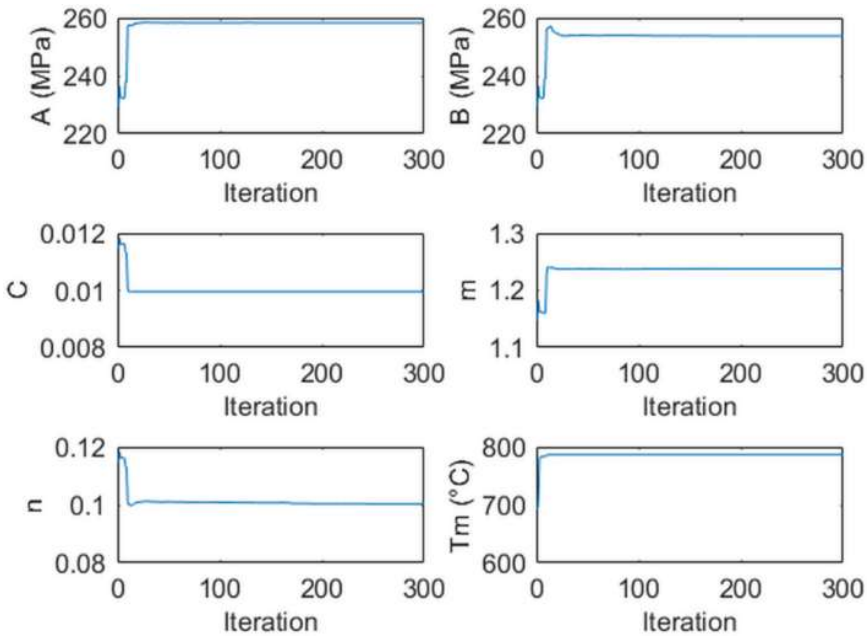

Figure 17 Convergence patterns in identifying J-C model constants of AL 6082-T6 aluminum in 300 iterations [86].

The identified J-C model constants are validated by comparing to the model constants from SHPB tests. The SHPB tests were conducted at strain ranges of 0.05 to 0.2, strain rate of 7500 1/s, and temperature ranges of 35 °C to 625 °C for AISI 1045 steel [7] and for Al 6082-T6 alloy [20]. Close agreements were observed upon experimental validation as illustrated in Figure 18, where 1, 2, 3 denote the experimental tests used for the identification of J-C model constants. SHPB denotes the J-C model constants obtained from SHPB tests for validation purposes. The blue line and red line represent the corresponding value of the J-C model constant for AISI 1045 steel and AL 6082-T6 alloy respectively.

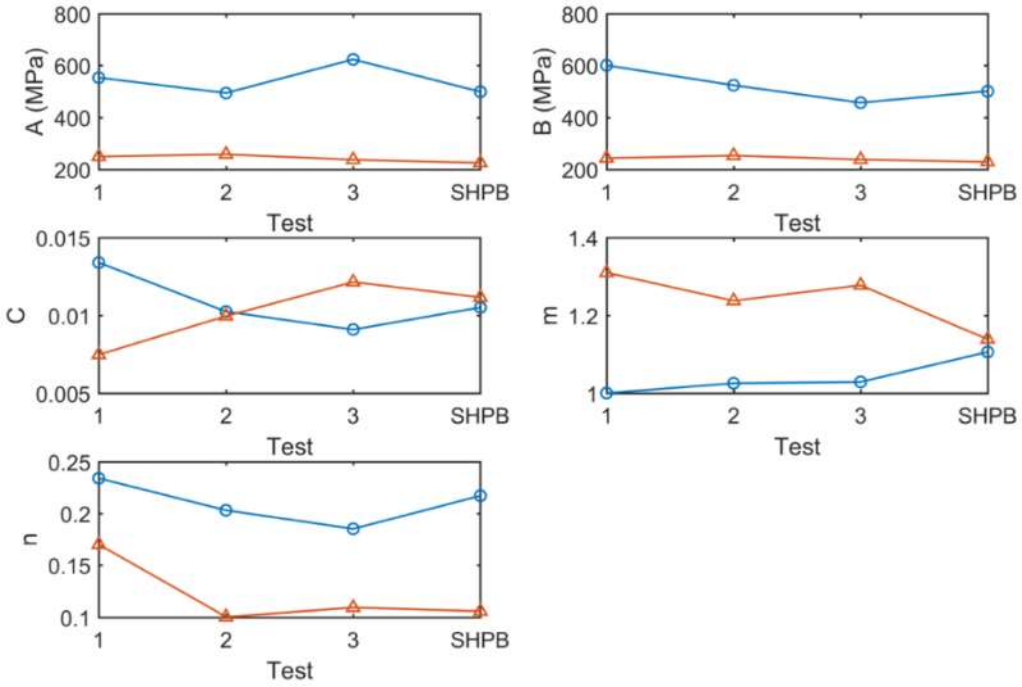

Figure 18 Identified J-C constants from different cutting tests and J-C constants from SHPB tests for AISI 1045 steel and AL 6082-T6 alloy [86].

3.2 Material Flow Stress Modeling for Machining Temperature Prediction

This section presented originally analytical models for the prediction of machining temperatures from the calculation of materials flow stress. The machining temperatures were determined based on materials constitutive model and chip formation model with easily measurable quantities of machining forces and chip thickness. The temperatures were determined when the differences between calculated shear stress using J-C model and calculated shear stresses using process mechanics model were minimal. J-C model constants from SHPB tests, cutting parameters, experimental machining forces, and chip thickness were model inputs. The average temperature at PSZ and the average temperature at SDZ were model outputs.

As shown in Figure 19, the material flow stress model used experimental cutting force and chip thickness as inputs.

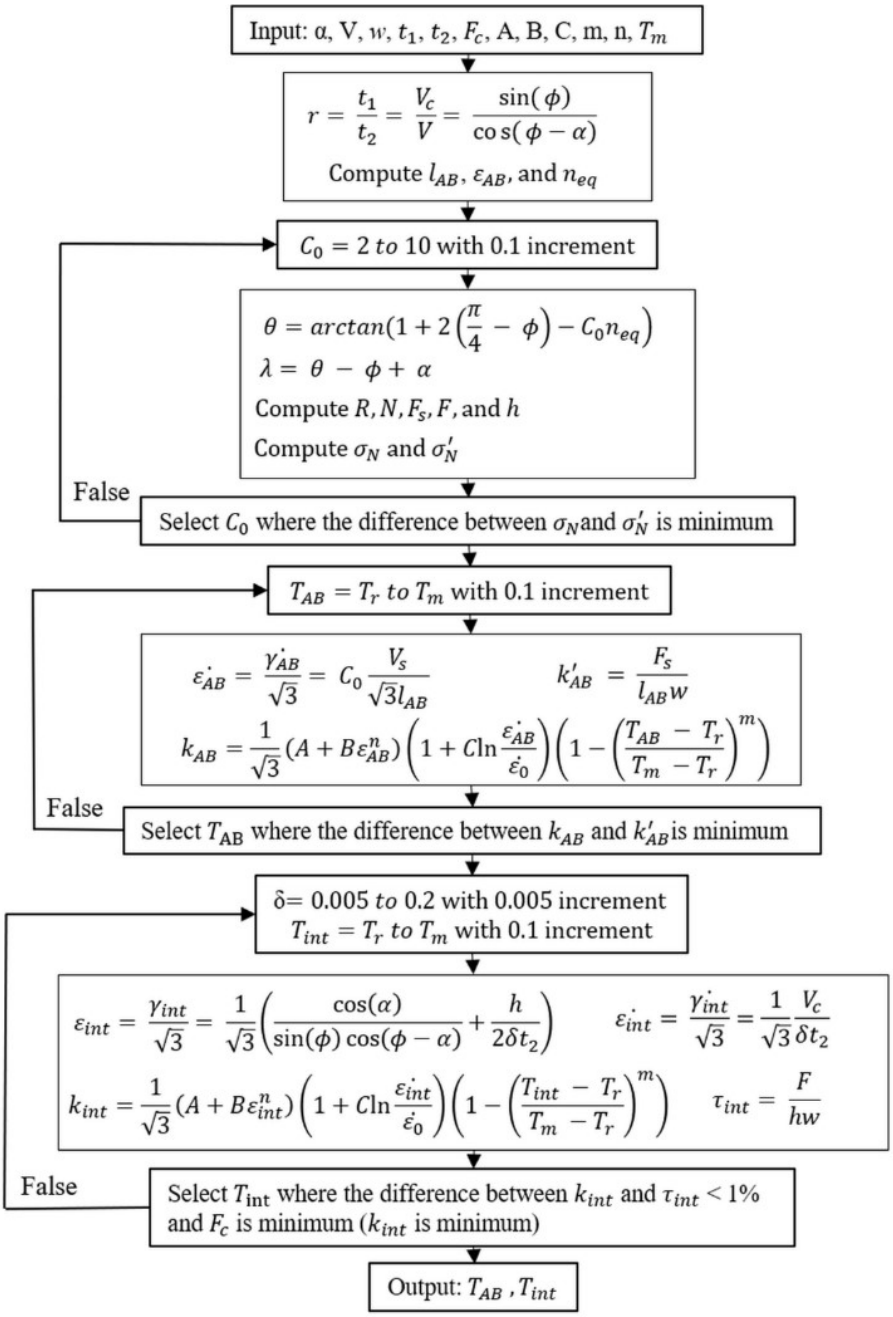

Figure 19 Algorithm of materials flow stress model using experimental cutting force and thickness.

The assumption of constant material flow rate was enforced at the chip formation zone. The two strain rate constants were calculated from the materials flow stress calculation. The shear angle is calculated as the following.

$$r = \frac{t_1}{t_2} = \frac{V_c}{V} = \frac{\sin(\phi)}{\cos(\phi - \alpha)} \tag{5}$$

where r is chip compression ratio, t_1, t_2 are the depth of cut and chip thickness respectively, ϕ, α are the shear angle and tool rake angle respectively.

To validate the presented model, the machining temperatures of AISI 1045 steel and AL 6082-T6 alloy were made in multiple tests under various cutting conditions. The cutting parameters, experimental chip thickness, and experimental machining forces are given in Table 6, where the asterisk denotes calculated values adopted from the literature.

Table 6 Orthogonal cutting condition, and machining force measurement, chip thickness measurement of AISI 1045 steel and AL 6082-T6 alloy [20, 79].

Material	Test	α (degs)	V (m/min)	w (mm)	t_1 (mm)	t_2 (mm)	Fc (N)	Ft (N)
AISI1045	1	5	200	1.6	0.15	0.424	583	402
	2	5	200	1.6	0.30	0.734	976	493
	3	5	300	1.6	0.15	0.389	539	326
	4	5	300	1.6	0.30	0.709	888	406
AL6082-T6	5	8	120	3.0	0.20	0.52*	552	384
	6	8	240	3.0	0.40	0.76*	795	300
	7	8	360	3.0	0.20	0.44*	456	204
	8	8	360	3.0	0.40	0.64*	768	276

The calculated temperatures of AISI 1045 steel and AL 6082-T6 alloy were validated to the documented values in the literature. Good agreements were observed as shown in Figure 20 and Figure 21. The deviations between the calculated temperatures and the documented temperatures were caused by experimental accuracy of machining forces and chip thickness, and the assumption of a perfectly sharp cutting tool in the presented model.

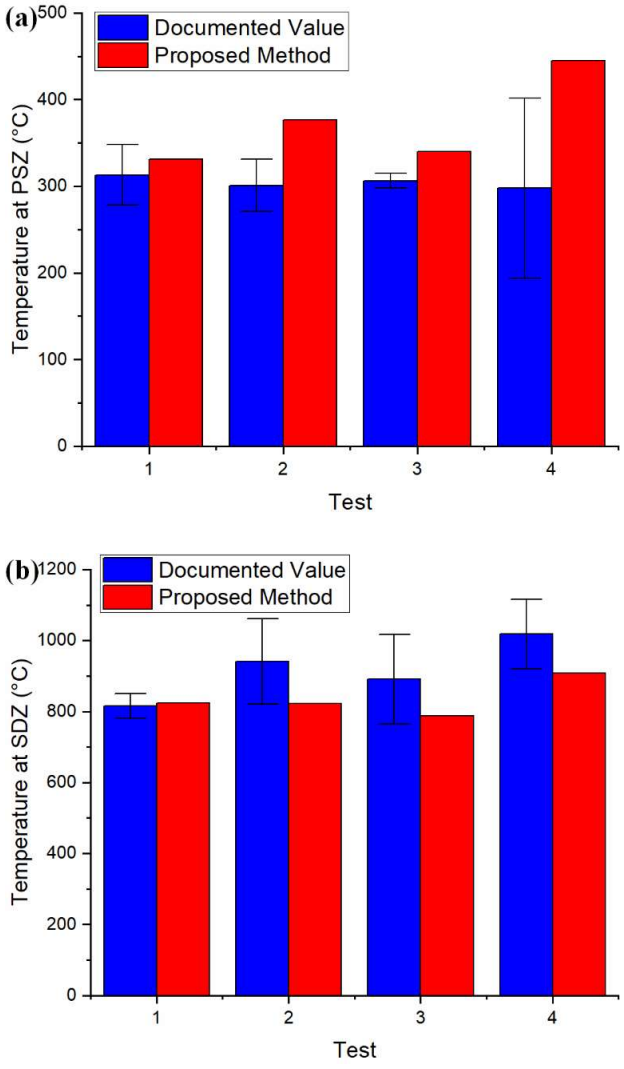

Figure 20 Validation of temperature calculation at (a) primary shear zone and (b) secondary deformation zone in machining AISI 1045 steel under various process conditions [87].

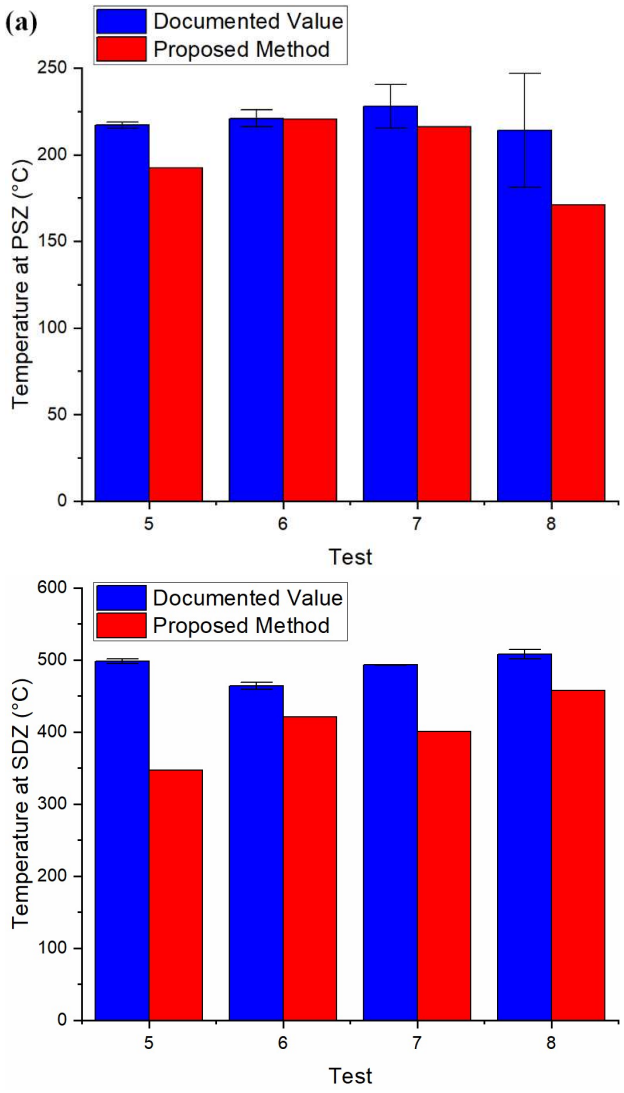

Figure 21 Validation of temperature calculation at (a) primary shear zone and (b) secondary deformation zone in machining AL 6082-T6 alloy under various process conditions [87].

However, the chip thickness is difficult to measure in real-time because of the discontinuous characteristic and restricted accessibility during the cutting process. The machining forces including cutting force and thrust forces were used as model inputs. The shear angle was calculated from the geometrical relationship between forces at the chip formation zone as illustrated in Figure 22.

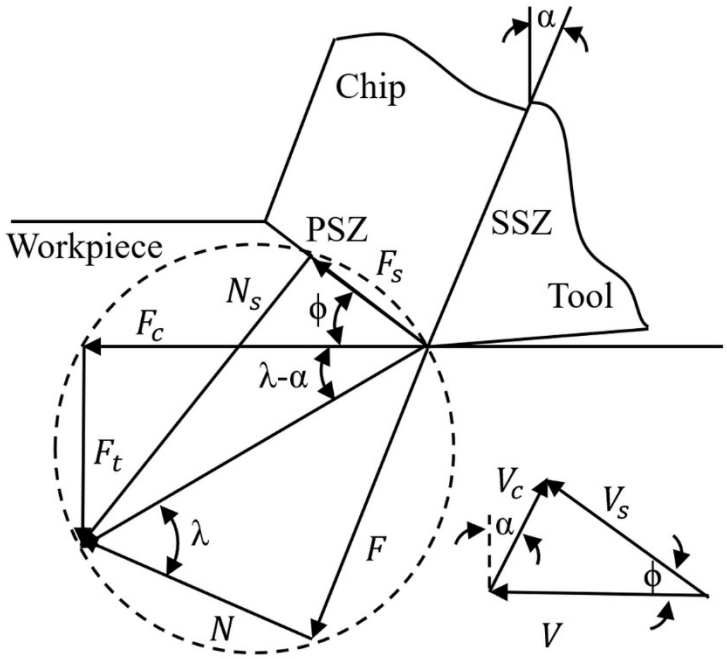

Figure 22 The geometrical relationship between forces in orthogonal cutting configuration [88].

The algorithm of the materials flow stress models is illustrated in Figure 23. The two strain rate constants were calculated from the materials flow stress calculation. The shear angle is calculated as the following,

$$\lambda - \alpha = \text{atan}\left(\frac{F_t}{F_c}\right) \tag{6}$$

$$\phi = \frac{\pi}{4} - \frac{\lambda}{2} + \frac{\alpha}{2} \tag{7}$$

where F_c, F_t are cutting force and thrust force respectively, ϕ, α, λ are the shear angle and tool rake angle, and friction angle respectively

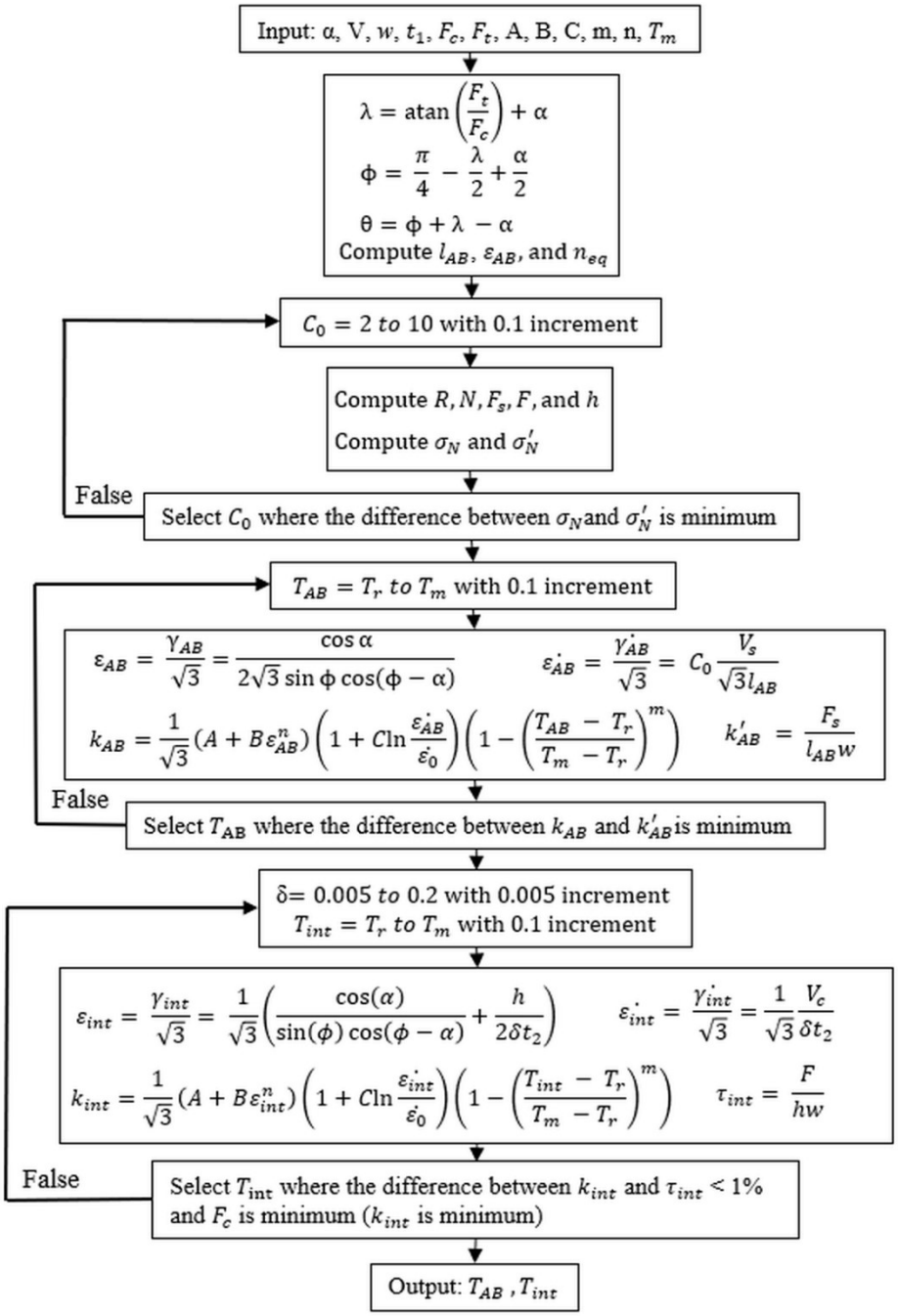

Figure 23 Algorithm of materials flow stress model using experimental cutting force and thrust force.

The presented model was validated with AISI 1045 steel under different cutting conditions. The cutting parameters, experimental machining forces, machining temperatures are given in Table 7. The calculated temperatures were validated by the

documental values. Good agreements were observed as shown in Figure 24. The deviations between the calculated temperatures and documented temperatures might be caused by the experimental accuracy of force measurements and the deviation of other model parameters. The average computational time was 0.27 s, which allows the real-time temperature prediction during the machining process, and cutting parameters planning through inverse analysis.

Table 7 Cutting parameters in orthogonal machining of AISI 1045 steel (w = 2 mm, α = -7 degs, T_0= 25 °C) [19, 26].

Test	V (m/min)	t_1 (mm)	F_{cR}(N)	F_{tR}(N)	T_{ABR} (°C)	T_{intR} (°C)
1	200	0.15	625.42	439.86	407.39	895.07
2	200	0.3	1077.7	637.19	383.1	992.44
3	300	0.15	574.55	364.74	393.31	947.81
4	300	0.3	1003.6	531.84	374.64	1049.8
5	200	0.15	576	500	385	942
6	200	0.3	1007	740	367	1042
7	300	0.15	533	478	374	1017
8	300	0.3	1041	628	387	1025

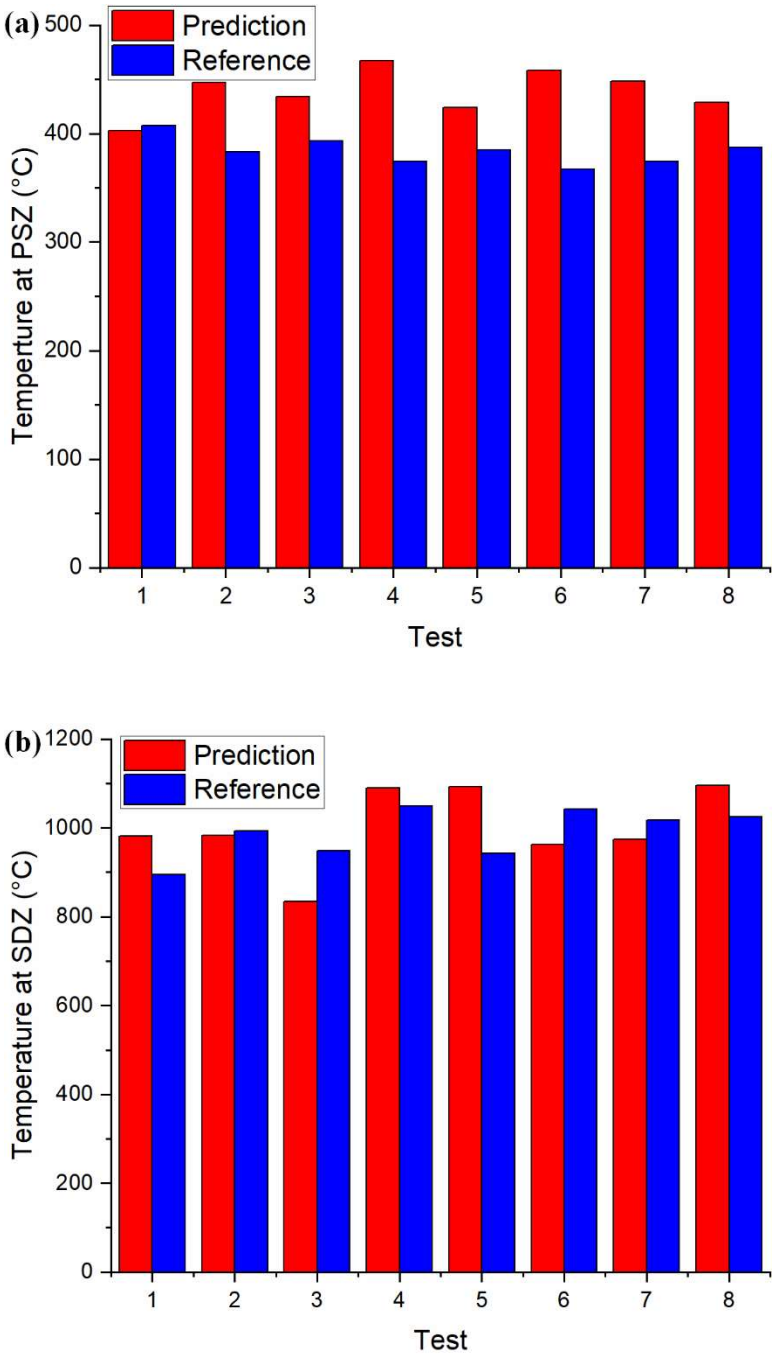

Figure 24 Validation of calculated temperatures at (a) primary shear zone and (b) second deformation zone in machining AISI 1045 steel under various process conditions [88].

A comparison between materials flow stress temperature model, modified chip formation model, and the heat source model were conducted qualitatively as shown in

Table 8, and quantitively as shown in Figure 27, where the black, red, blue, and green colors denote documented values, calculated values using modified chip formation model, calculated values using heat source model, calculated values from materials flow stress model, respectively. The cutting parameters and experimental measurements in the comparative study are given in Table 9**Error! Reference source not found.**.

Table 8 Comparison of three analytical temperature prediction models [91].

Model	Materials Flow Stress Temperature Model [87, 88]	Modified Chip Formation Model	Heat Source Model [21-23]
Input	Cutting parameters; J-C constants; cutting force; chip thickness.	Cutting parameters; J-C constants; workpiece thermal-physical properties; heat partition ratios at PSZ and SDZ respectively.	Cutting parameters; cutting forces; workpiece and tool thermal-physical properties; geometry including lengths and angles of PSZ and SDZ.
Output	The average temperatures at PSZ and SDZ respectively.	The uniform temperatures at PSZ and SDZ respectively.	Temperature distribution at chip formation zone.
Assumption	Constant material flow rate at chip formation zone; steady-state and plane strain condition.	Perfect sharp cutting tool; uniform strain and temperature at two shear zones; steady-state and plane strain condition.	Moving band heat source in the chip; stationary rectangular heat source in the tool; Imaginary heat source for boundary conditions.
Difficulty and limitation	Prediction of average temperature at PSZ and SDZ respectively.	Determination of heat partition ratios at PSZ and SDZ respectively; Prediction of uniform temperatures at PSZ and SDZ respectively.	Determination of geometry including lengths and angles of PSZ and SDZ.

Table 9 Orthogonal cutting parameters, experimental machining force, machining temperature, chip thickness of AISI 1045 steel [19, 79].

Test	V (m/min)	t_1 (mm)	t_2 (mm)	F_c (N)	F_t (N)	T_{AB} (°C)	T_{int} (°C)
1	200	0.15	0.31	529-602	320-400	301	861
2	200	0.30	0.54	881-1006	348-596	294	984
3	300	0.15	0.28	503-564	245-343	297	932
4	300	0.30	0.69	800-1122	296-696	332	869

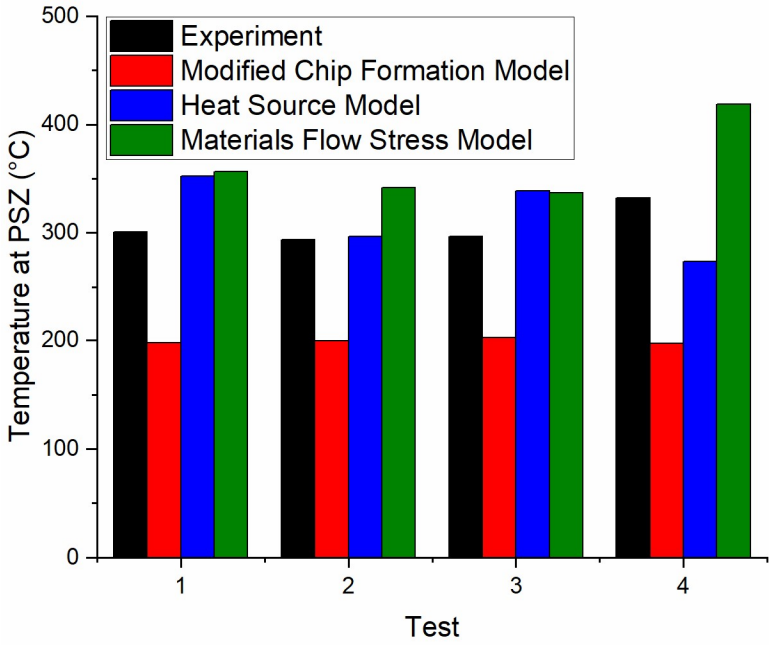

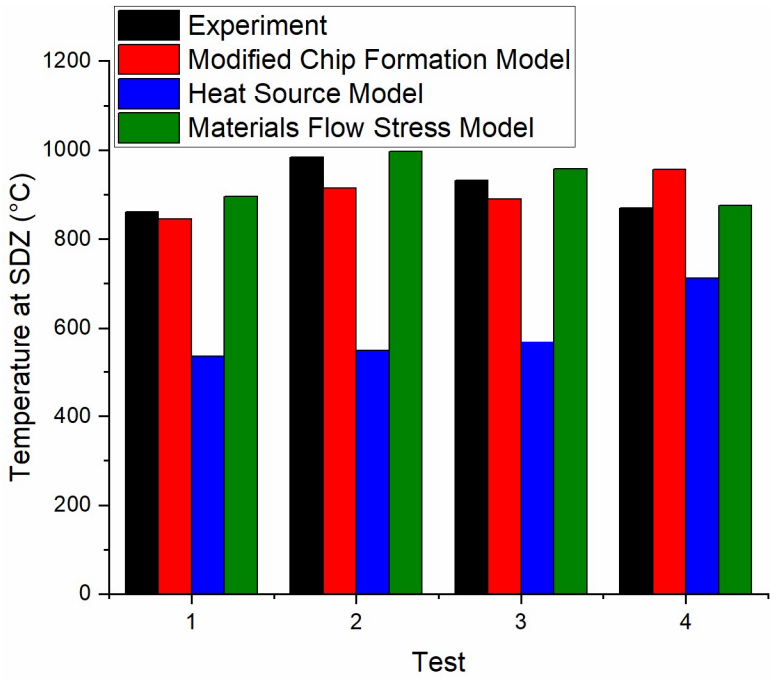

Figure 25 Comparison between calculated temperatures in multiple cutting tests. (a) average temperatures at primary shear zone; (b) average temperatures at the secondary deformation zone [92].

3.3 Case Study in Machining Ultra-Fine-Grained Pure Titanium

In this section, the studies in machining UFG Ti using the developed analytical models were discussed. The scientific pillar of analytical modeling in the machining process is illustrated in Figure 26. In this study, the J-C model constants were inversely identified in the modeling of the orthogonal cutting process. The machining forces and machining temperatures were calculated using the chip formation model, and the materials flow stress model. Multiple machining tests were performed under various process conditions for the purposes of model calibration and validation.

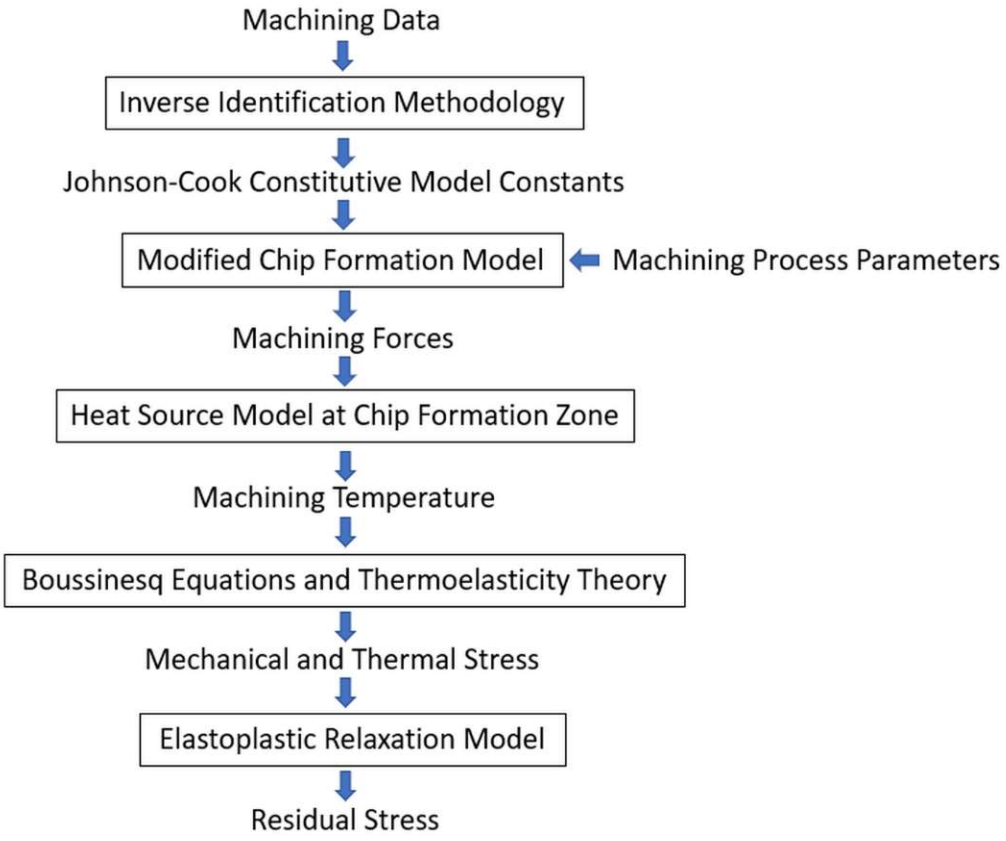

Figure 26 Scientific pillar in analytical modeling of precision machining.

As shown in Figure 27, multiple cutting tests were performed with Okuma Genos L250 CNC lathe under different cutting conditions. A triangular cutting insert with a 0-degree rake angle and a tool holder with a 0-degree lead angle from Kennametal were used to enforce the orthogonal cutting. A piezoelectric dynamometer and data acquisition system (DAQ) from National Instrument were employed to measure the experimental forces in orthogonal cutting. The cutting parameters are given in Table 10.

The specimen was prepared with commercially pure grade 4 titanium (CP4) using a severe plastic deformation (SPD) process, specially named equal channel angular extrusion (ECAE), in which the raw material underwent four passes through a 90-degree

angle die at temperature 345 °C, 300 °C, 275 °C, and 260 °C, respectively. No rotation was introduced in-between passes. No rolling was performed in-between passes. The extrusion speed and strain intensity were 0.254 mm/s and 1.15 for each pass. The bulk UFG Ti bar was then machined into a cylindrical shape with a tubular feature at one end. The specimen was processed with heat treatment in a GSL-1700X vacuum tube furnace at 480 °C for 20 minutes for residual stress relief purposes.

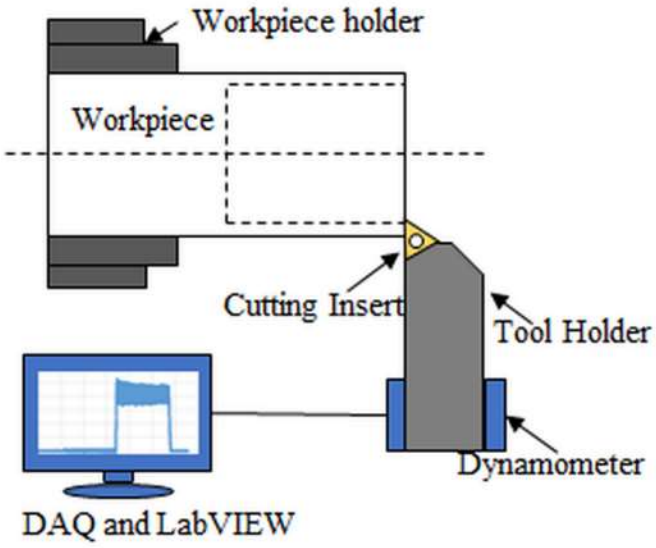

Figure 27 Experimental setup in machining ultra-fine-grained pure titanium.

Table 10 Cutting parameters and experimental forces in machining UFG Ti [93].

Test	V (m/min)	w (mm)	t_1 (mm)	α (deg)	F_c^{Exp} (N)	F_t^{Exp} (N)
1	60	1	0.2	0	333.83	206.32
2	75	1	0.2	0	338.14	204.81
3	90	1	0.3	0	480.38	231.44
4	60	0.5	0.3	0	302.13	117.52
5	90	0.5	0.4	0	351.50	118.66
6	120	0.5	0.4	0	350.35	124.24

The J-C model constants were identified with machining data under test 1, test 2 and test 3 conditions. The convergence patterns of identified J-C constants are shown in Figure 28, where the heat partition ratio ψ is determined as an output variable. The assumptions of plane strain, steady-state, and perfectly sharp cutting tool are enforced in the employed modified chip formation model with temperature at PSZ calculated by the energy balance equation. The identified J-C model constants are given in Table 11.

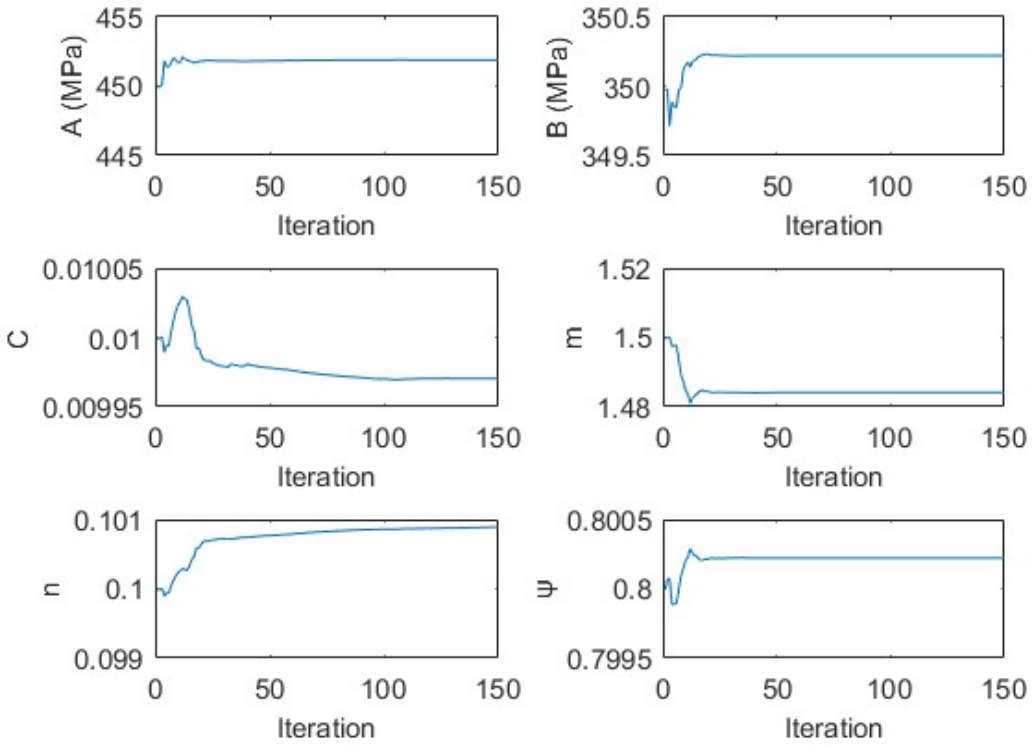

Figure 28. Convergence patterns of the identified J-C constants in 150 iterations with test 1 [93].

Table 11. Predicted J-C constants of UFG Ti and corresponding calibration errors [93].

Test	A (MPa)	B (MPa)	C	m	n	ψ	Fc calibration error (%)	Ft calibration error (%)
Initial	450	350	0.010	1.500	0.100	0.80	NA	NA
1	426.78	349.55	0.012	1.514	0.075	0.80	3.50	4.25
2	412.43	343.54	0.011	1.623	0.100	0.82	1.28	8.71
3	451.89	350.22	0.010	1.484	0.101	0.80	0.50	0.32

The J-C model constants identified from machining data (test 3) were validation with experimental forces under different process conditions. Good agreements were observed upon validation. The deviations might be caused by the model assumption of a perfectly sharp cutting tool, which neglected tool geometry and build-up edge during the machining process.

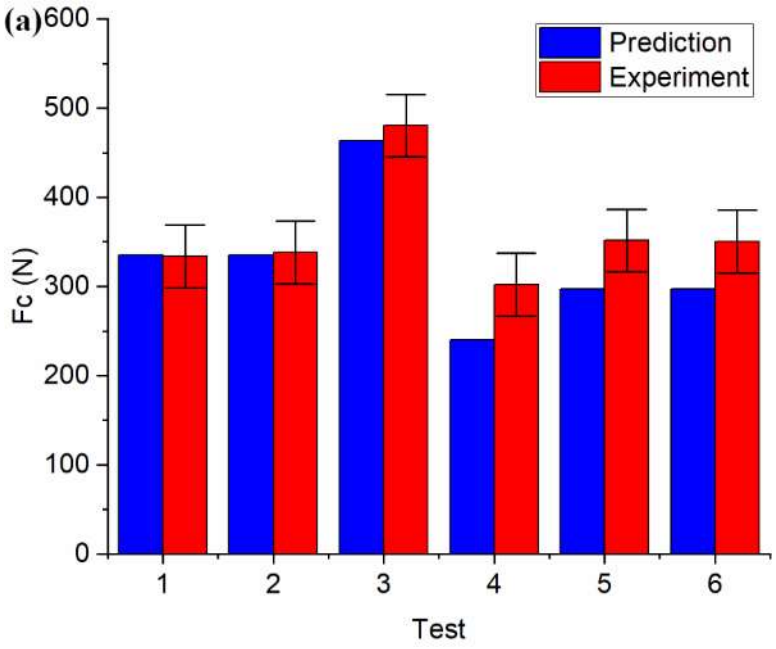

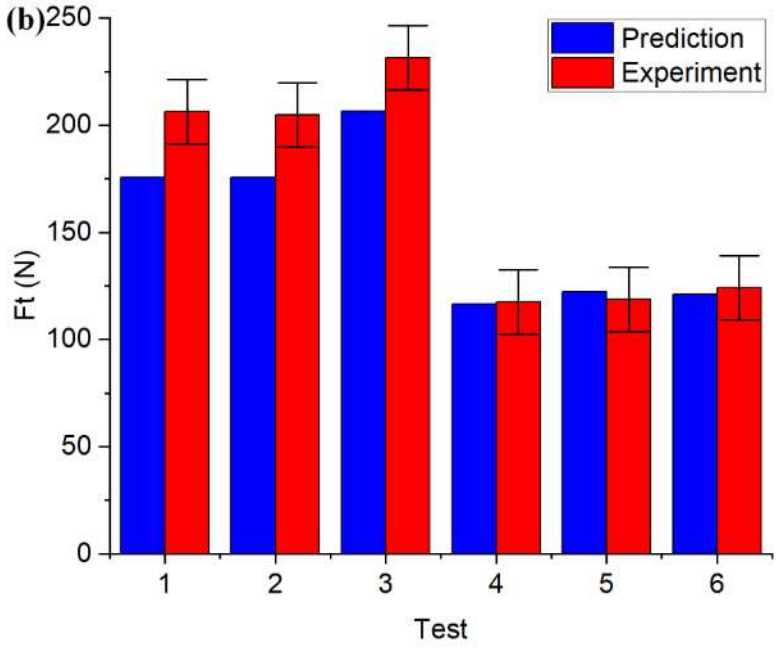

Figure 29 Validation of the identified Johnson-Cook model constants of UFG Ti with (a) cutting forces and (b) thrust forces [94].

To investigate the influence of input J-C constants on the prediction accuracy, each J-C model constant was deliberately varied with the same amount up to ± 30%. Machining forces were predicted with test 1 cutting condition. The corresponding deviations of predicted forces and prediction error are illustrated in Figure 30. To investigate the influence of input cutting conditions, each cutting parameter was deliberately varied with the same amount up to ± 30%. The corresponding deviations and prediction errors are illustrated in Figure 31. The input variations had a significant influence on the predicted forces. Minimum prediction errors were observed with adopted J-C model constants and input cutting parameters. An increasing deviation of inputs resulted in an increasing prediction error.

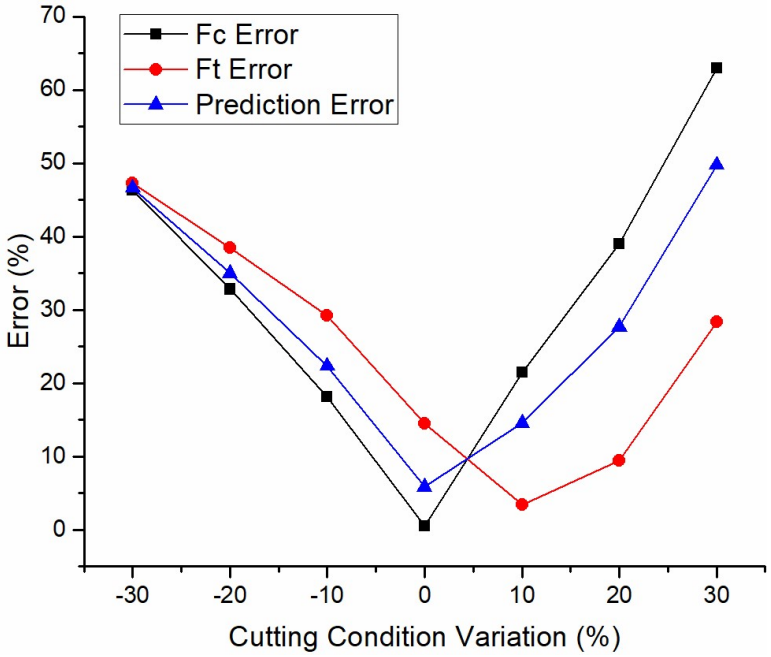

Figure 30 Sensitivity analyses of input J-C model constants with input variation up to ± 30% under test 1 cutting condition [94].

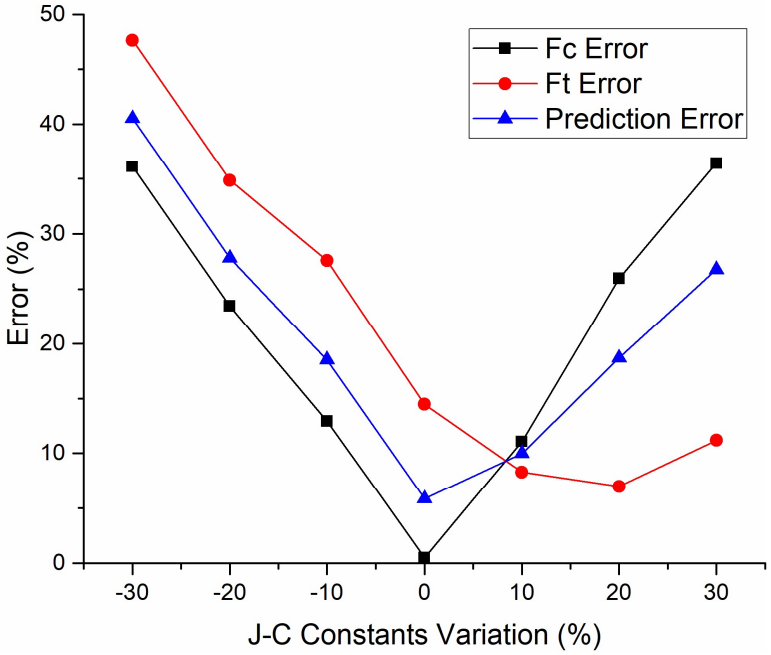

Figure 31 Sensitivity analyses of input cutting conditions with input variation up to ± 30% under test 1 cutting condition [94].

The machining forces of UFG Ti were compared to that of Ti6Al4V alloy. The machining forces were calculated using the modified chip formation model under the same process conditions, specifically tests 1to 4 conditions as in Table 10. The machining forces of UFG Ti were smaller than that of Ti6Al4V alloy as shown in Figure 32. It is well-known that the machining forces are positively correlated to machining temperatures, large machining forces and elevated temperatures are detrimental for tool performance and life, and quality by softening tool material and increasing diffusion. Therefore, the UFG Ti has preferable machinability compared to the Ti6Al4V alloy.

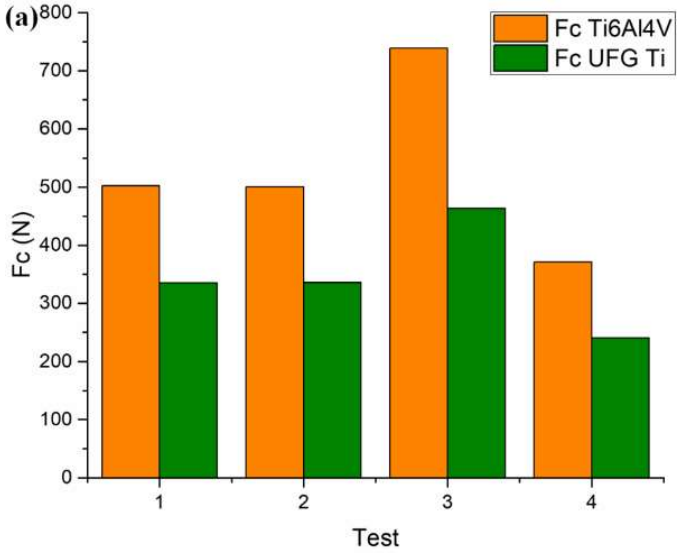

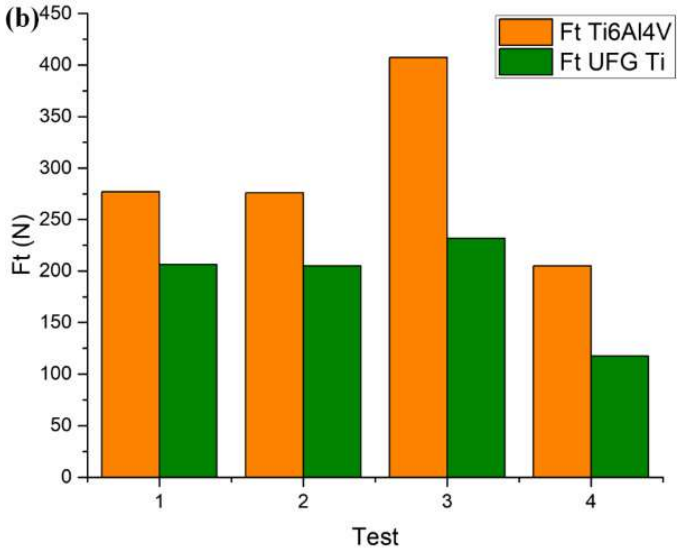

Figure 32 Force comparison in machining Ti6Al4V alloy and UFG Ti under various cutting conditions. (a) comparison of cutting forces. (b) comparison of thrust forces [94].

The machining temperatures at PSZ and SDZ were obtained from the modified chip formation model as intermediate variables, which were marked as Ref denoting reference values. The machining temperatures were also calculated from the material flow stress model, which was marked with Pre denoting predicted values. The minimization of the difference between calculated stress using mechanical model and the calculated stress using J-C model yields the estimations of the machining temperatures at PSZ and SDZ. Close agreements were observed between predictions using modified chip formation model and materials flow stress model, as shown in Figure 33, where Pre denotes predicted temperature value, Ref denotes reference temperature value.

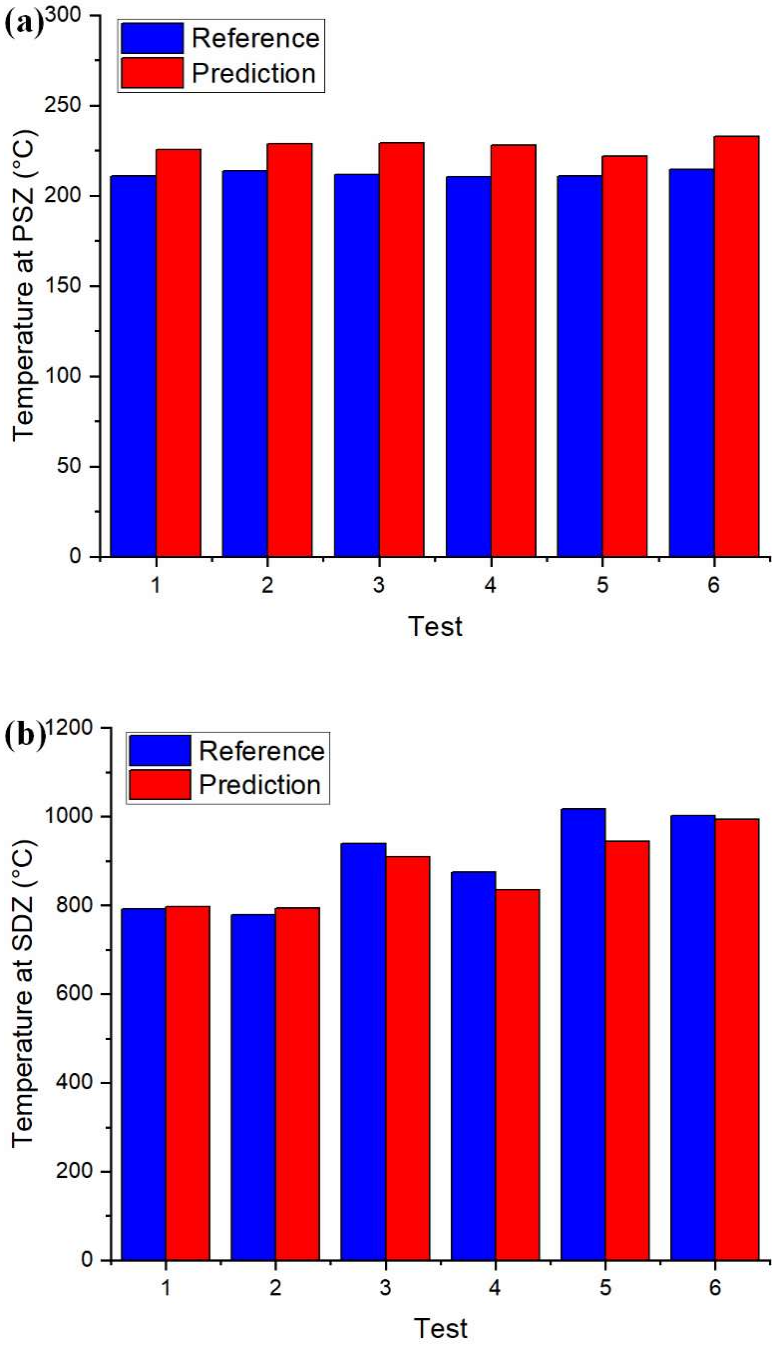

Figure 33 Validation of calculated temperatures (Pre) against reference values (Ref) at (a) primary shear zone and (b) secondary deformation zone under various cutting conditions [95].

CHAPTER 4. ANALYTICAL MODELING OF METAL ADDITIVE MANUFACTURING

4.1 Overview of Analytical Modeling in Metal Additive Manufacturing

Analytical modeling methodology has demonstrated its sufficient prediction accuracy with a significant computational advantage in the study of precision machining. In this section, analytical modeling methodology was employed in the prediction of temperature profile, part porosity, thermal stress, in-situ deformation, residual stress, and part distortion in metal additive manufacturing. The scientific pillar in the modeling of metal additive manufacturing is shown in Figure 34. The powder size statistical distribution was used in the calculations of powder material properties and powder bed porosity. An advanced temperature model was developed based on the moving heat source solution for laser heat input, and heat sink solution for boundary heat loss. The part porosity due to lack-of-fusion was calculated from the thermal analysis on the part cross-sectional area. The thermal stress was calculated from the temperature calculation by the thermoelasticity theory. The thermal deformation was calculated from the thermal stress calculation during the process. The residual stress and residual stress-induced part distortion were calculated from the thermal stress calculation using an elastoplastic relaxation procedure and surface displacement calculation.

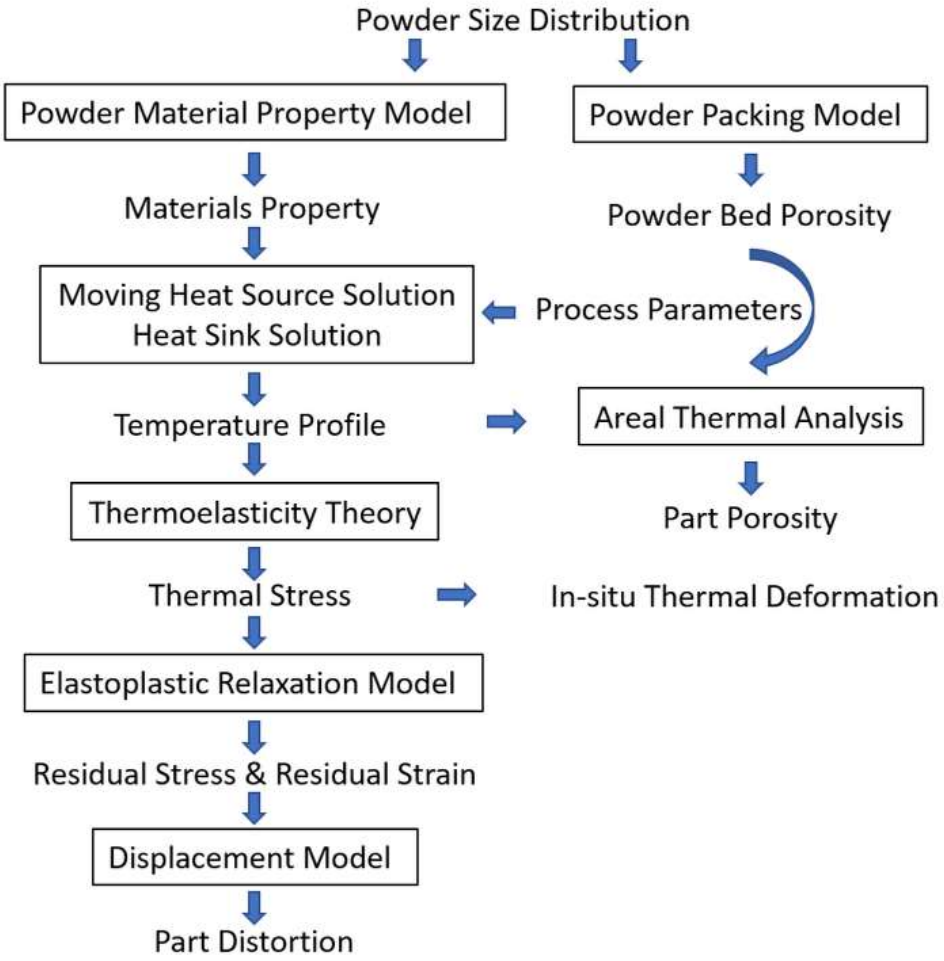

Figure 34 Scientific pillar in analytical modeling of metal additive manufacturing.

4.2 Analytical Thermal Modeling in Metal Additive Manufacturing

In this section, the analytical thermal modeling of metal additive manufacturing was discussed in PBMAM and PFAMAM. The analytical thermal models have been developed with considerations of follows.

(1) Scan strategy in metal additive manufacturing

(2) Heat transfer boundary condition in metal additive manufacturing

(3) Statistical powder size distribution and powder packing related material properties.

4.2.1 Thermal Modeling in Metal Additive Manufacturing Considering Scan Strategy

The existing analytical models employed a moving coordinate and semi-infinite medium assumption, which neglected the part dimensions and thus reduced their usefulness in real applications. In this section, an analytical model was presented to calculate the in-process temperature in PBMEM using a stationary coordinate with an origin at the part boundary (absolute coordinate). Analytical solutions were developed for temperature prediction of single-track scan and multi-track scans considering scanning strategy as illustrated in Figure 35. Inconel 625 was chosen to test the presented model. The material properties and process parameters are given in Table 12 and Table 13 respectively.

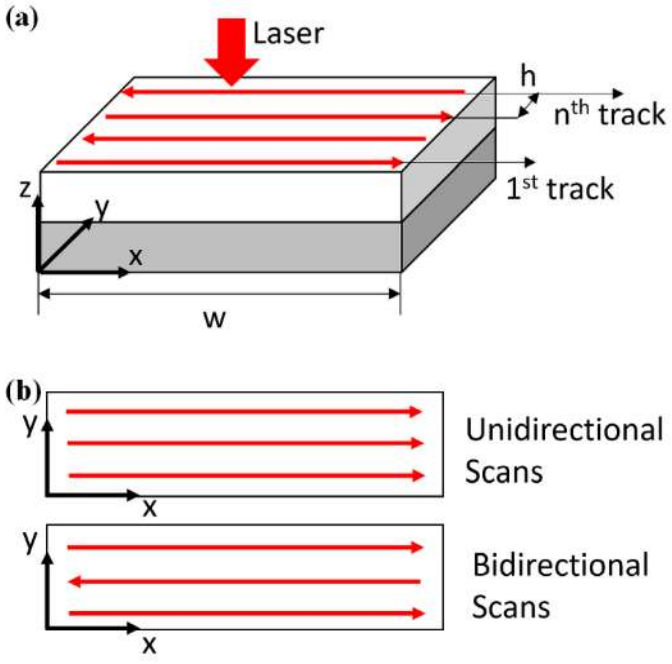

Figure 35 Schematic view of scan strategy in metal additive manufacturing. w and h denote track length and hatch space respectively, (b) schematic view of unidirectional scans and bidirectional scans.

Table 12 Material properties of Inconel 625 [96].

Name	Symbol	Value	Unit
Density	ρ	8840	kg/m^3
Thermal conductivity	k	9.8	W/(m· °C)
Specific heat	c	410	J/(kg·°C)
Solidus temperature	T_S	1290	°C
Liquidus temperature	T_L	1350	°C
Latent heat	H_f	227000	J/kg
Absorption	η	0.4	1

Table 13 Process conditions for single-track scans and bidirectional scans in powder bed metal additive manufacturing of Inconel 625.

Test	Laser Powder P (W)	Scanning Velocity V (mm/s)	Hatch Space H (mm)	Layer Thickness t_L (μm)
1	169	875	0.1	20
2	195	875	0.1	20
3	182	800	0.1	20
4	195	725	0.1	20
5	169	725	0.1	20
6	195	800	0.1	20

The moving heat source solution was derived from the heat balance equation expressed as the following.

$$\frac{\partial \rho u}{\partial t} + \frac{\partial \rho h V}{\partial x} = \nabla \cdot (k \nabla T) + \dot{q} \tag{8}$$

where u is internal energy, h is enthalpy, ρ is density, k is conductivity, and $\dot{q}$ is a volumetric heat source, t is time, x is distance, V is heat source moving speed, and T is temperature.

The temperature distribution is calculated from the superposition of the point moving heat source solution and heat sink solution as the following.

$$\theta(\boldsymbol{x}, \boldsymbol{0}, \boldsymbol{z}, \boldsymbol{t}) = \theta_1 + \theta_2 \tag{9}$$

$$\theta_1(\boldsymbol{x}, \boldsymbol{h}, \boldsymbol{z}, \boldsymbol{t_1}) = \frac{P\eta}{8\rho C_p(\pi\kappa)^{\frac{3}{2}}} \int_0^t \frac{exp\left[-\frac{\left(x - V(t-t')\right)^2 + y^2 + z^2}{4\kappa(t-t')}\right]}{(t-t')^{\frac{3}{2}}} dt' \tag{10}$$

$$\theta_1(\boldsymbol{x}, \boldsymbol{h}, \boldsymbol{z}, \boldsymbol{t_1}) = \frac{P\eta}{2Rk\pi^{\frac{3}{2}}} \exp\left(\frac{Vx}{2\kappa}\right) \int_{\frac{R}{2\sqrt{\kappa t}}}^{\infty} \exp\left[-\xi^2 - \left(\frac{V^2R^2}{16\kappa^2\xi^2}\right)\right] d\xi \tag{11}$$

$$\theta_2(\boldsymbol{x}, \boldsymbol{0}, \boldsymbol{z}, \boldsymbol{t}) = \frac{P}{8\rho c(\pi\kappa)^{\frac{3}{2}}} \int_{t1}^t \frac{exp\left[-\frac{\left(x - V(t-t')\right)^2 + y^2 + z^2}{4\kappa(t-t')}\right]}{(t-t')^{\frac{3}{2}}} dt' \tag{12}$$

$$\theta_2(\boldsymbol{x}, \boldsymbol{0}, \boldsymbol{z}, \boldsymbol{t}) = \frac{P}{8\rho c(\pi\kappa)^{\frac{3}{2}}} \int_{t1}^t \frac{exp\left[-\frac{\left(x + V(t-t')\right)^2 + y^2 + z^2}{4\kappa(t-t')}\right]}{(t-t')^{\frac{3}{2}}} dt' \tag{13}$$

where θ is temperature change ($\theta = T - T_0$), R is the distance from the laser heat source ($R^2 = x^2 + y^2 + z^2$), κ is thermal diffusivity ($\kappa = k/\rho c$).

In addition, latent heat is considered using the heat integration method, which the temperature of the molten pool material is lowered by an amount as the following due to the phase transformation [54]. The temperature change due to the consideration of latent heat is calculated as the following.

$$\Delta T = H_f / c \tag{14}$$

where ΔT is temperature change, H_f is latent heat, c is specific heat.

The molten pool dimensions including molten pool length, molten pool width, molten pool depth, were calculated with varying laser absorption from the temperature calculation as illustrated in Figure 36. It should be noted that the color bar values are corresponding to the temperature contours rather than the maximum temperature at the heat-affected zone. The laser absorption was inversely determined with the minimum error of the calculation of molten pool dimensions as 40 % as shown in Figure 37.

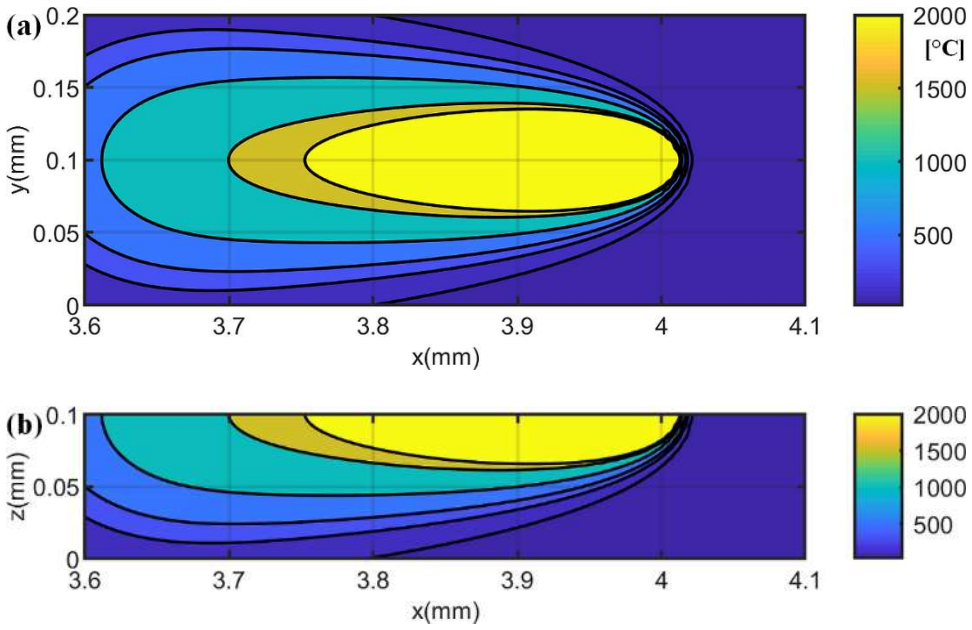

Figure 36 Calculated temperature distribution at t = 5 ms (laser location x = 4 mm, y = 0.1 mm) in single-track scan under test 6 condition with 40% absorption. (a) top view; (b) cross-sectional view at laser scanning location. [96].

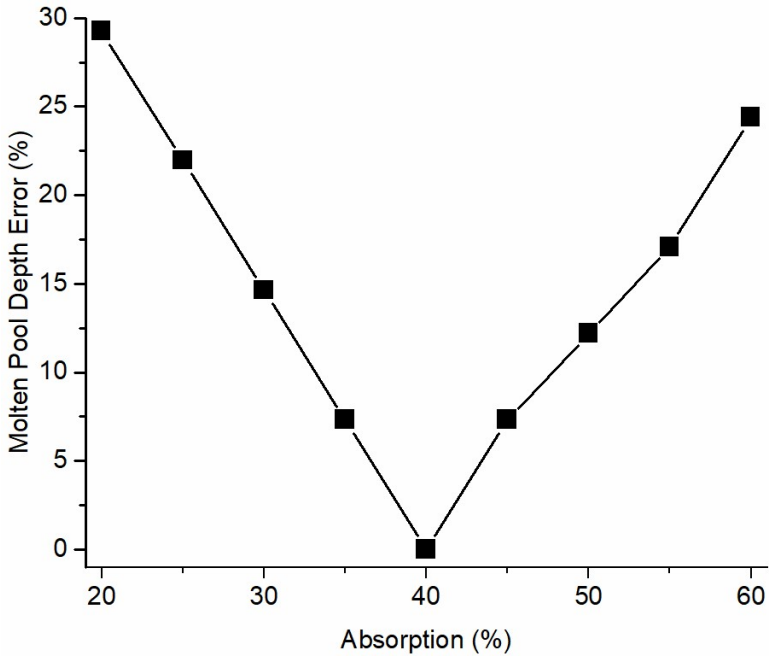

Figure 37 Inverse determination of laser absorption based on molten pool depth calculation under test 6 condition [96].

The molten pool evolution was investigated with respect to scanning time as shown in Figure 38 and Figure 39. The stabilized temperatures in the single-track scan and bidirectional scans were predicted under various process conditions. Good agreements were observed upon validation to experimental values as shown in Figure 40, in which the experimental molten pool dimensions were measured based on solidification microstructure. In addition, the influence of powder bed porosity on the temperature prediction was investigated through sensitivity analysis as shown in Figure 41, where the positive relationships were observed between powder bed porosity and molten pool dimensions. The larger the powder bed porosity, the larger the molten pool size because the powder bed porosity decreases thermal conductivity, which prevented the thermal energy dissipation and facilitated the formation of the molten pool.

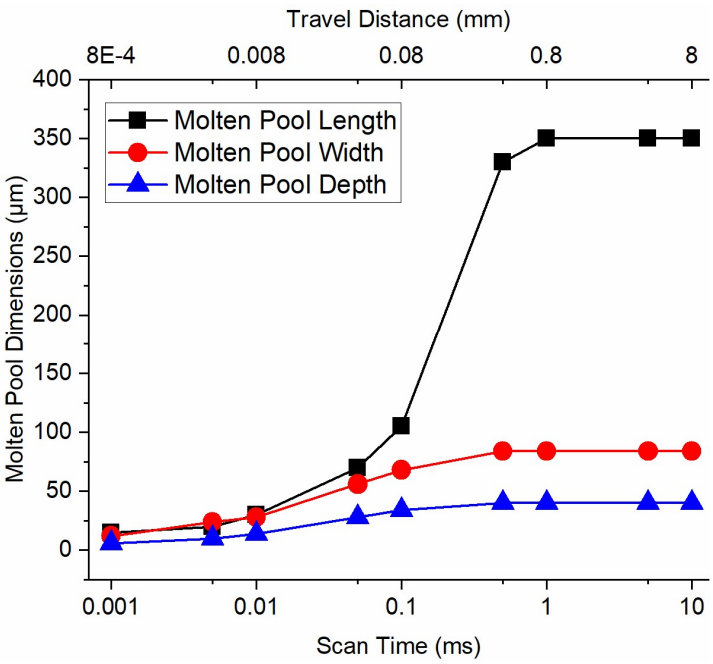

Figure 38 The growth and stabilization of calculated molten pool in a single-track scan in terms of molten pool length, molten pool width, and molten pool depth [96].

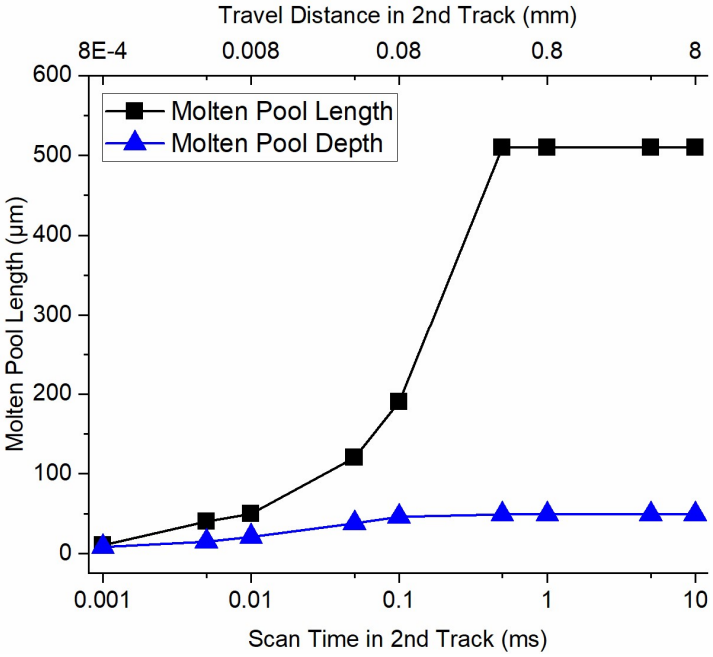

Figure 39 The growth and stabilization of the calculated molten pool in the second track of bidirectional scans in terms of molten pool length and molten pool depth [96].

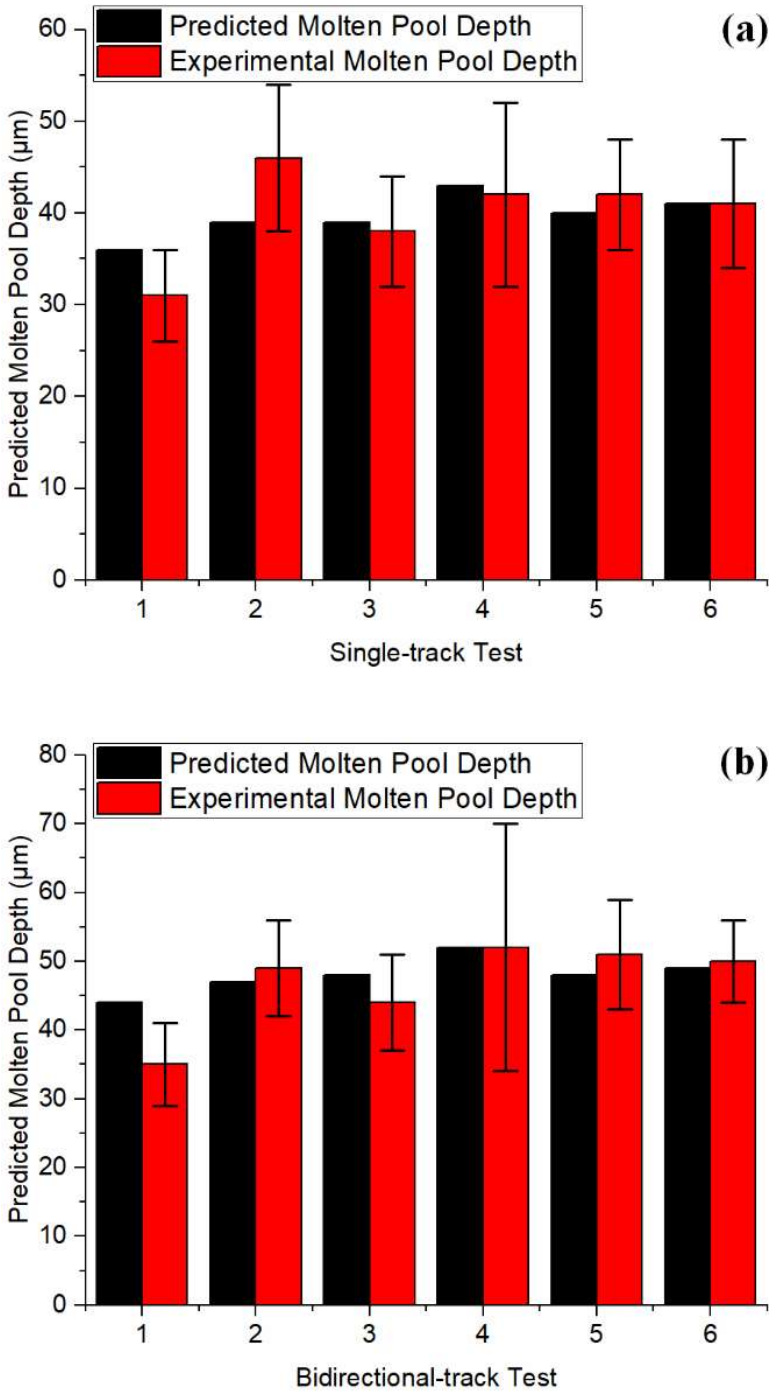

Figure 40 Validation on stabilized molten pool depth in (a) single-track scan (b) bidirectional scan. [96].

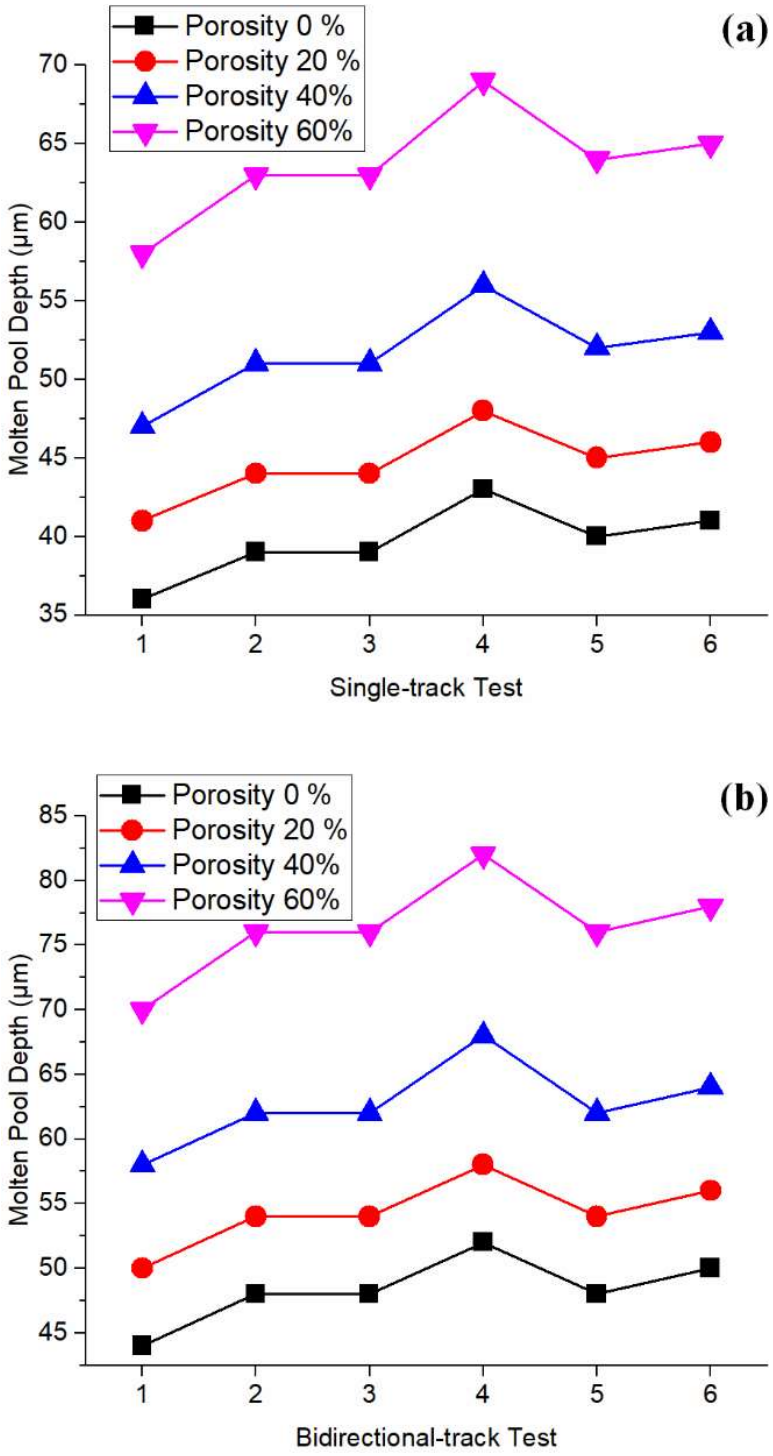

Figure 41 Influence of powder bed porosity on molten pool through sensitivity analyses in (a) single track scans and (b) bidirectional scans. [96].

4.2.2 Thermal Modeling in Metal Additive Manufacturing Considering Boundary Heat Transfer

This section presented an explicit solution, namely heat sink solution, to consider the heat transfer boundary condition. The heat sink solution was developed from the point moving heat source solution based on heat transfer of conduction, convection, and radiation. The heat transfer mechanism in PBMAM is illustrated in Figure 42, in which the red arrow, green arrows, blue arrows, and orange arrows denote the laser heat input, heat loss from top boundary due to convection and radiation, heat loss to surrounding powders due to conduction, heat loss to the platform due to conduction, respectively. The heat transfer mechanism in PFMAM is illustrated in Figure 43.

The heat transfer equations for conduction, convection, and radiation are expressed as the following.

$$Q_{cond} = Ak_p\Delta T/R \tag{15}$$

$$Q_{conv} = Ah(T - T_0) \tag{16}$$

$$Q_{rad} = A\varepsilon\sigma(T^4 - T_0^4) \tag{17}$$

where $Q_{cond}, Q_{conv}, Q_{rad}$ are boundary heat loss from conduction, convection, and radiation respectively, A, T are the area and temperature of the heat sink, R is the distance from heat sink, ΔT is the temperature difference between heat sink location and surrounding powders, k_p is powder thermal conductivity, h is heat convection coefficient, ε is emissivity, σ is Stefan-Boltzmann constant.

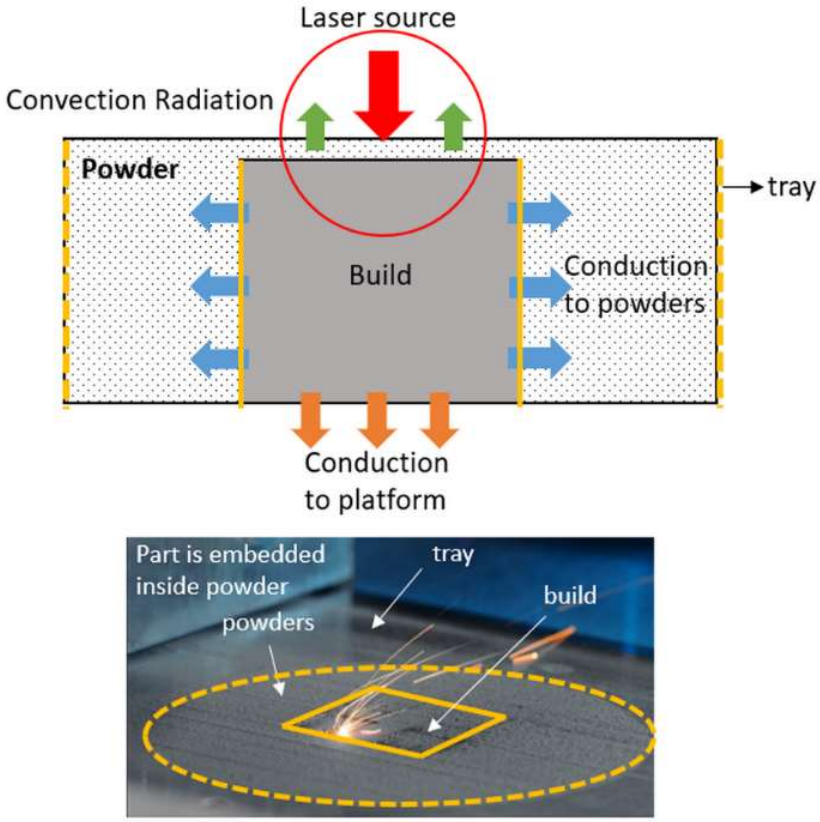

Figure 42 Schematic view of the heat transfer mechanism in powder bed metal additive manufacturing.

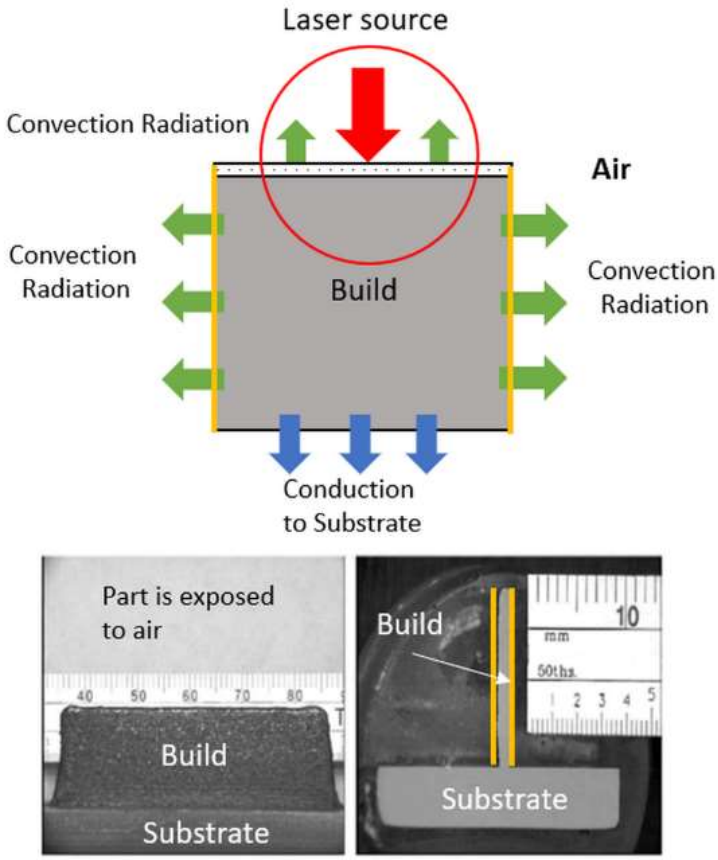

Figure 43 Schematic view of the heat transfer mechanism in powder feed metal additive manufacturing.

The part boundary is mathematically discretized into many heats sinks due to the non-uniform temperature distribution, which causes non-uniform heat loss as shown in Figure 44, where the red arrow and green arrows represent represents heat input from the laser source and the heat loss from part boundary due to convection and radiation, respectively. x, y, z denote coordinate directions. L, W, D denote the molten pool length, width, and depth respectively. With the heat sink solution, the complete understanding of the heat transfer mechanism in PBMAM can be implemented conveniently and computational efficiency. Therefore, the usefulness of the developed analytical model can be significantly improved in real applications.

The point moving heat source solution at steady state is expressed as the following.

$$\theta_L(x,y,z) = \frac{P\eta}{4\pi kR(T_m - T_0)} exp\left(\frac{-V(R+x)}{2\kappa}\right) \tag{18}$$

The heat sink solutions in PBMAM and PFMAM are expressed as the following.

$$\theta_S(x,y,z) = \sum_{i=0}^{n} \frac{A_i}{4\pi kR(T_m - T_0)} \left[h(T_i - T_0) + \varepsilon\sigma(T_i^4 - T_0^4) + \frac{k(T_i - T_0)}{R} \right] \tag{19}$$

The temperatures are finally calculated from the superposition of the point moving heat source solution and heat sink solution as the following.

$$\theta(x,y,z) = \frac{P\eta}{4\pi kR(T_m - T_0)} exp\left(\frac{-V(R+x)}{2\kappa}\right) - \sum_{i=0}^{n} \frac{A_i}{4\pi kR(T_m - T_0)} \left[h(T_i - T_0) + \varepsilon\sigma(T_i^4 - T_0^4) + \frac{k(T_i - T_0)}{R} \right] \tag{20}$$

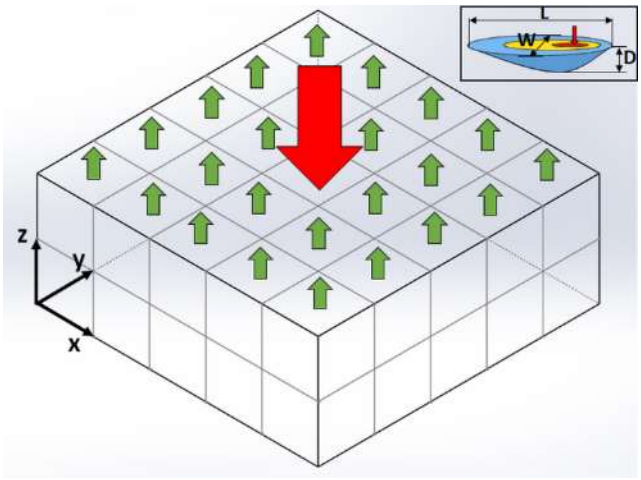

Figure 44 Schematic drawing of the heat transfer mechanism in PFMAM [79].

Table 14 Materials properties of Ti6Al4V alloy in PBMAM [97].

Name	Symbol	Value	Unit
Density	ρ	4428	kg/m^3
Thermal conductivity (powder at T_0)	k_p	6.6	W/(m·K)
Thermal conductivity (solid)	k_s	$-0.797 + 18.2 \times 10^{-3}T - 2 \times 10^{-6}T^2$ $(T < 1923K)$ 33.4 (T>1923K)	W/(m·K)
Specific heat (powder at T_0)	c_p	580	J/(kg·K)
Specific heat (solid)	c_s	$411.5 + 2 \times 10^{-1}T - 5 \times 10^{-7}T^2$ $(T < 1923K)$ 830 (T>1923K)	J/(kg·K)
Absorption	η	0.77	1
Latent heat	H_f	365000	J/kg
Room temperature	T_0	20	°C
Solidus temperature	T_s	1605	°C
Liquidus temperature	T_l	1655	°C
Heat convection coefficient	h	24	W/(m^2·K)
Emissivity	ε	0.9	1
Stefan-Boltzmann constant	σ	5.67×10^{-8}	W/(m^2·K^4)

The heat sink solution was derived and employed for imposing heat transfer boundary conditions without significant compensation of computational efficiency in analytical temperature modeling. The implementation of the heat sink solution was investigated by applying different numbers of heat sinks in the temperature prediction of

PBMAM of Ti6Al4V. The material properties of Ti6Al4V alloy are given in Table 14, where the material properties of powders were used in the calculation of temperature distribution, and the material properties of solid were used in the calculation of temperature affected materials properties. The process parameters are given in Table 15. The temperature profile, thermal gradient, and the temperature-affected material property variation were calculated in the single-track scan.

Table 15 Process parameters in PBMAM of Ti6Al4V.

Test	Laser Power (W)	Scan velocity (mm/s)
1	100	500
2	100	750
3	100	1000
4	100	1200
5	150	500
6	150	750
7	150	1000
8	150	1200

As shown in Figure 45, the number of heat sinks on the top boundary was chosen as 4x4, 6x6, 8x8, and 10x10 under test 1 process condition respectively. The dash lines represent the calculated temperature profiles without consideration of heat loss (No heat sink). The solid lines represent the calculated temperature profiles with consideration of heat loss. Red circles represent the centers of heat sinks. The area of heat sink under each setting is identical to the total area/number of heat sinks. For example, the area of each heat sink with 4x4 setting is identical as total area/16. The area of each heat sink with chosen 8x8 setting is identical as total area/64. The heat loss from the side boundary was not

considered because of the significantly lower temperature than the top boundary near heat source location (x = 0.8 mm, y =0.5 mm). The red circles represent the centers of heat sinks. The temperature profiles were predicted using the presented model with consideration of heat loss at the top boundary (plotted as solid lines). For comparison, the temperature profiles were also calculated using the point heat source solution without consideration of heat loss at the top boundary (plotted dashed lines). As shown in the temperature profiles on the top boundary at the x-y plane, the predicted heat-affected zones considering the heat loss (solid lines) were smaller than those predicted without considering the heat loss (dashed lines) at each temperature level. The more heat sinks, the smaller the heat-affected zone, and vice versa. The employed heat sink solution can reduce the overestimation of temperature levels and thus improve the prediction accuracy.

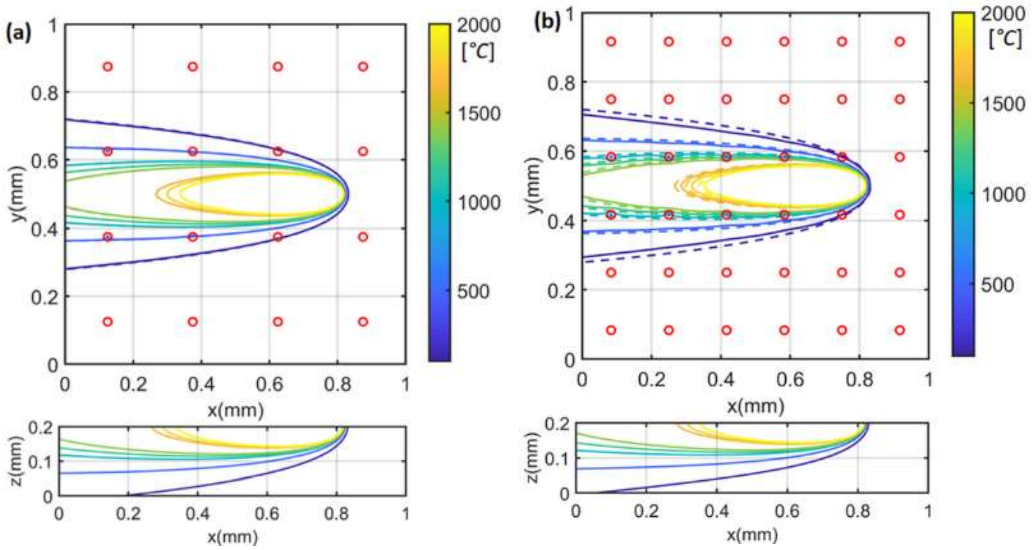

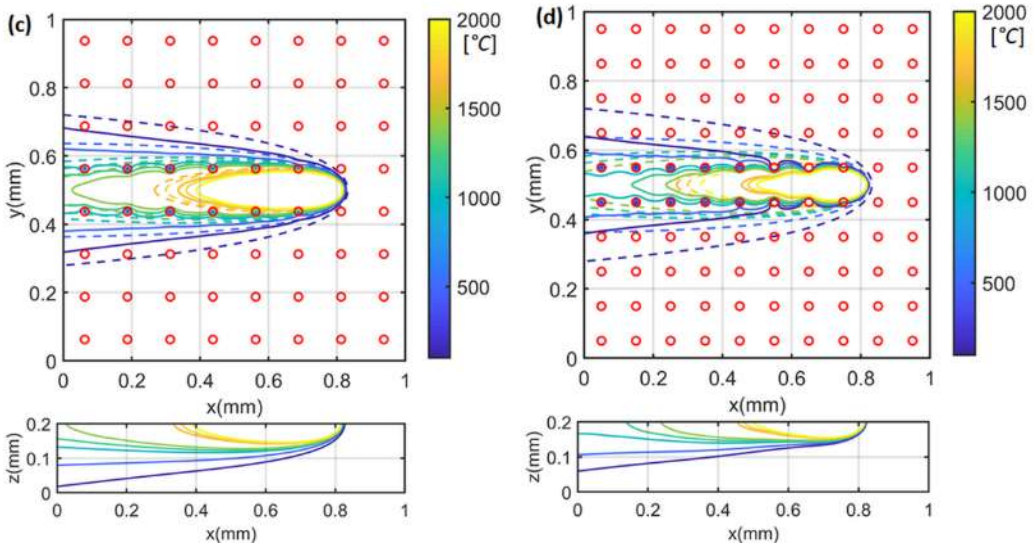

Figure 45 Calculated three-dimensional temperature distribution with (a) 4x4=16 heat sinks (b) 5x5=25 heat sinks (c) 8x8=64 heat sinks (d) 10x10=100 heat sinks. The heat source is located x = 0.8 mm y = 0.5 mm [97].

The temperature gradient profiles were plotted in Figure 46 with a different number of heat sinks. The large temperature gradient was observed at the near heat source location (x = 0.8 mm y = 0.5 mm) and near heat sink location (marked as red circles). The materials property variations, namely the thermal conductivity and the specific heat, were plotted in Figure 47 and Figure 48 respectively. The material property variation was caused by the temperature-dependent nature and the temperature variation.

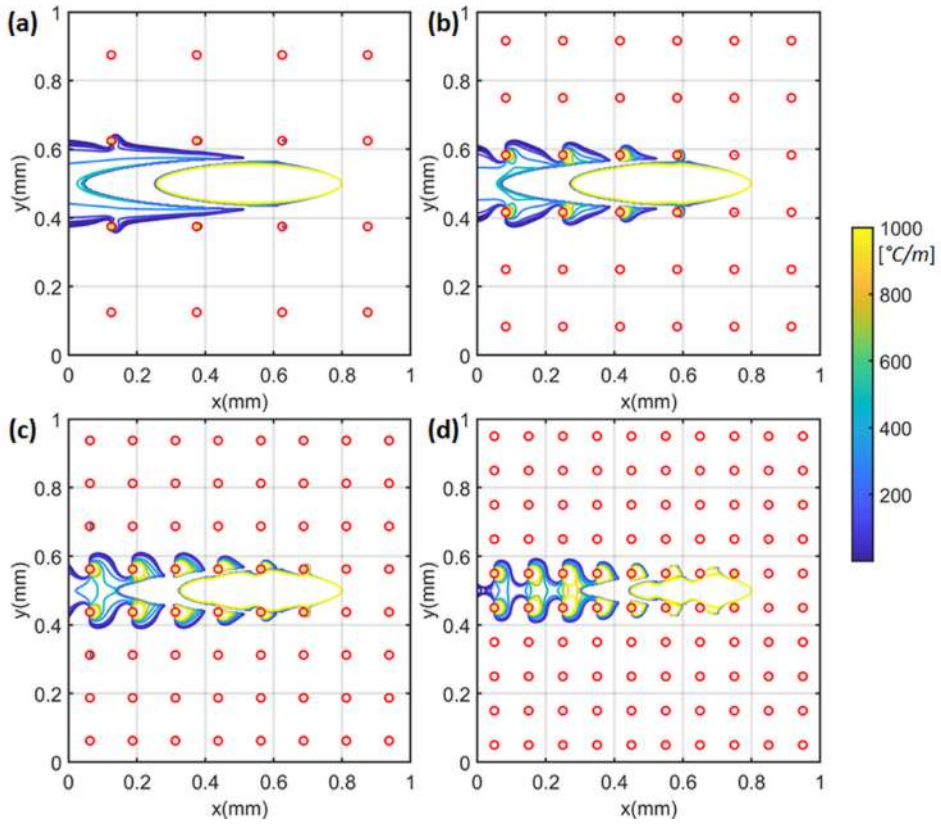

Figure 46 Calculated temperature gradient with (a) 4x4=16 heat sinks (b) 5x5=25 heat sinks (c) 8x8=64 heat sinks (d)10x10=100 heat sinks. The moving laser is located at x = 0.8 mm y = 0.5 mm [97].

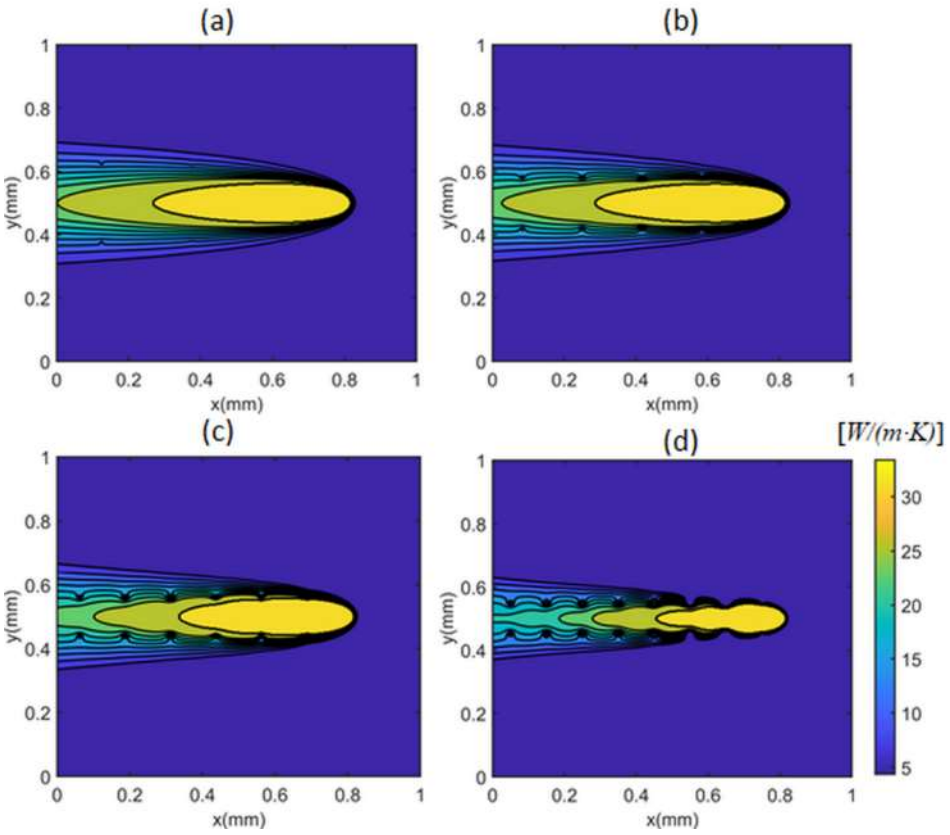

Figure 47 Calculated variations on thermal conductivity due to the single-track scan with a different number of heat sinks. (a) 4x4=16 heat sinks (b) 5x5=25 heat sinks (c) 8x8=64 heat sinks (d)10x10=100. The moving laser is located at x = 0.8 mm y = 0.5 mm [97].

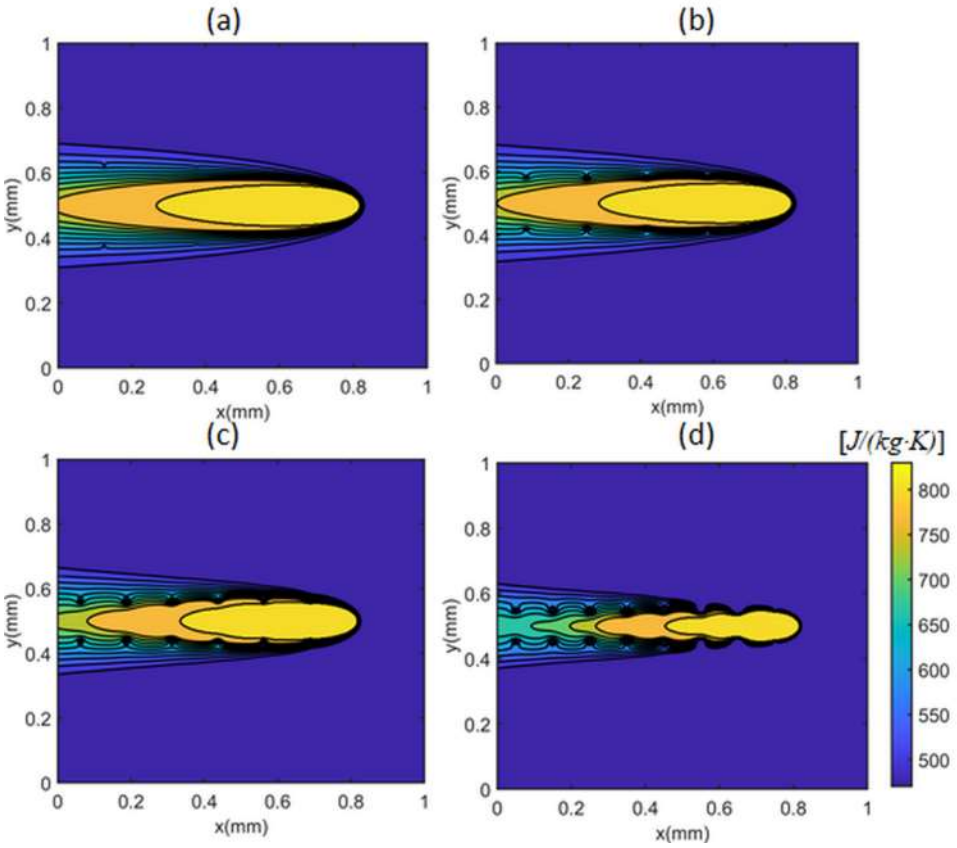

Figure 48 Calculated variations on specific heat due to the single-track scan with a different number of heat sinks. (a) 4x4=16 heat sinks (b) 5x5=25 heat sinks (c) 8x8=64 heat sinks (d)10x10=100. The moving laser is located at x = 0.8 mm y = 0.5 mm [97].

To determine the proper number of heat sinks, the calculated molten pool dimensions were compared to the documented values, which were experimentally measured based on the solidification microstructure as illustrated in Figure 49. The molten pool dimensions were calculated by comparing the predicted temperature to the material melting temperature as illustrated in Figure 50, where *L, W, D* represents the molten pool length, molten pool width, and molten pool depth respectively.

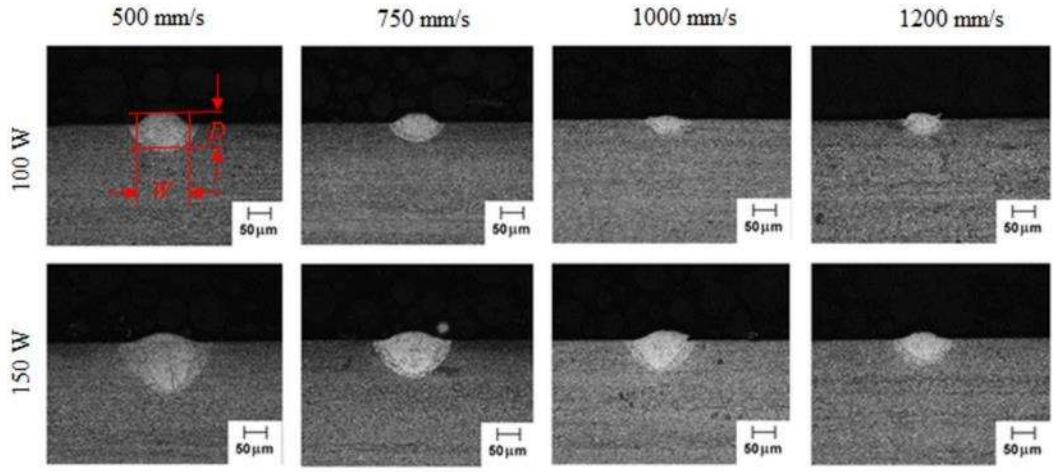

Figure 49 Experimental measurements of molten pool dimension based on the solidification microstructure [98].

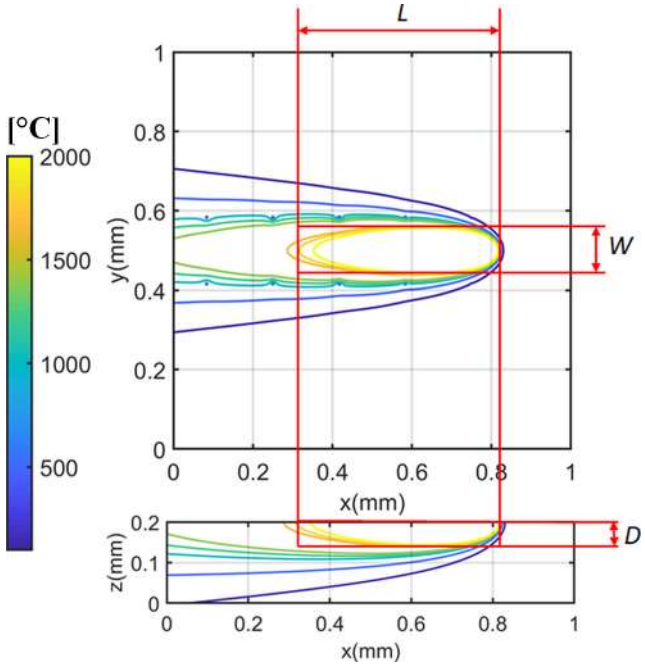

Figure 50 Calculation of molten pool dimensions from a three-dimensional temperature profile [97].

As shown in Figure 51, the closest agreement was observed with 6x6 heat sinks under test 1 condition. The horizontal axis 0x0 denotes the calculated molten pool dimensions without a heat sink. In other words, the heat loss from the part boundary was

not considered. Exp denotes the experimental molten pool dimensions. The more heat sinks, the smaller the molten pool dimension, which is consistent with the heat-affected zone dimensions. This trend confirms the instinctive trend that the more heat loss, the smaller the heat-affected zone and molten pool, and vice versa.

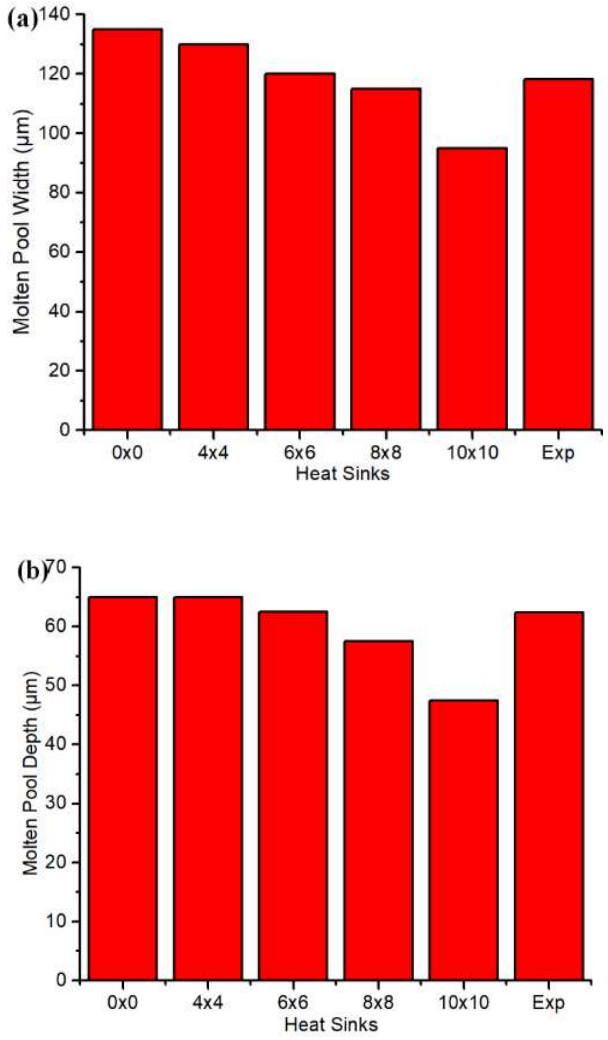

Figure 51 Determination of the number of heat sinks from the comparison between calculated molten pool dimensions and experimental measurement. Exp denotes experimental values under test 1 condition [97].

With a 6x6 heat sink setting, the molten pool dimensions were predicted under 8 different process conditions in Table 15. The predicted molten pool dimensions were

validated with the experimental measurements. The continuity of the scan tracks was confirmed from the observation on top view. The experimental measurement was made at least in triplicate with negligible variation observed under each process condition. A close agreement was observed as shown in Figure 52. The deviation might be caused by the simplified point heat source solution without considering the heat source profile, the adopted absorptivity and materials properties.

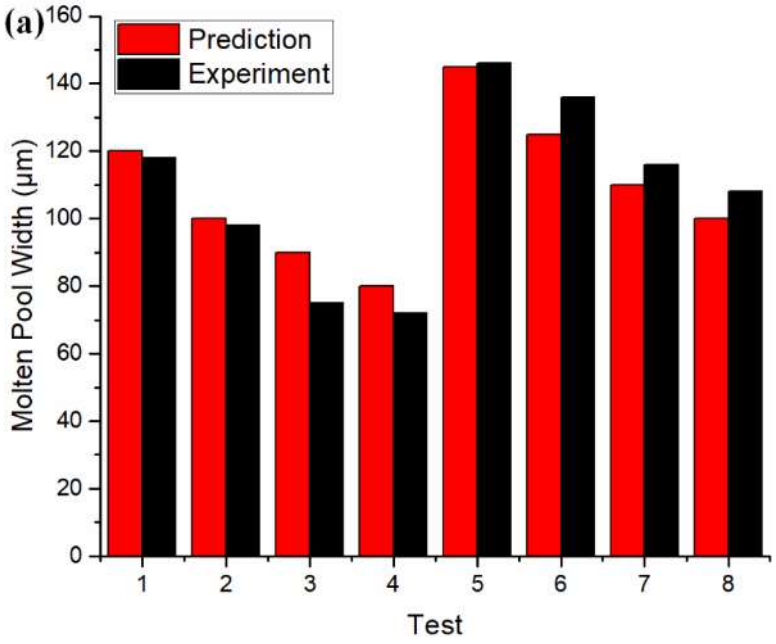

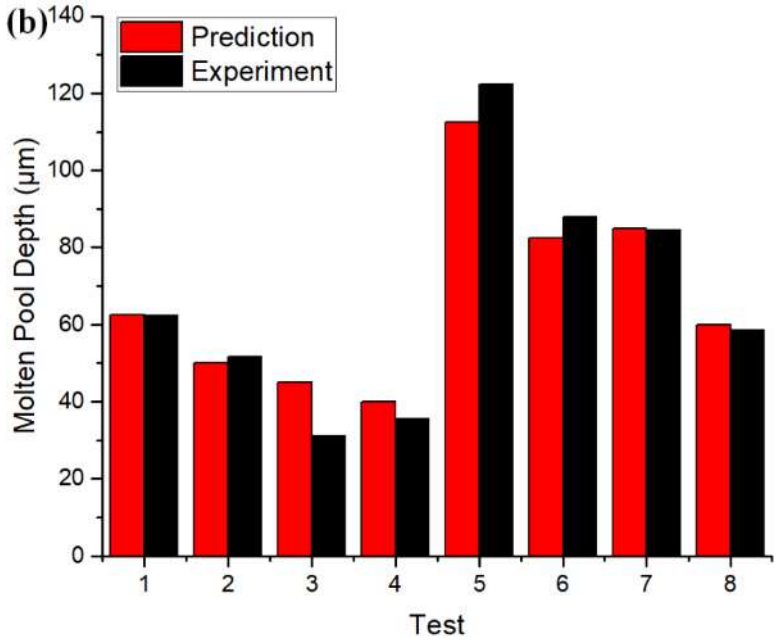

Figure 52 Validation of calculated molten pool dimension to the experimental measurement under different process conditions. (a) molten pool width, (b) molten pool depth.

The presented model was also tested with a low-power regime in PBMAM. The Laser scanning velocity was 200 mm/s. The scanning velocity varied from 20 W to 80 W. The calculated temperatures were validated to experimental measurements as shown in Figure 53, where the red, blue, and black colors represent calculations from analytical model, calculations from numerical model and experimental measurements respectively. Good agreements were observed for calculations from both analytical model and numerical model upon validation to experimental measurements. Moreover, the computational time of temperature calculation under each process condition with the proposed model by a personal computer running at 2.8 GHz was about 150 s. For comparison, the FE model needed a few hours for each temperature prediction depending on the mesh elements size for a part with a similar size [45].

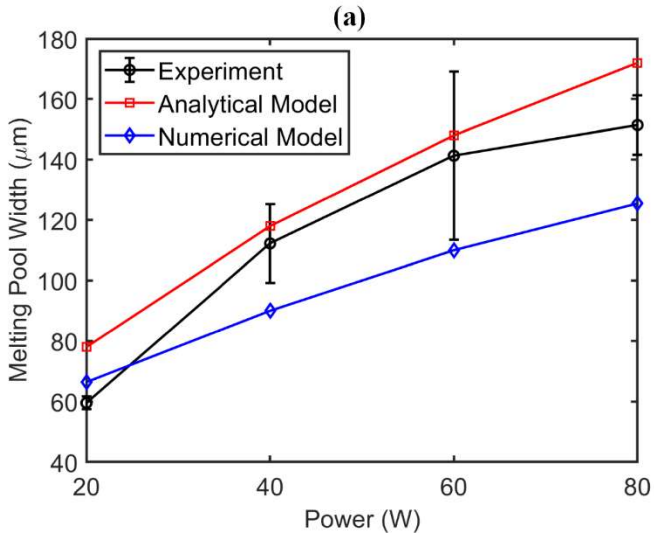
(a)
Experiment
Analytical Model
Numerical Model
Melting Pool Width (μm)
Power (W)
180
160
140
120
100
80
60
40
20
40
60
80

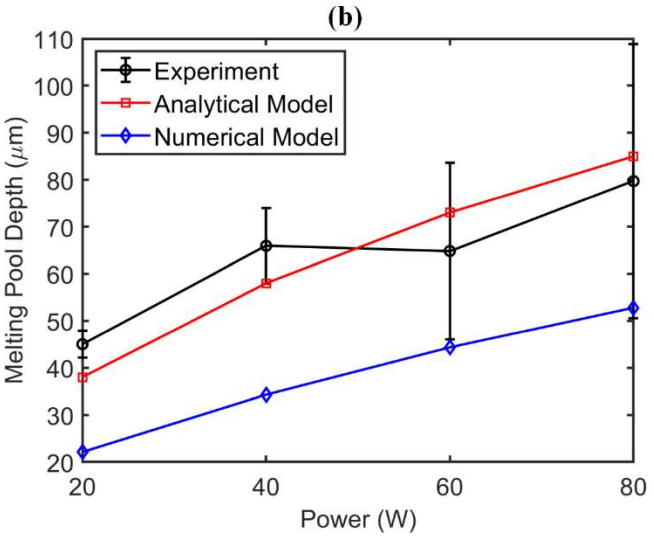
(b)
Experiment
Analytical Model
Numerical Model
Melting Pool Depth (μm)
Power (W)
110
100
90
80
70
60
50
40
30
20
20
40
60
80

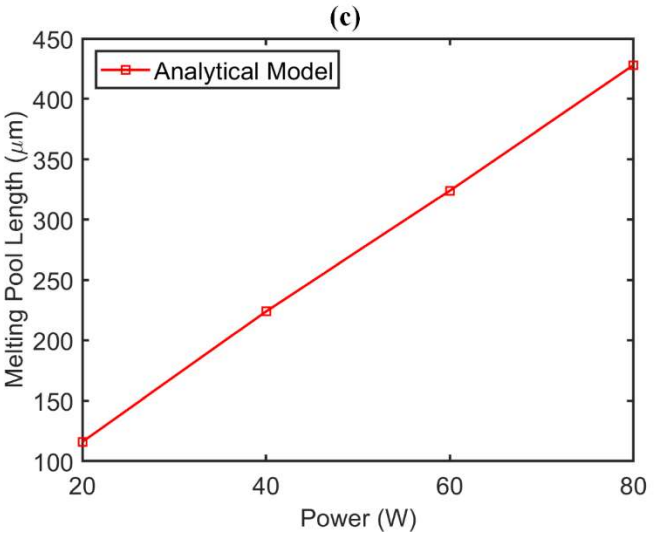
(c)
Analytical Model
Melting Pool Length (μm)
Power (W)
450
400
350
300
250
200
150
100
20
40
60
80

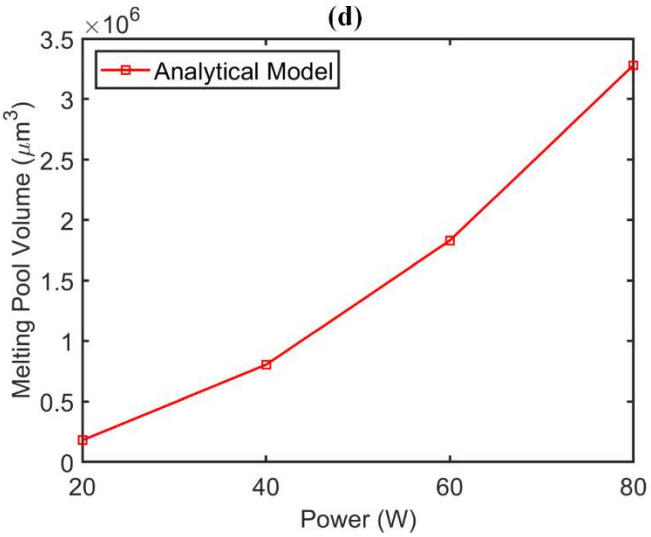

Figure 53 Molten pool dimensions under various process conditions. (a) Molten pool width. (b) Molten pool depth. (c) Molten pool length. (d) Molten pool volume [99].

Furthermore, the heat sink solution was employed in the temperature calculation in PFMAM of Ti6Al4V. The temperature evolution and molten pool evolution were calculated in a single-track scan. The stabilized temperature profiles were calculated in the scan of multiple layers. The process parameters are given in Table 16.

Table 16 Process condition and build geometry in PFMAM of Ti6Al4V.

Name	Value	Unit
Power (P)	600	W
Absorption (η)	0.7	1
Scanning velocity (V)	6	mm/s
Wall length (L)	40	mm
Layer thickness (t_L)	0.35	mm
Wall width (W)	2.114	mm

The molten pool evolution was investigated using the presented model with respect to laser travel distance from its starting location during a single-track scan during heating stage. The temperature evolution in the single-track scan is illustrated in Figure 54. The workpiece material was assumed to be isotropic and homogeneous with the initial temperature at room temperature. The calculated region had a size of 1.4 mm (4 layers) in height (z-direction) and 4 mm in length (x-direction) with an increment of 0.01mm in both directions. The molten pool dimensions including molten pool length and molten pool depth were then obtained as illustrated in Figure 55. The laser travel distance was given as 0.01 mm, 0.1 mm, 1 mm, 3 mm, 5 mm, 10 mm, 15 mm, 20 mm respectively. A stabilized molten pool was observed after 10 mm.

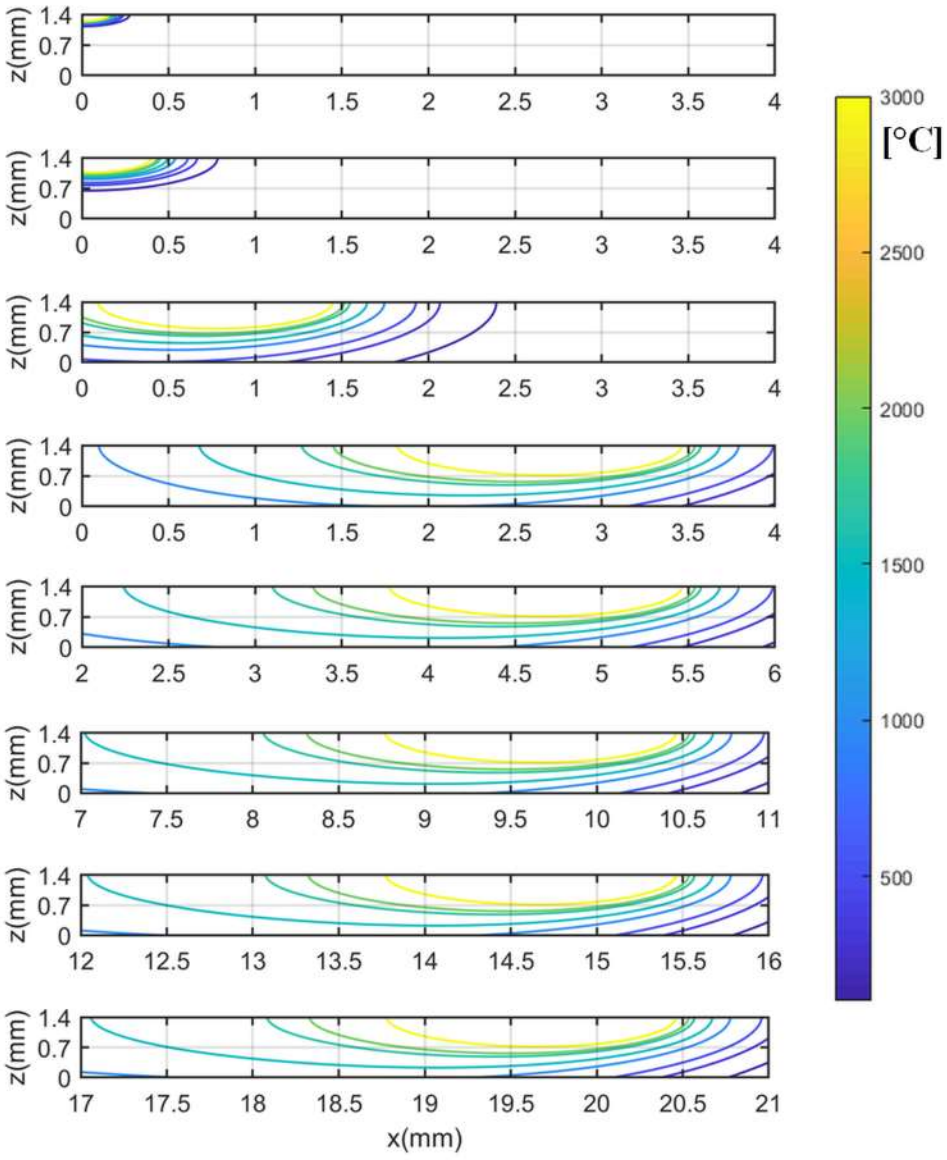

Figure 54 Temperature evolution during a single-track scan [100].

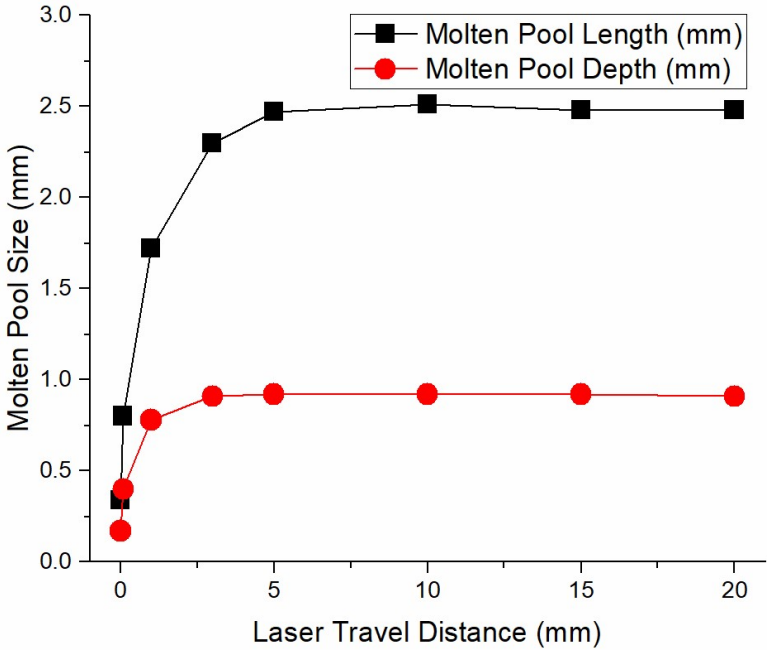

Figure 55 Molten pool evolution during the single-track scan in powder feed metal additive manufacturing [100].

The stabilized molten pool dimensions were then predicted in printing an 8-layer thin-wall structure, namely in 2nd, 4th, 6th, and 8th layers. The stabilized temperature profiles in the 4th layer and 8th layer are illustrated in Figure 56. The non-smooth temperature contour was caused by the coarse incremental resolution and the consideration of the influence of the heat-affected zone in previous layers.

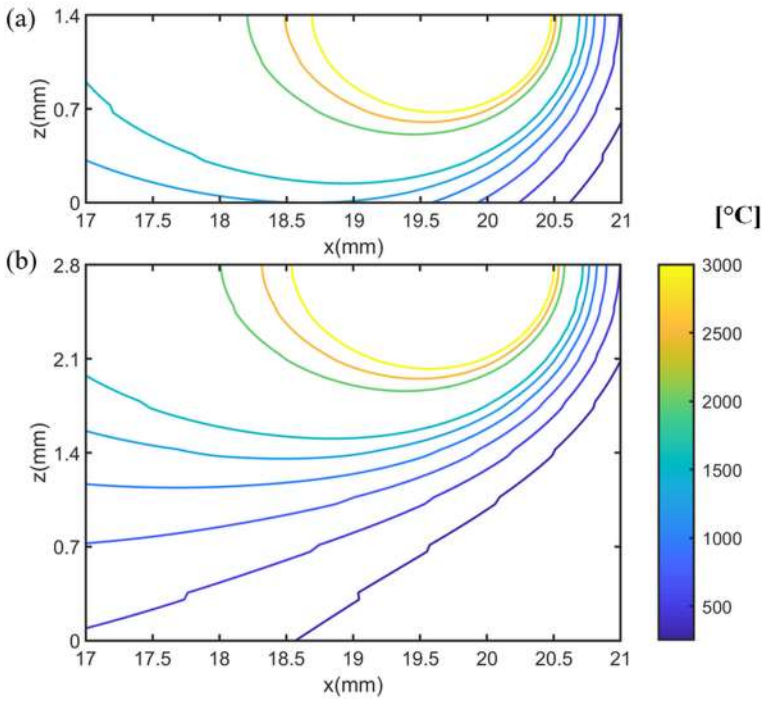

Figure 56 Stabilized temperature profile during (a) the 4th-layer scan and (b) the 8th layer scan [100].

The predicted molten pool dimensions were validated to the experimental measurements using an infrared camera based on the relationship between a pixel and a known distance. The Nd: YAG laser was used in a coaxial regime with Ti6Al4V powder distribution in the range of 25-45 μm. The laser spot size at 5 mm working distance was 1.5 mm in diameter. The average feed rate was used as 2 g/min. Meantime, a high-speed camera (Fastcam Photron) was used to record the stabilized molten pool dimensions at 1000 Hz. Close agreements were observed from the validation as shown in Figure 57, where the error bars for the predicted values and experimental values were determined by the incremental resolution in prediction (± 0.05 mm) and IR camera resolution (± 0.017 mm) respectively. The error bars for predicted values were determined as ± 0.05 mm due to the incremental resolution in temperature prediction. The error bars for experimental

values were determined as ± 0.017 mm due to the resolution of the IR thermal camera. The slightly underestimated results might be caused by the inversely determined absorption value

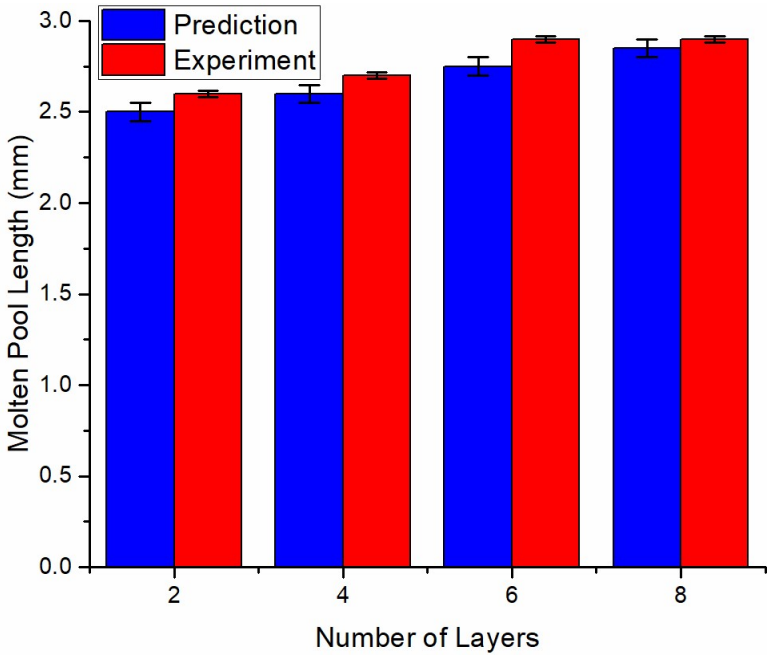

Figure 57 Validation of calculated molten pool dimensions during multi-layer scanning for a thin-wall structure [100].

The influence of wall width on the temperature profile and molten pool dimensions was investigated with various wall thickness values. The obtained molten pool length and depth were shown in Figure 58. An increasing trend was observed for molten pool dimensions with increasing wall width, and vice versa. The influence of wall thickness became negligible when it was over 10 mm because the heat loss due to convection and radiation took place at the part boundary, and the boundary was far from the laser source location at the middle of width for a thick-wall structure.

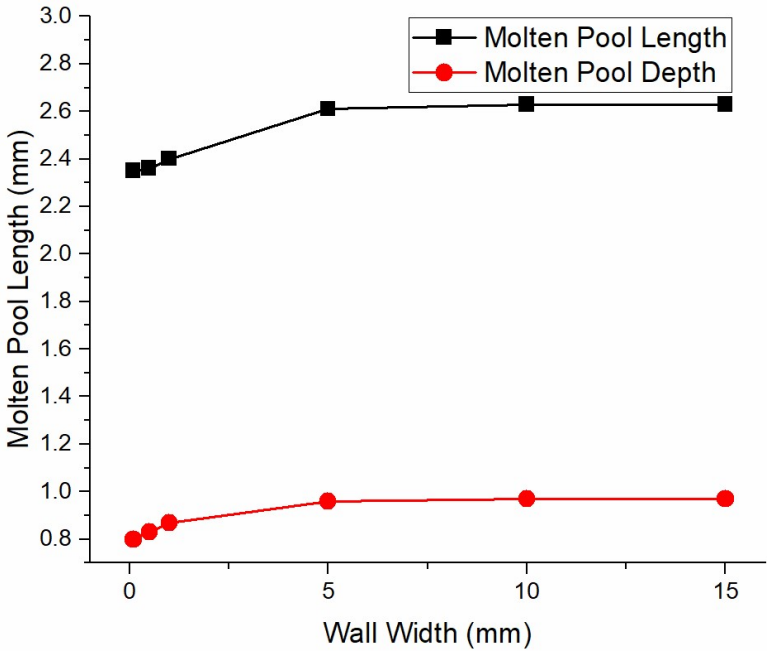

Figure 58 The influence of wall width on calculated molten pool dimensions (wall width = 0.1, 0.5, 1, 5, 10, 15 mm) [100].

Furthermore, the developed was employed for the temperature prediction in PFMAM of Inconel 718 alloy during the heat stage and cooling stage. The heat source solution was activated during the heating stage and deactivated during the cooling stage, while the heat sink solution was activated all the time. The materials properties of Inconel 718 alloy are given in Table 17.

Table 17 Materials properties of Inconel 718 alloy in PFMAM [101].

Name	Symbol	Value	Unit
Density	ρ	8820	kg/m^3
Thermal conductivity	k	11	W/(m·K)
Specific heat	c	420	J/(kg·K)
Latent heat	H_f	210000	J/Kg
Room temperature	T_0	25	°C
Solidus temperature	T_s	1260	°C
Liquidus temperature	T_l	1533	°C
Heat convection coefficient	h	25	W/(m^2·K)
Emissivity	ε	0.8	1
Stefan-Boltzmann constant	σ	5.67 10^{-8}	W/(m^2·K^4)

To investigate the relationship between laser scanning location and the influence of heat transfer boundary condition, the temperature profiles were predicted in multiple single-track scans at different locations on part 1 considering bounded medium and semi-infinite medium as illustrated in Figure 59, where the solid lines represented the predicted temperature profiles considering heat loss for the bounded medium; the dashed line represented the predicted temperature profiles neglecting the heat loss for semi-infinite medium. The red stars denote the center of each heat sink, where the heat sink temperatures were estimated using the point heat source solutions. The number of heat sinks on part with

5mm by 5 mm by 2 mm was empirically determined as 1 per mm2. Temperature profiles were plotted as top views at five different laser locations, specifically (a) x = 4 mm y = 0.5 mm (b) x = 4 mm y = 1.5 mm (c) x = 4 mm y = 2.5 mm (d) x = 4 mm y = 3.5 mm (e) x = 4 mm y = 4.5 mm. A significant discrepancy was observed between predictions considering heat loss and predictions neglecting heat loss. The closer the scan location to the part boundary (y = 0 mm and y = 5 mm), the greater the discrepancy of the temperature profile and thus the greater the influence of heat loss, and vice versa.

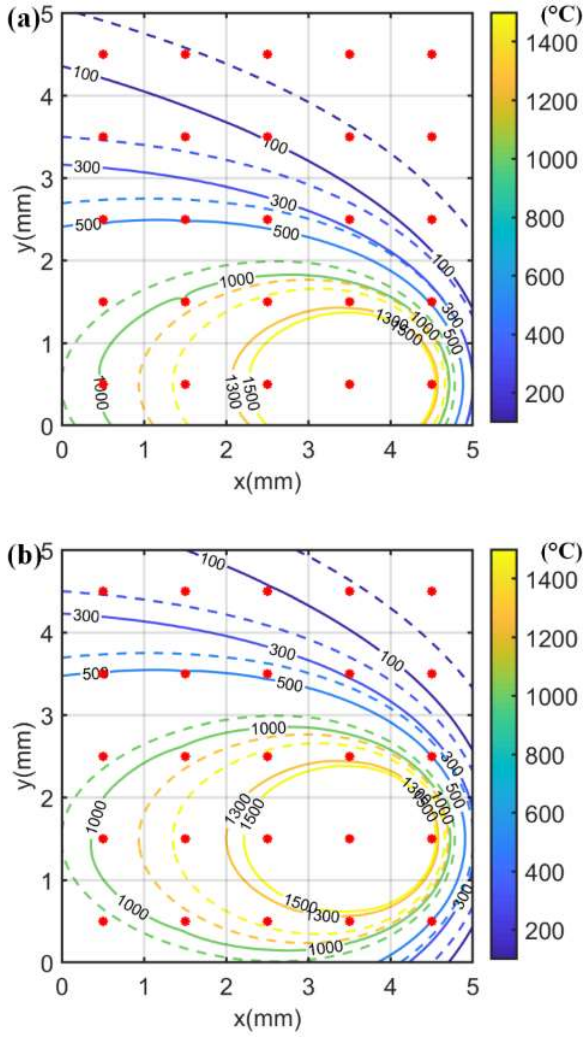

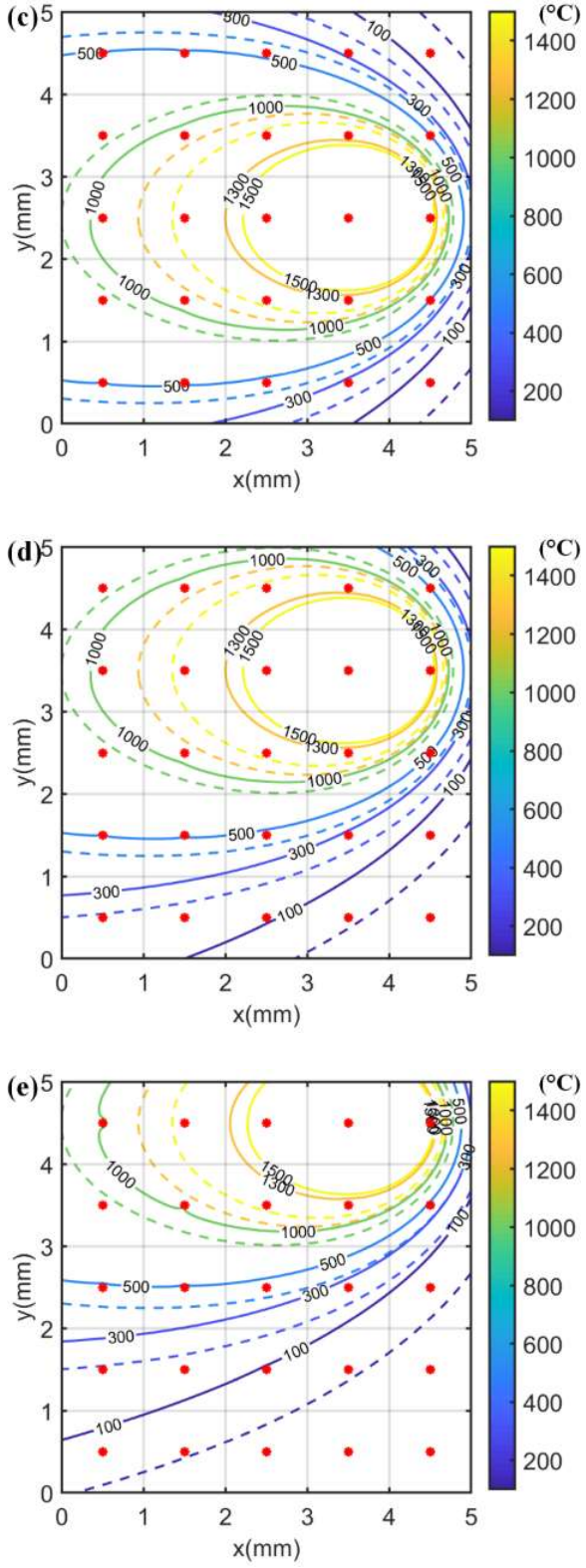

Figure 59 Calculated temperatures with various laser scanning locations in the y-direction [101].

In addition, the molten pool length and depth were calculated by comparing it to the material melting temperature. The symmetric pattern was observed for molten pool dimensions at symmetric scan locations as illustrated in Figure 60.

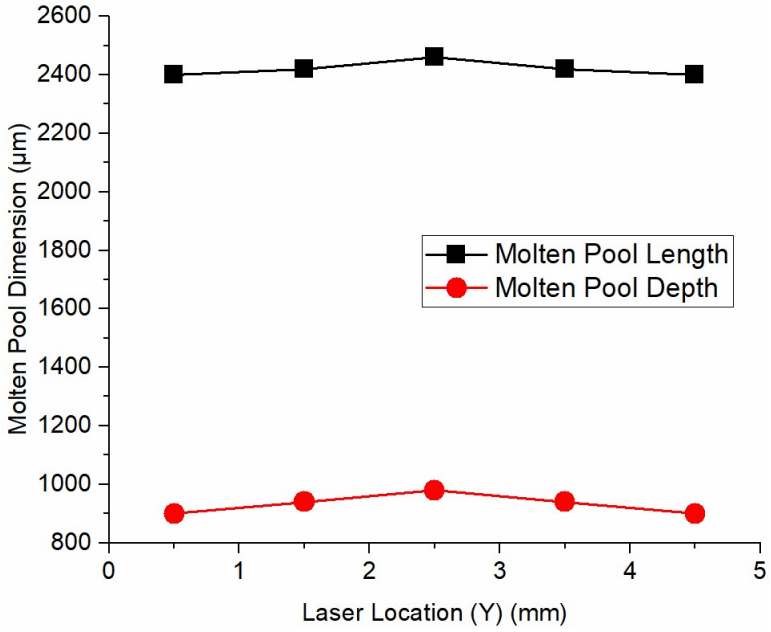

Figure 60 Calculated molten pool dimensions considering bounded medium with various laser scan location (x = 4 mm, y = 0.5, 1.5, 2.5, 3.5, 4.5 mm) [101].

The temperature solution is constructed from the superposition of moving point heat source solution and heat sink solution based on a stationary coordinate with respect to the part boundary. The heat source solution is activated during the heating stage and deactivated during the cooling stage. The temperature evolution was predicted in a single-track scan during the heating stage and cooling stage of PFMAM as illustrated in Figure 61. The molten pool evolution was calculated by comparing the predicted temperature profiles to the material melting temperature. The molten pool growth and stabilization during heating state and shrinkage during the cooling stage are shown in Figure 61.

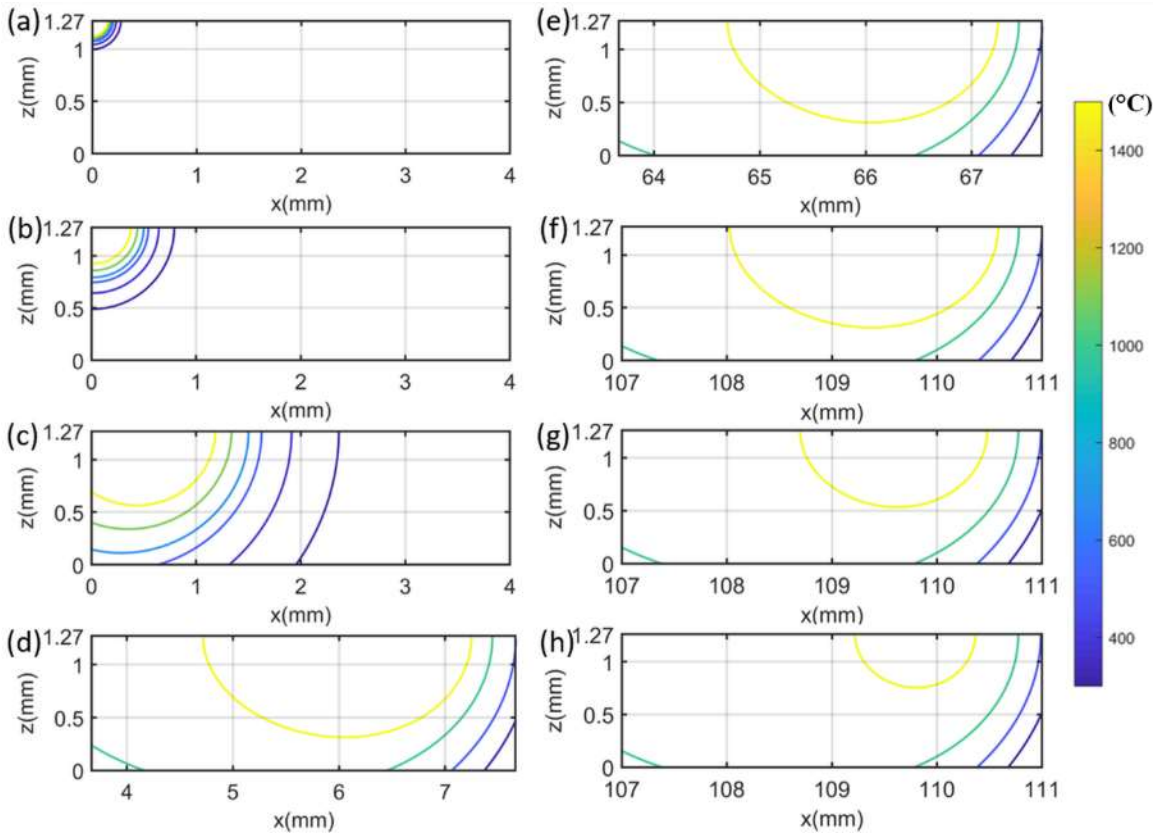

Figure 61 Calculated temperature evolution during heat state and cooling state of PFMAM for part 2 at (a) 0.001 s (b) 0.01 s (c) 0.1 s (d) 1 s (e) 10 s (f) 16.5 s (g) 21.5 s (h) 31.5 s. Note: The cooling stage starts from 16.5 s [101].

The molten pool evolution was calculated by comparing the predicted temperature profiles to the material melting temperature. The molten pool growth and stabilization during heating state and shrinkage during the cooling stage are shown in Figure 62.

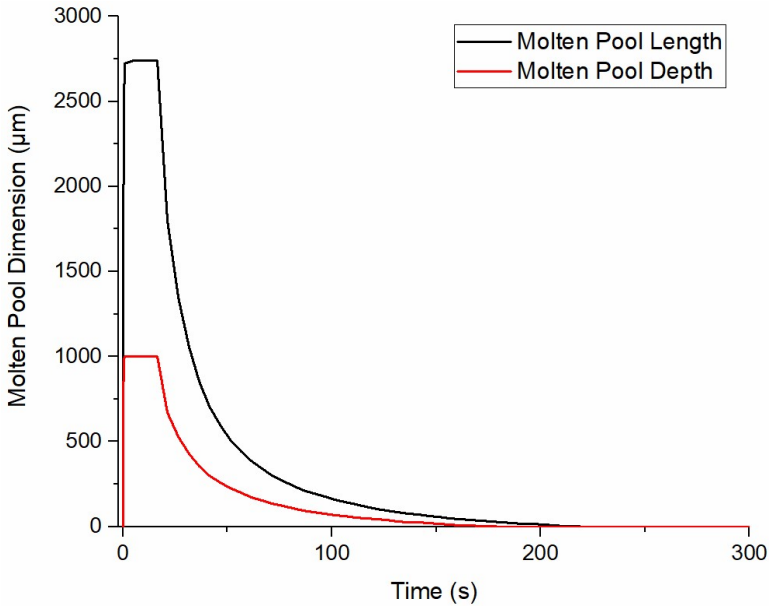

Figure 62 Calculated molten pool evolution during the heating stage and cooling stage of PFMAM in the single-track scan for part 2 [101].

The heat loss from the top boundary of the substrate was neglected due to the small distance from the measurement location to the build, and relatively lower temperature. Close agreements were observed between the predicted temperatures and the experimental measurement as illustrated in Figure 63, where red dash lines denote calculated temperature. Black solid lines denote experimental temperature. The temperature drop before the cooling state was observed because of increasing distance from the moving laser to the thermocouple location. The temperature drop during the cooling stage was observed because of the heat loss from convection and radiation.

The experimental peak temperature and predicted peak temperature during the heating state were 521.2 °C and 495.6 °C respectively as illustrated in Figure 9a. The prediction error on peak temperature was 4.91 %. The slight mismatch between prediction and measurement might be caused by the employed point moving heat source, which

neglected the influence of the laser beam profile. The laser beam profile should be considered as future works to further improve the prediction accuracy. In addition, the temperature-independent materials properties, and the simplified rectangular-shaped workpiece, and the chosen number of heat sinks might also affect the deviation between prediction and experimental measurement.

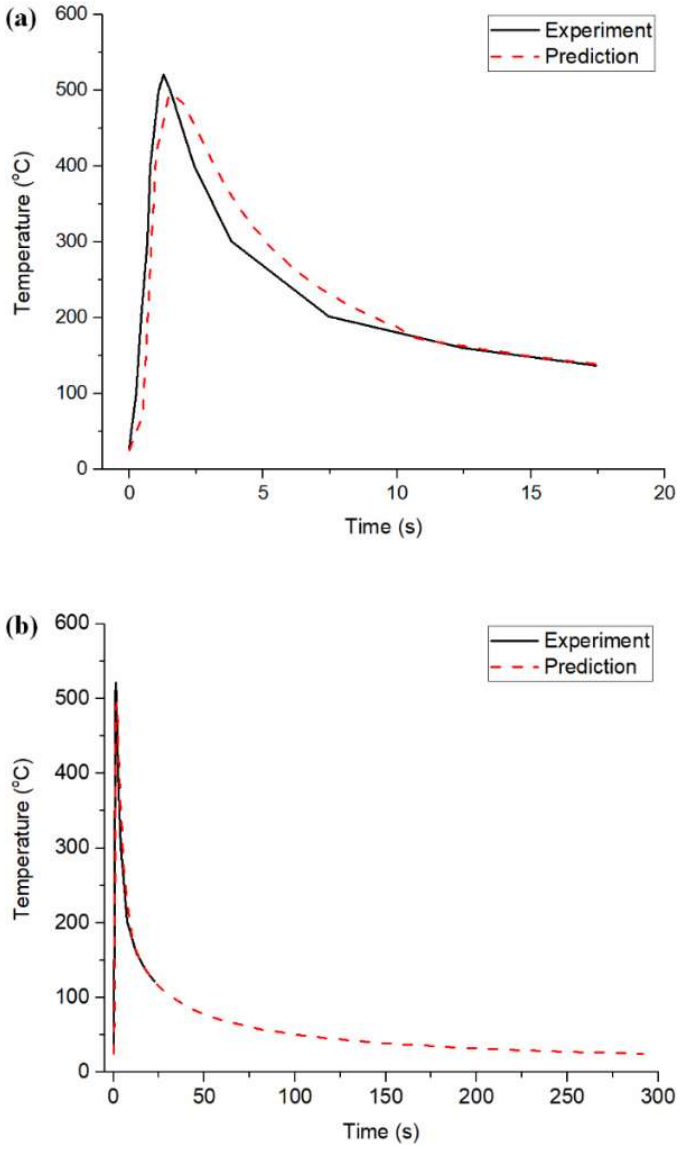

Figure 63 Validation of temperatures during (a) heating stage and (b) heating and cooling stages to the experimental measurements using a K-type thermocouple placed on the substrate (x = 55 mm y = 3mm z = 0 mm). [101].

4.2.3 Thermal Modeling in Metal Additive Manufacturing Considering Powder Size Distribution and Powder Packing

This section presented an analytical thermal model with consideration of powder statistical size distribution and powder packing. The presented model was investigated in the PBDMAM of AlSi10Mg alloy. The heat transfer boundary condition was also considered with a heat sink solution. The powder size distribution of AlSi10Mg is shown in Figure 64. The material properties of AlSi10Mg are given in Table 18.

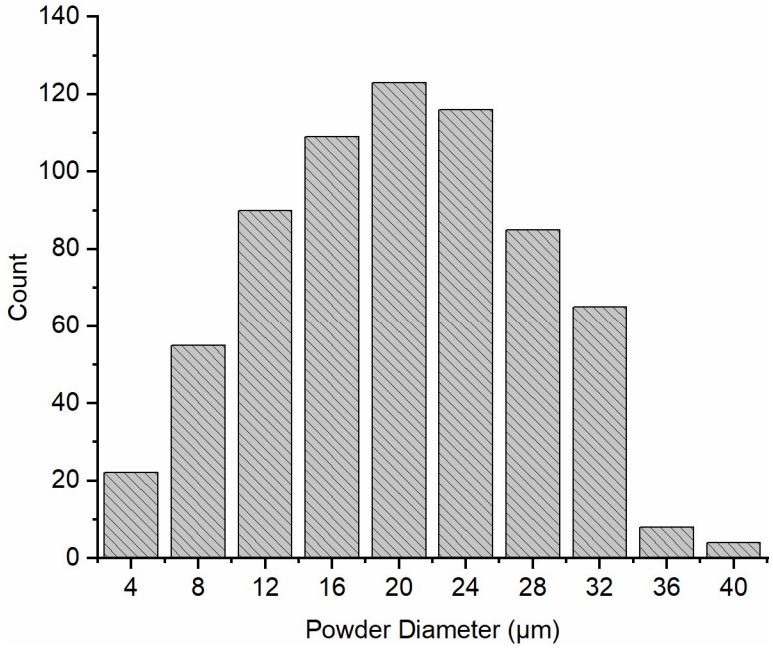

Figure 64 The powder size distribution of AlSi10Mg powders in this study.

Table 18. Materials properties of AlSi10Mg and process parameters in powder bed metal additive manufacturing [102].

Parameter	Symbol	Value	Unit
Solid bulk density	ρ_s	2680	kg/m^3
Solid bulk specific heat	C_s	1024	J/(kgK)
Solid bulk thermal conductivity	k_s	233	W/(mK)
Heat transfer coefficient	h	82	W/(m^{2}K)
Radiation emissivity	ε	0.4	1
Stefan-Boltzmann constant	σ	$5.67 \cdot 10^{-8}$	W/(m^{2}K^4)
Room temperature	T_0	293.15	K
Solidus temperature	T_s	830.15	K
Liquidus temperature	T_l	870.15	K
Laser power	P	180	W
Laser scan velocity	V	600-1600	mm/s
Absorption	η	0.3	1

Spherical powders were generated based on the probability distribution curve and packed using advancing front approach as illustrated in Figure 65. The first three circles are generated as the initial front with the densest packing in the center of the given region. The additional circles are generated on the right-hand side of the vectors (1-2, 3-1, 3-1) from the initial front. The powder packing pattern was predicted using the advancing front method as illustrated in Figure 66, in which the red circles and white irregular shapes

represent packed powders (solid) and void respectively. The influence of uncertainty in powder packing and the number of powders on void calculation was investigated with a sensitivity analysis, in which the powder packing structure was predicted three times at each level of powder numbers. The calculated powder volume fraction and void volume fraction are given in Table 19. The average void volume fraction, also known as power bed porosity, was used as 0.1648 in the current study.

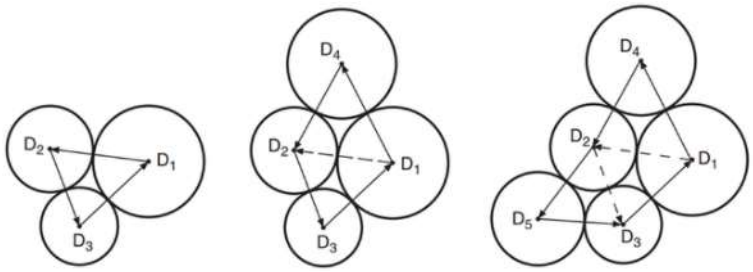

Figure 65 Schematic drawing of the advancing front approach for the calculation of powder bed packing pattern [103].

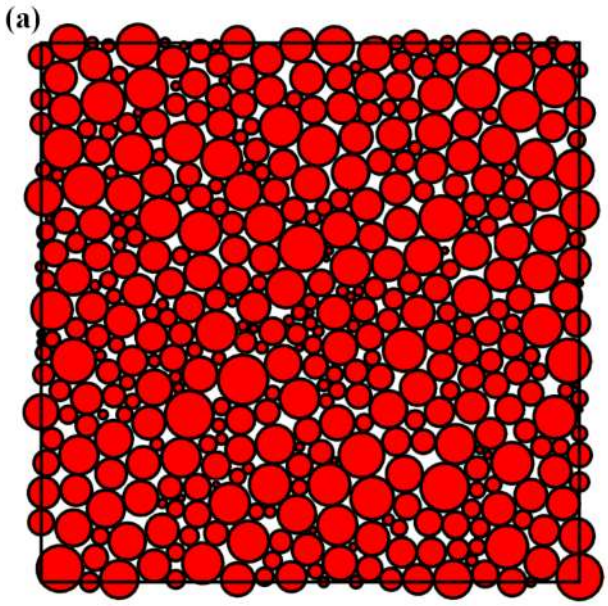

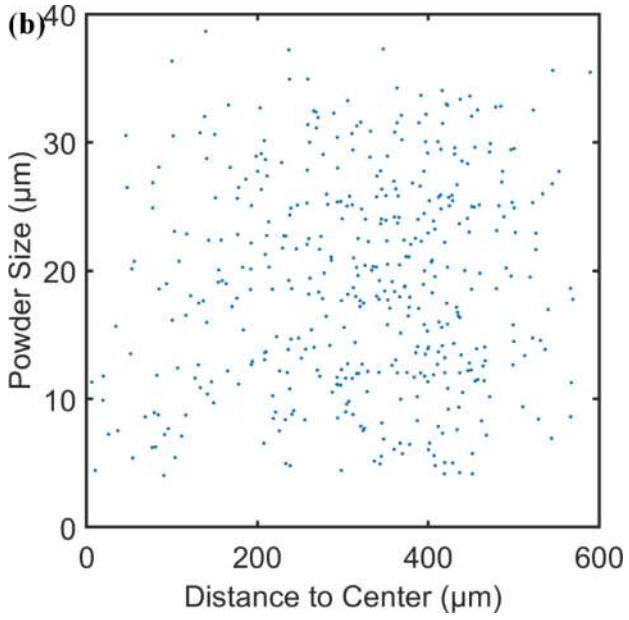

Figure 66 Predicted powder packing structure of ALSi10Mg in this study. (a) packing structure of 500 powders, (b) powder size and center location of 500 packed powders [102].

Table 19 Volume fractions of void and solid of packed powder bed with the various number of powders [102].

Number of Powders	Void Volume Fraction	Solid Volume Fraction
100	0.1676	0.8324
250	0.1636	0.8364
500	0.1685	0.8315
750	0.1625	0.8375
1000	0.1620	0.8380
Average	0.1648	0.8352

The specific heat of powders is not significantly different from the bulk materials properties according to the experimental measurement reported in the reference [104]. The powder bed density is calculated as the following.

$$\rho_p = (1-\varepsilon)\rho_s + \varepsilon\rho_g \tag{21}$$

where ρ_p is the powder bed density, ρ_s is the solid bulk density, ρ_g is the density of gas atmosphere (The density of air is 1.225 kg/m^3), ε is the volume fraction of voids.

$$k_p = \frac{k_s(1-\varepsilon)}{1+\psi\frac{k_s}{k_g}} \tag{22}$$

$$\psi = 0.02 \times 10^{2(\varepsilon-0.3)} \tag{23}$$

where k_p is the powder bed thermal conductivity, k_s is the bulk thermal conductivity, k_g is the thermal conductivity of the gas atmosphere, and ψ is an exponential factor, ε is the volume fraction of voids.

The temperature distribution was predicted with respect to the scanning time and laser traveling distance from the beginning point. The temperature distribution at t = 0.0001 ms, 0.001 ms, 0.01 ms, 0.1 ms, 1 ms, 10 ms, 20 ms, 30 ms were predicted using the presented model under test 1 process condition (P = 180 W, V = 600 mm/s) as illustrated in Figure 67. It should be noted that the color bar is corresponding to the temperature contour value in Kelvin. The temperature plots on x-y planes are the temperature profiles at the top boundary; the temperature plots on x-z planes are the temperature profiles at the cross-sectional area along the laser scanning direction. Laser scanning direction is along positive x-direction at y = 0 mm.

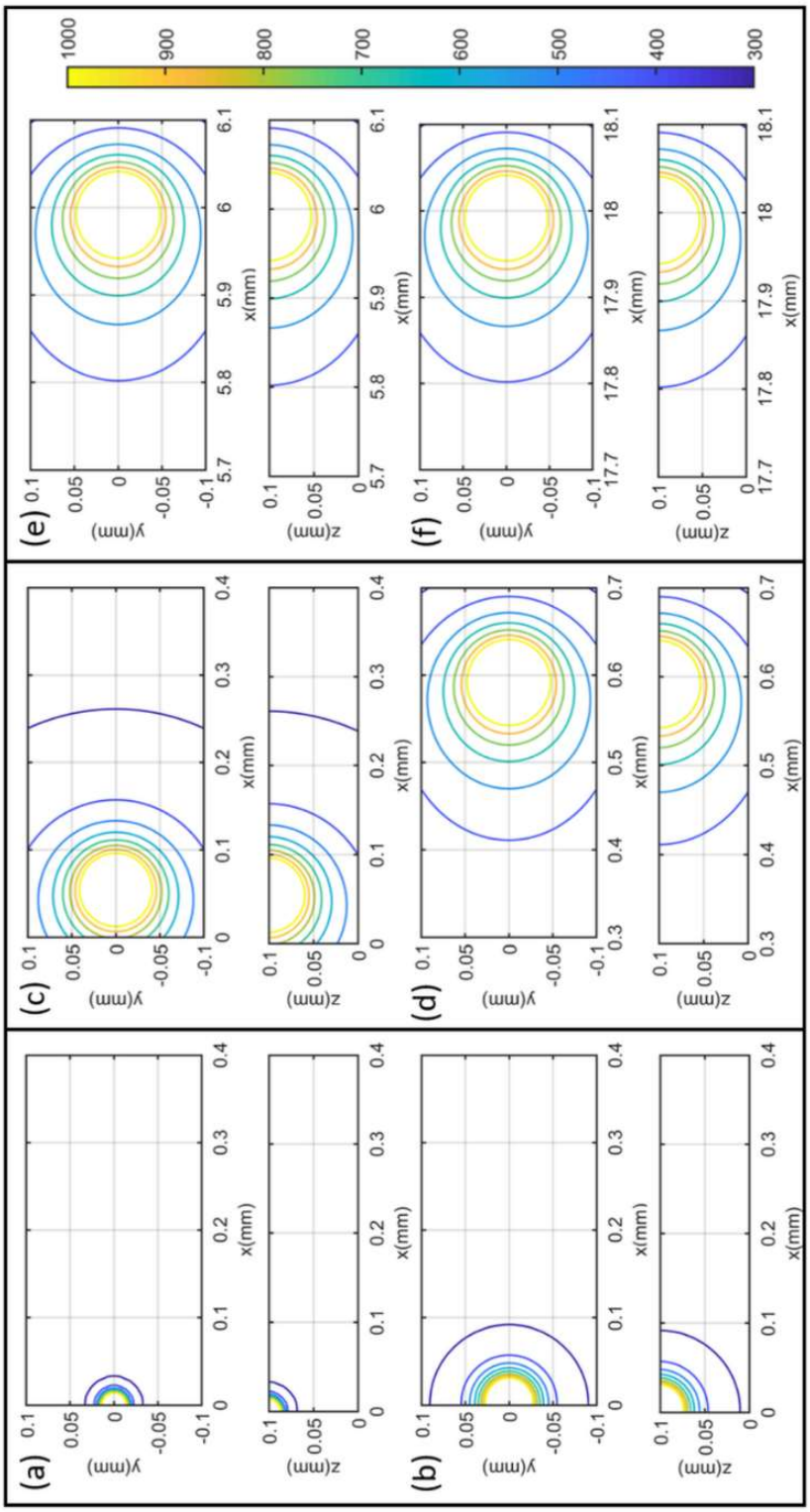

Figure 67 Temperature profiles during a single-track scan of PBMAM with P = 180 W, V = 600 mm/s at (a) 0.001 ms (b) 0.01 ms (c) 0.1 ms (d) 1 ms (e) 10 ms (f) 30 ms. The temperature unit is K [102].

The molten pool evolution during the single-track scan under test 1 process condition (P = 180 W, V = 600 mm/s). It should be noted that the cooling stage after laser turning off is not considered in the presented results. As shown in Figure 68, the time for molten pool stabilization using the developed model in the previous work and the presented model has no pronounced difference. However, the stabilized molten pool dimensions using the presented model were significantly larger than those using the previous model because the solid thermal conductivity is significantly higher than powder thermal conductivity without introducing the voids with high thermal resistance. High thermal conductivity materials require larger laser powder for the PBMAM process because the energy can be more easily dissipated into the surrounding area, which prevents the material melting and the formation of the molten pool.

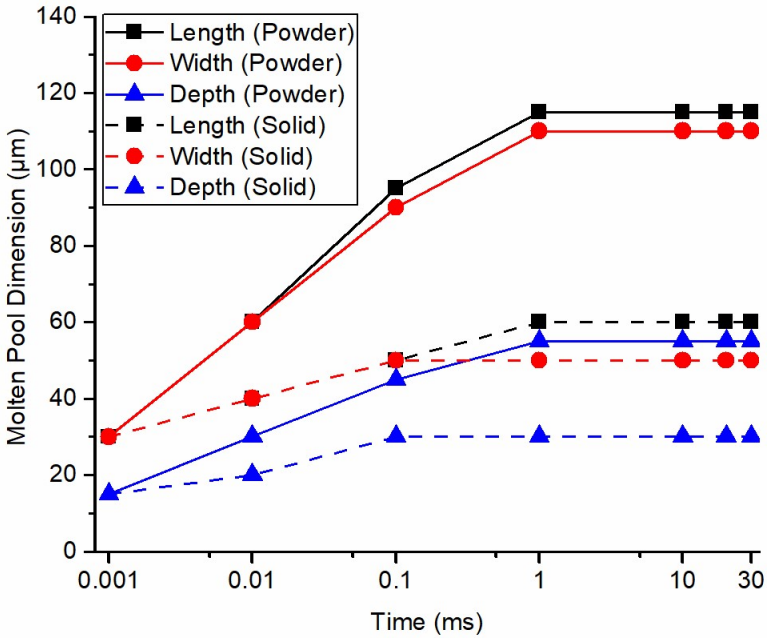

Figure 68 Comparison between calculated molten pool evolutions using solid material properties and powder materials properties [102].

To investigate the prediction accuracy, the stabilized molten pool dimensions from the prediction using the presented model were validated to the experimental measurement. Close agreements were observed between predictions and experimental values as shown in Figure 69.

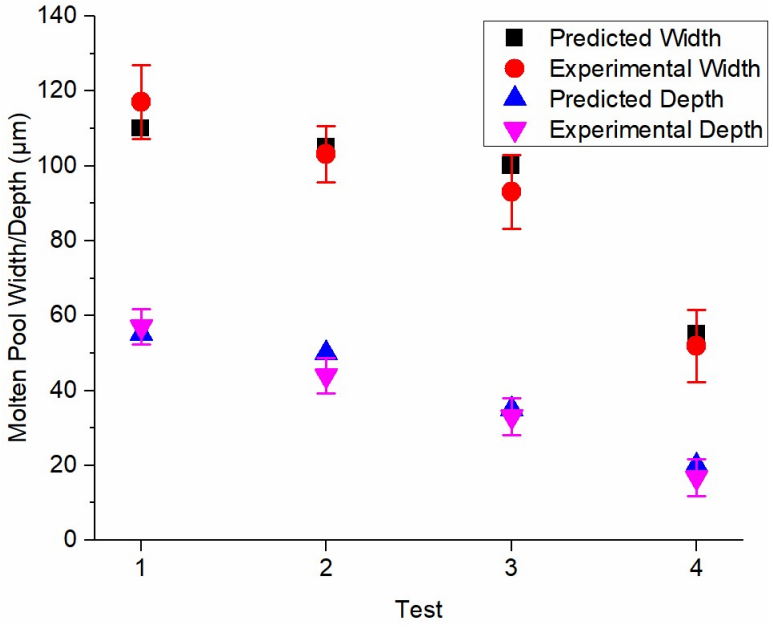

Figure 69 Validation of calculated molten pool dimensions to the documented experimental values based on the solidification microstructure. P = 180 W, V = 600 mm/s, 800 mm./s, 1000 mm/s and 1600 mm/s respectively [102].

In addition, the higher the laser scanning speed, the smaller the molten pool dimensions, and vice versa. This observed trend was confirmed with the experimental measurements. Moreover, the molten pool dimensions were also predicted using the presented model with various laser power setting as illustrated in Figure 70. The higher the laser power, the larger the molten pool size, and vice versa.

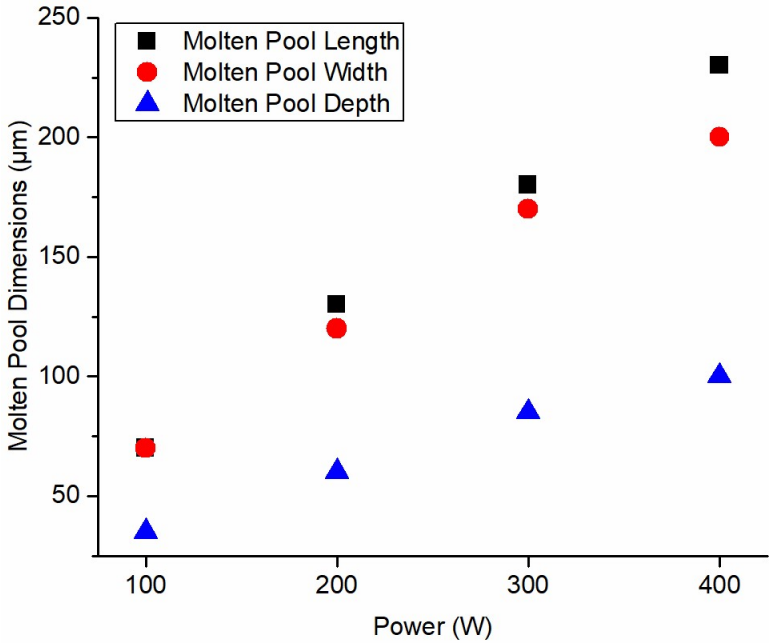

Figure 70 Predicted molten pool dimensions under various laser power settings. The laser scanning velocity was 600 mm/s [102].

4.3 Analytical Modeling of Part Porosity in Powder Bed Additive Manufacturing

4.3.1 Analytical Modeling of Part Porosity from Areal Thermal Analysis

This section presented a physics-based analytical modeling methodology for the prediction of the lack-of-fusion porosity in powder bed metal additive manufacturing (PBMAM) considering the molten pool geometry, powder size variation, and packing. The algorithm of the presented model is illustrated in Figure 71. A closed-form temperature model, which considers the moving laser heat source, boundary heat transfer, and laser power absorption, was employed to calculate the temperature profile and molten pool geometry with laser parameters and scan parameters. An advancing front approach was employed to calculate the powder packing pattern with statistical powder size distribution. The lack-of-fusion area and powder bed porosity were then obtained from image analyses.

The multiplication of lack-of-fusion area and powder bed porosity yields the prediction of part porosity due to lack of fusion.

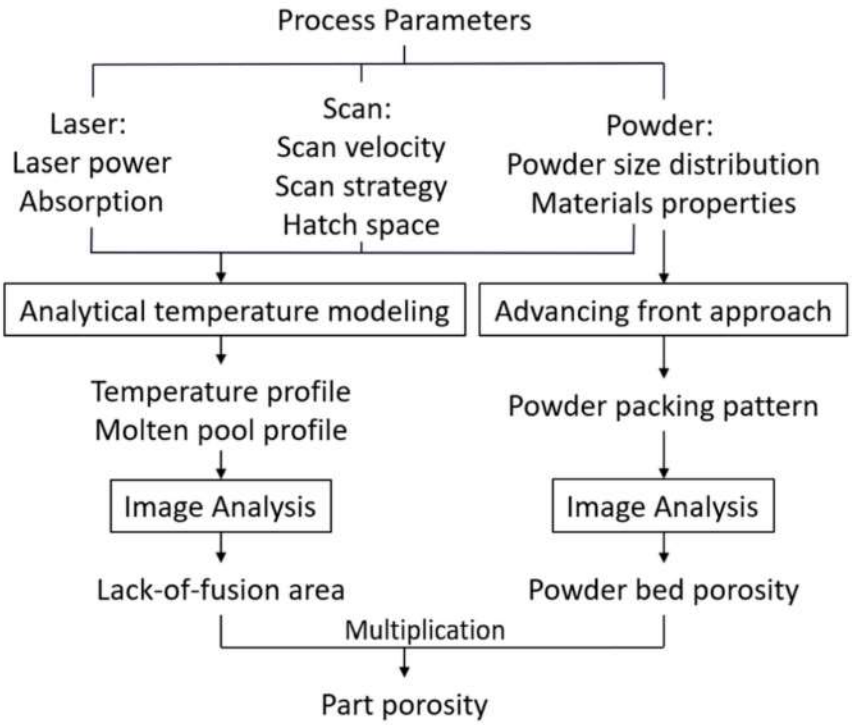

Figure 71 Algorithm of analytical modeling of part porosity in powder bed metal additive manufacturing [105].

The lack-of-fusion area was then calculated on the part cross-sectional area (on the y-z plane) normal to the scan path (in x-direction) as illustrated in Figure 72. A unidirectional scan strategy was used in the PBMAM. The track continuity and keyhole effect were investigated based on the single-track scans using metallographic analysis as illustrated in Figure 73, where part (a) has continuous track and stable molten pool formation, part (b), and part (c) have a discontinuous track with balling and keyhole effect respectively. The presented model calculates the part porosity as a result of lack-of-fusion. Therefore, the part porosity was not calculated under process conditions causing discontinuous track, balling effect, and keyhole effect.

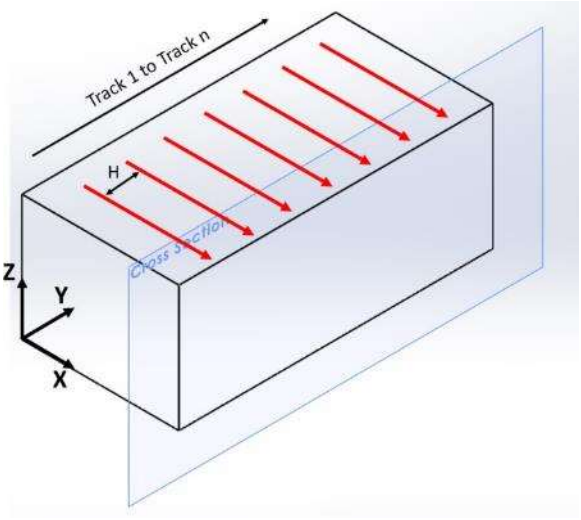

Figure 72 Schematic view of unidirectional scanning strategy on part cross-sectional view. H denotes hatch space between adjacent tracks [105].

Table 20 Process parameters of PBMAM of Ti6l4V [105].

Test	Power (W)	Scan Velocity (mm/s)	Part Porosity (%)
1	100	500	0 (full dense)
2	100	750	5.74
3	150	750	0 (full dense)
4	150	1000	0 (full dense)
5	150	1200	4.96
6	195	750	1.62
7	195	1000	0 (full dense)
8	195	1200	0 (full dense)

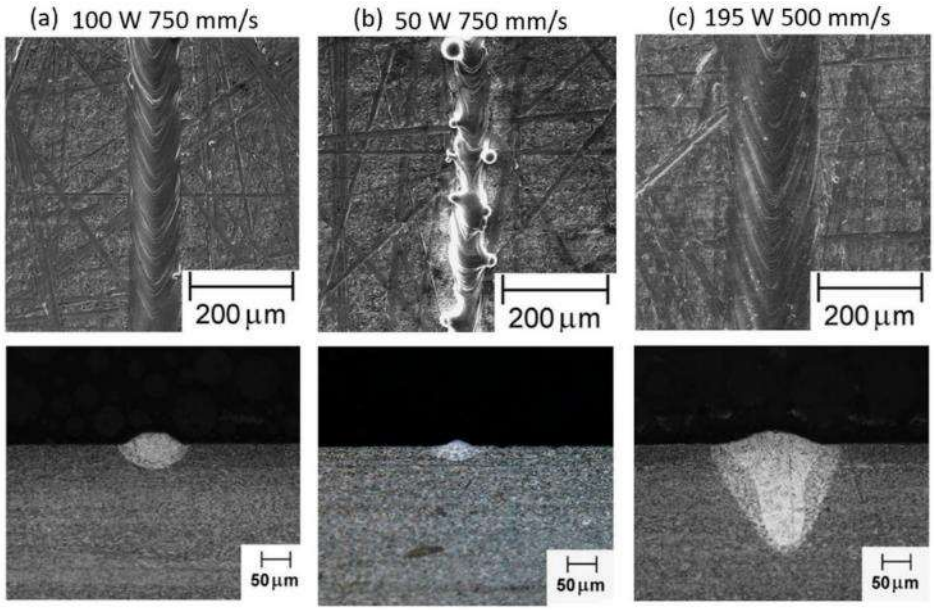

Figure 73 Scanning electron microscopy image of scanning tracks in single track scan at top view (upper) and optical microscopy image of cross-sectional view (lower) under various process conditions (a) 100 W 750 mm/s (b) 50 W 750 mm/s (c) 195 W 500 mm/s [98].

The part porosity values were calculated under 8 different process conditions, from which the continuous track and stable molten pool were observed. In other words, the lack-of-fusion part porosity dominates the formation of part porosity. The temperature transverse contours with multiple tracks were plotted on the cross-sectional area as illustrated in Figure 74, where the maximum value on the color bar represents the highest temperature contour value instead of the highest molten pool temperature. The molten pool transverse contours with multiple tracks were plotted to calculate the lack-of-fusion area as illustrated in Figure 75, where the yellow region and white region denote the molten pool area and lack-of-fusion area respectively.

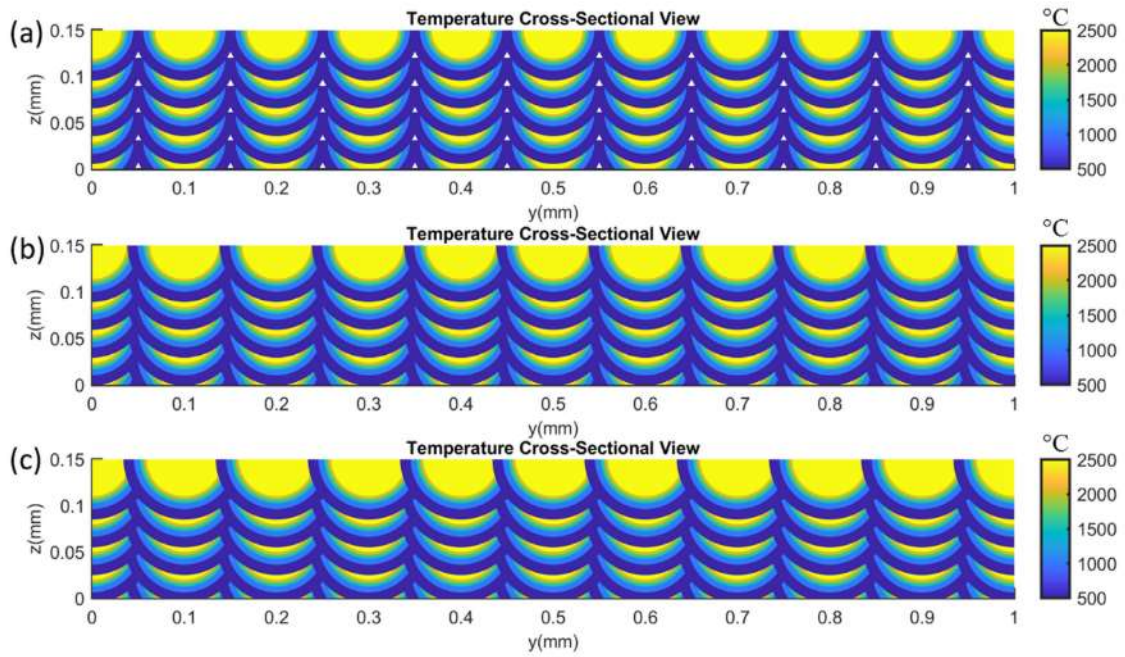

Figure 74 The plot of temperature contours on the part cross-sectional area (y-z plane) with multiple scans under various process conditions. t_L = 30 µm, H = 100 µm (a) 100 W 750 mm/s (b) 150 W 750 mm/s (c) 195 W 750 mm/s [105].

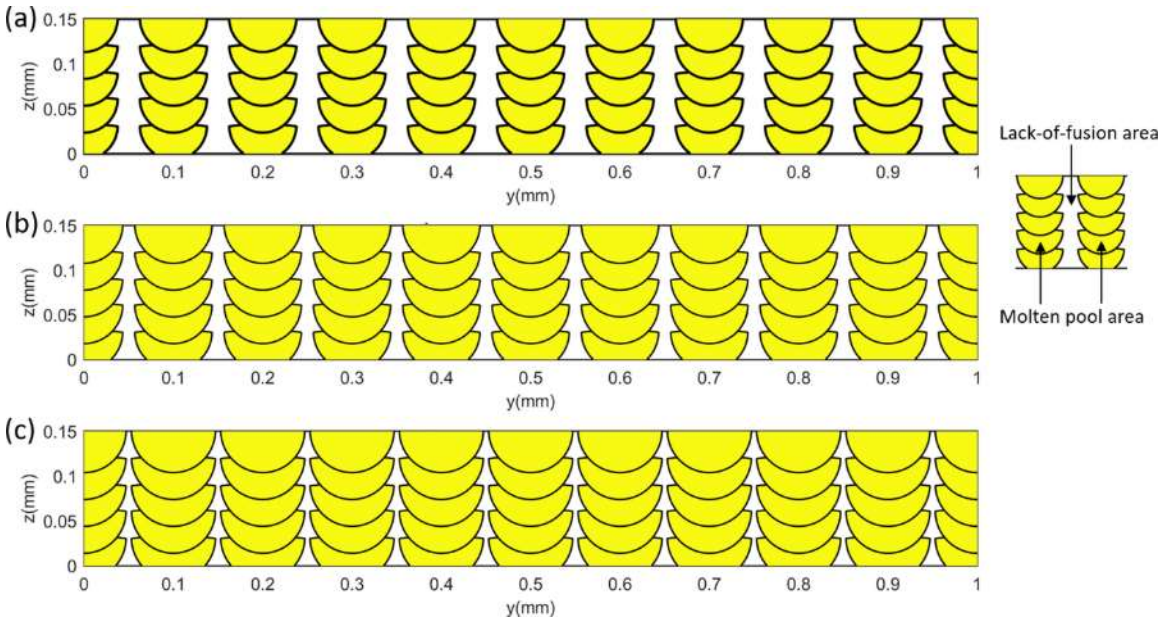

Figure 75 The plot of transverse sectional molten pool geometry on the part cross-sectional area (y-z plane). The molten pool contour was determined by comparing it to the materials melting temperature. t_L = 30 µm, H = 100 µm (a) 100 W 750 mm/s (b) 150 W 750 mm/s (c) 195 W 750 mm/s [105].

The calculated part porosity values were validated to the experimental measurements as illustrated in Figure 76. Acceptable agreements were observed with a maximum deviation of 6.31 %. The deviation of porosity calculation might be caused by the deviation of molten pool calculation, which assumed a point laser heat source with solid bulk material properties. The solid thermal conductivity is much larger than the powder thermal conductivity, which leads to faster temperature dissipation and thus smaller molten pool calculation, which cause the overestimation of part porosity. That effect became more significant with increasing laser power under test 6, 7, 8 conditions.

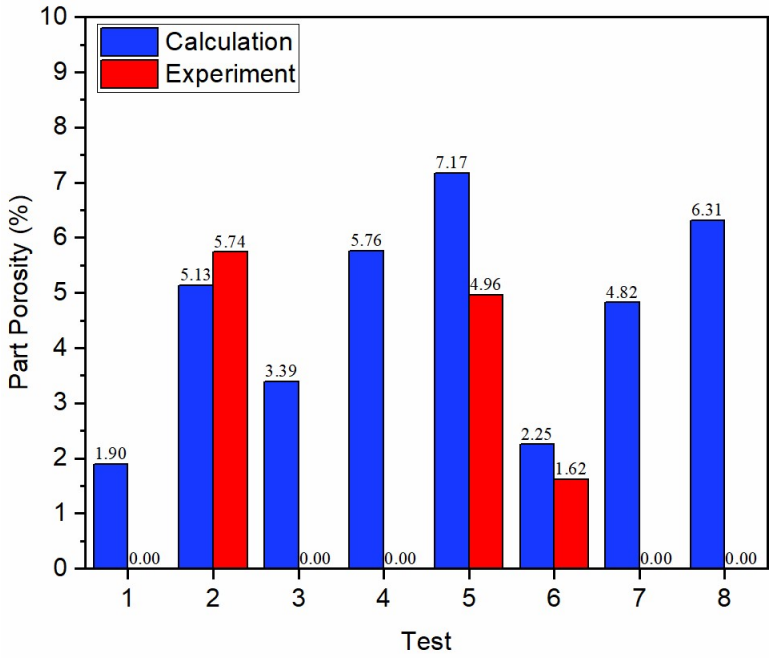

Figure 76 Experimental validation of the calculated part porosity. The blue color and red color denote calculated values and documented experimental values measured from the metallographic analysis [105].

Furthermore, sensitivity analyses of part porosity calculations were performed on the hatch space and layer thickness as shown in Figure 77. This trend confirms the reported

results in the references [107,108]. The nonlinear relationship was observed due to the overlapping of the semi-elliptical molten pool contour area.

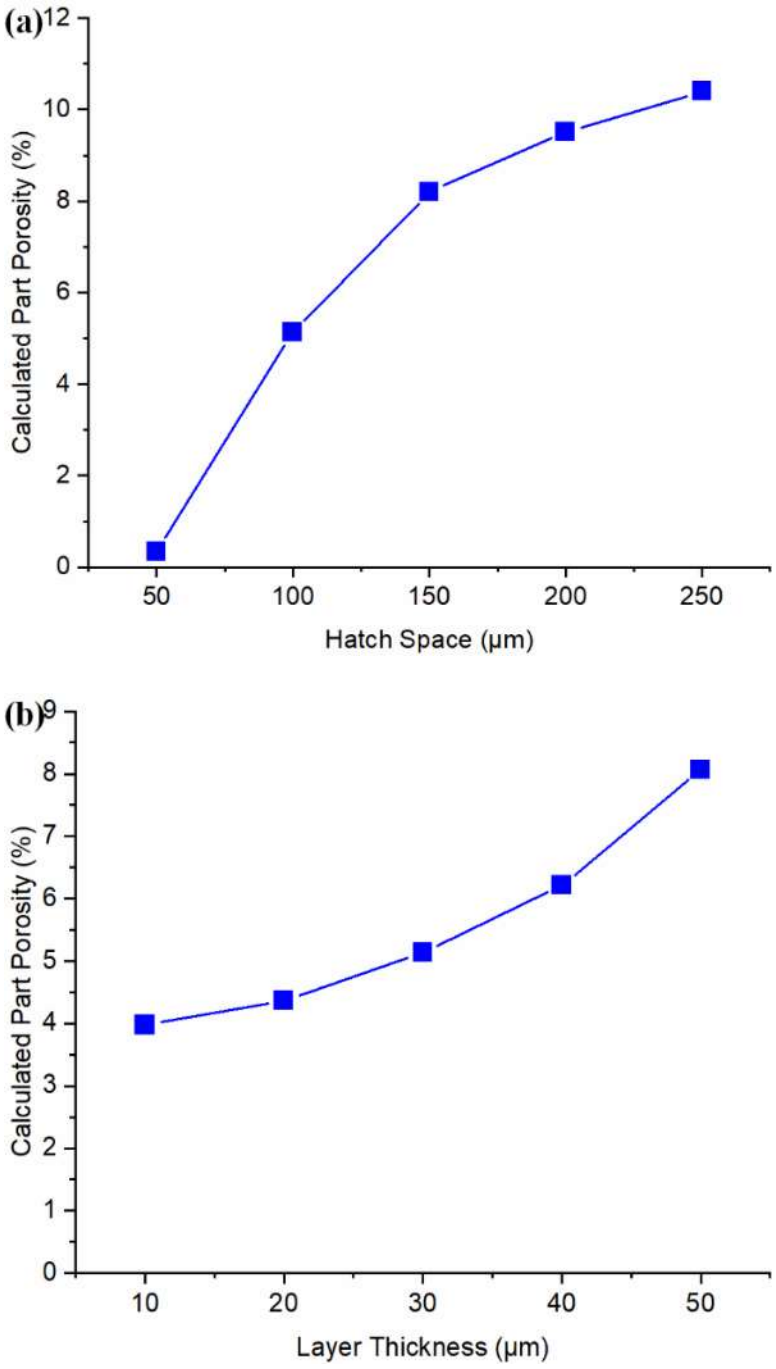

Figure 77 Sensitivity analyses of hatch space with t_L = 30 μm (a) and layer thickness with H = 100 μm (b) on the calculation of part porosity. Process parameters are P = 100 W, V = 750 mm/s [105].

4.3.2 Analytical Modeling of Part Porosity from Statistical Analysis

This section presented a physics-based model to predict the part porosity in PBMAM with given process parameters, materials properties, powder size distribution. The algorithm of the presented model is shown in Figure 78. The molten pool dimensions were first calculated by a closed-form temperature solution considering the laser heat input and part boundary heat loss. The porosity evolution was calculated by subtracting the volume fraction of the preprocessed powder bed void from the part porosity. The volume fractions of powder and void in packed powder bed were calculated by advancing front method and image analysis considering powder size variation and statistical distribution. The porosity model was developed based on the correlation between molten pool dimensions and porosity evolution using regression analysis.

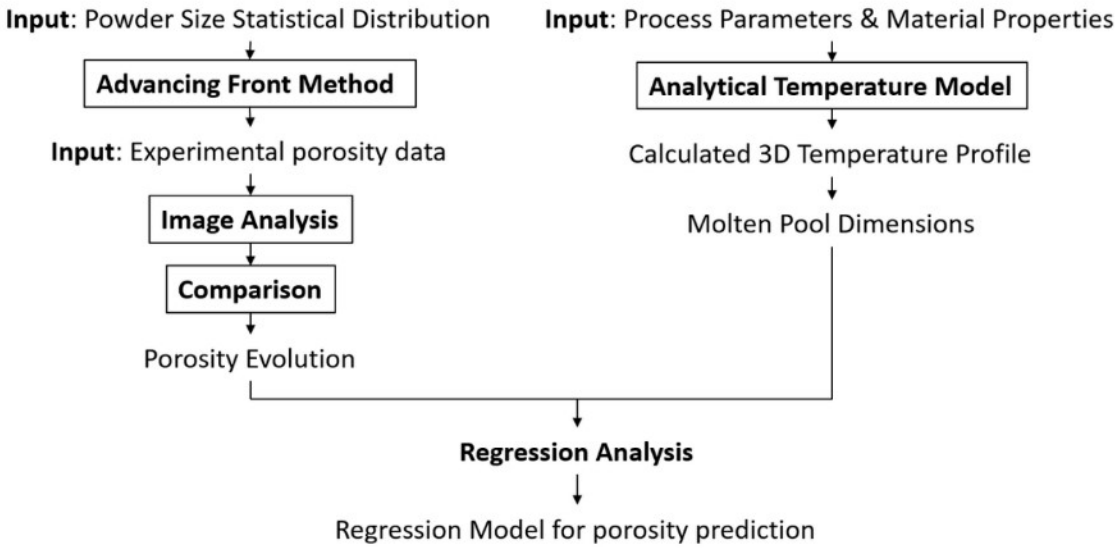

Figure 78 Algorithm of the analytical model in porosity prediction [106].

As shown in Figure 79, the morphology and size variation of the Ti6Al4V powders were analyzed using scanning electron microscopy (SEM). The powder size variation and

statistical distribution were obtained using ImageJ software based on the SEM image. The process parameters and experimental porosity values are given in Table 21.

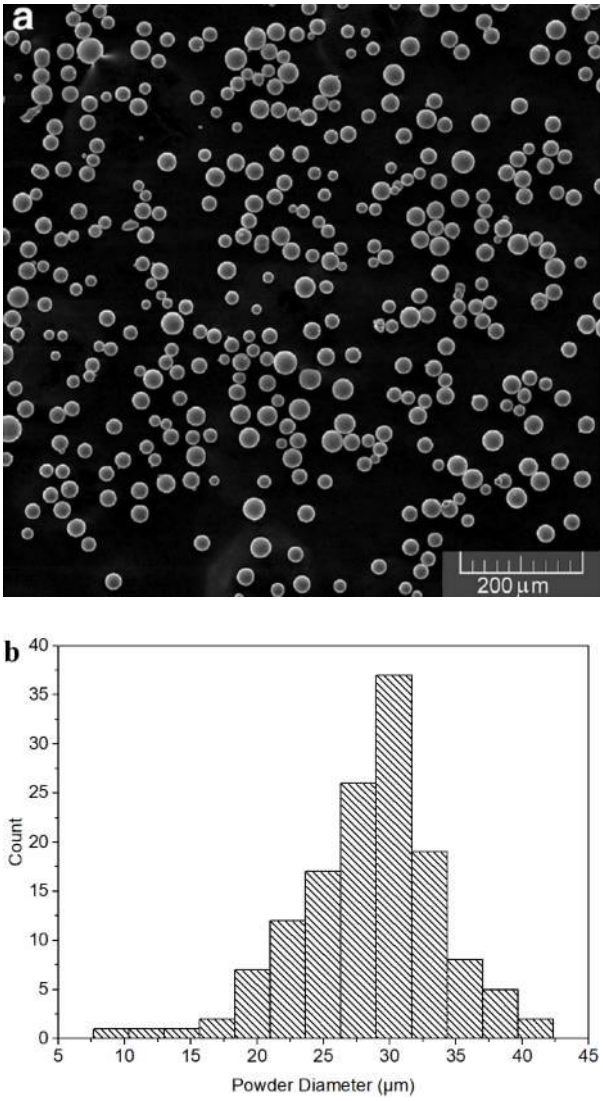

Figure 79 (a) Scanning electron microscopy (SEM) micrograph of Ti6Al4V powders. (b) Powder size variation of the Ti6Al4V powders [106].

Table 21 Experimental measurement of molten pool dimensions and part porosity [98].

Test	Power (W)	Velocity (mm/s)	Molten Pool Width (μm)	Molten Pool Depth (μm)	Porosity (%)	Porosity Evolution (%)
1	50	500	67.36	40.62	22.00	13.50
2	50	750	50.43	21.44	44.98	36.48
3	50	1000	47.42	19.51	54.99	46.49
4	50	1200	45.33	49.61	65.00	56.50
5	100	500	118.14	75.48	Fully dense	-8.50
6	100	750	98.20	48.84	5.74	-2.76
7	100	1000	75.25	36.32	19.81	11.31
8	100	1200	72.23	38.90	24.82	16.32
9	150	500	145.51	122.17	7.85	-0.65
10	150	750	135.54	89.83	Fully dense	-8.50
11	150	1000	116.29	74.82	Fully dense	-8.50
12	150	1200	108.17	66.92	4.96	-3.54
13	195	500	193.02	197.18	8.59	0.09
14	195	750	160.73	129.98	1.62	-6.88
15	195	1000	129.6	99.97	Fully dense	-8.50
16	195	1200	122.04	82.65	Fully dense	-8.50

The preprocessed powder bed packing pattern was calculated using the advancing front method as shown in Figure 80. The influence of the number of powders was investigated by using 500, 1000, 1500, and 2000 powders respectively. The powder packing pattern was calculated in duplicate at each powder number level as given in Table 22. The influence of the number of powders on the calculated volume fraction of the

powder bed void was insignificant. The average values were calculated and used in this study.

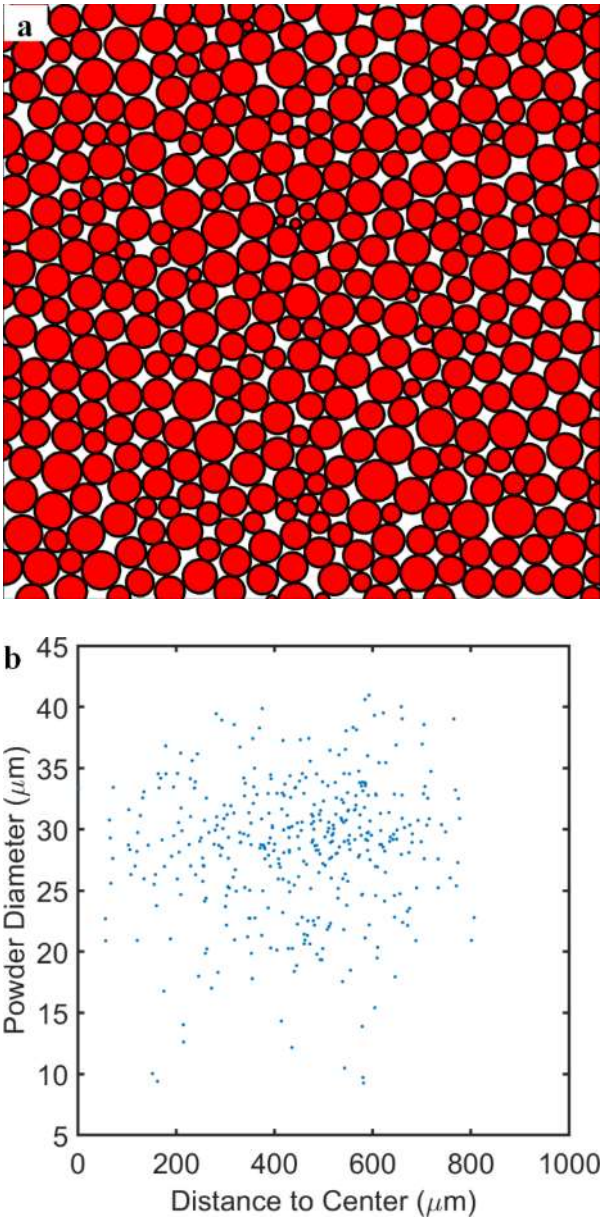

Figure 80 Calculated powder bed packing pattern of 500 particles. (b) calculated powder size and location [106].

Table 22 Powder volume fraction and void volume fraction of packed powder bed [106].

Number of Powders	Powder Volume Fraction (%)	Void Volume Fraction (%)
500	83.43	16.57
1000	84.62	15.38
1500	87.58	12.42
2000	86.46	13.54
2500	87.66	12.34
3000	86.78	13.22
Average	86.09	13.91

The regression model was developed by correlating the calculated molten pool dimensions and calculated porosity evolution under 12 different process conditions, specifically 1-3, 5-7, 9-11, 13-15 test conditions. The detailed outputs from the regression model are given in Table 23. The molten pool length has the lowest significant to the porosity prediction because the analyses of powder bed void and part porosity were performed based on the cross-sectional area, which was normal to the scanning direction, and the molten pool length direction. 4 different process conditions, specifically 4, 8, 12, 16 test conditions, were used to validate the porosity prediction. Close agreement was observed between prediction and experiment values as shown in Figure 81. The values reported in the table were calculated porosity evolution values. The deviation between experimental porosity and calculated porosity might be caused by the accuracy of temperature prediction and powder bed packing calculation, the small number of calibration data, and the missing physics such as the influence of deposition quality of

previous layer, and the influence of heat-affected zone of previous layer, which should be investigated as future works to further improve the prediction accuracy.

Table 23 Regression analysis based on 12 different test conditions [106].

Regression Statistics		Output Parameters				
Multiple R	0.930	Variables	Coefficients	Standard Error	t Stat	P-value
R Square	0.865	Intercept	71.265	10.991	6.484	0.000
Adjusted R Square	0.815	L	-0.022	0.067	-0.336	0.745
Standard Error	8.011	W	-1.102	0.266	-4.139	0.003
Observations	12	D	0.714	0.177	4.039	0.004

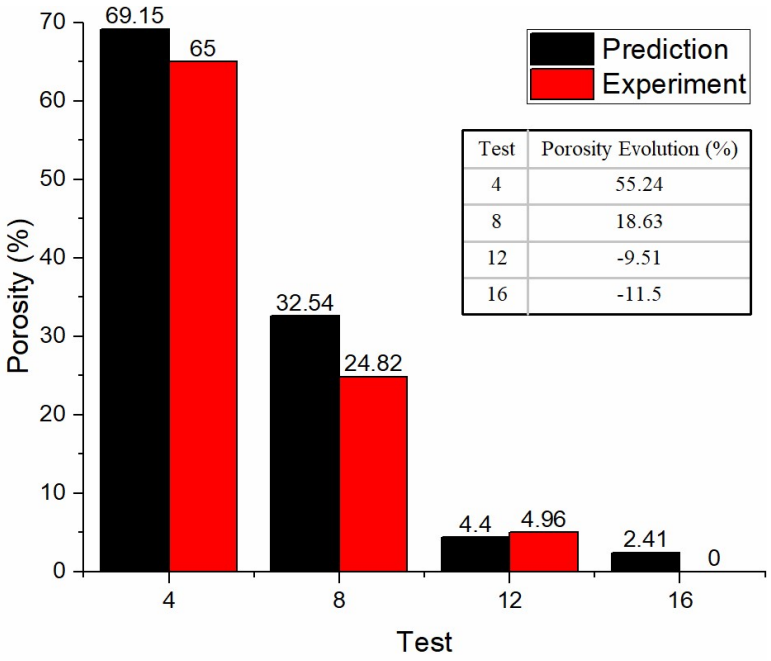

Figure 81 Experimental validation on the calculated part porosity under 4 different process conditions [106].

4.4 Analytical Modeling of In-situ Deformation in Powder Feed Additive Manufacturing

The section presented an analytical model to predict the in-situ thermal deformation of the build and substrate in PFMAM. The repeatedly rapid heat and solidification during the process caused non-uniform temperature distribution, which led to the deformation of the build and substrate such as geometrical deviation and delamination as illustrated in Figure 82, where the blue object represents a laser displacement sensor (LDS) placed underneath the substrate, the red arrows represent laser scans. the black arrow represents the deflection at the right end from its original shape. The moving point heat source solution was employed and modified to predict temperature distribution with the assumption of uniform temperature at the same in-depth locations. The die-substrate assembly model was employed to predict the deformation of the build and substrate, in which the build was mathematically discretized into two sections, as shown in Figure 83, where the red arrow denotes laser scan direction. The following assumptions were enforced in the presented model. 1) plane strain condition and steady-state; 2) temperature-sensitive material properties; 3) isotropic and homogeneous material for each section.

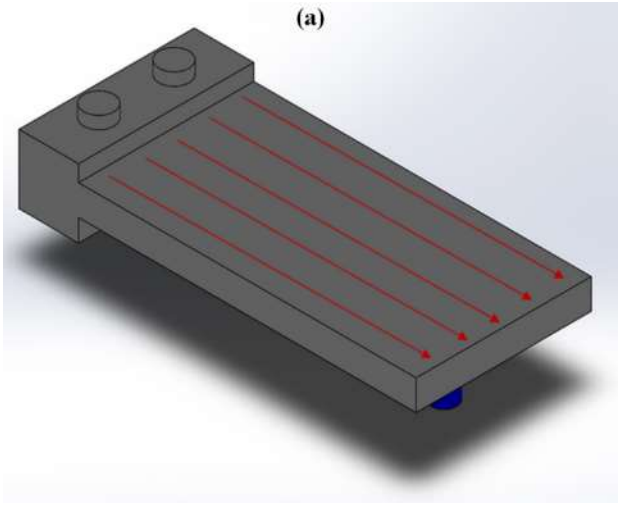

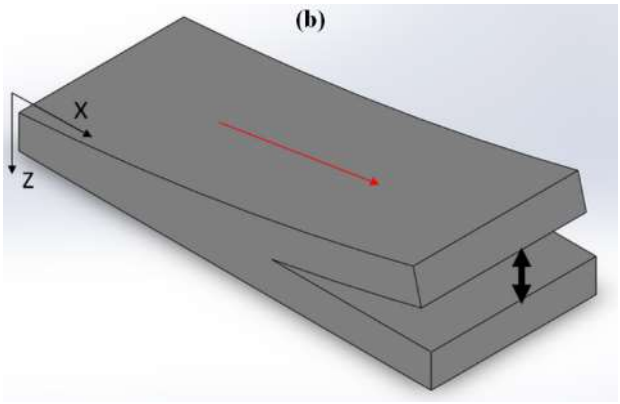

Figure 82 Schematic drawing of (a) experimental setup in powder feed metal additive manufacturing and (b) deformation of the build and substrate with a fixed left end [109].

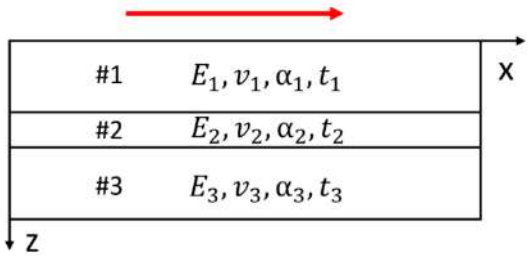

Figure 83 Schematic view of the die-substrate assembly [109].

The die-substrate model was developed based on the difference in thermal stress, which can be expressed as the following [110,111].

$$w(x) = \frac{t\Delta\alpha\Delta T}{2\lambda D}\left(\frac{1}{2}x^2 - \frac{coshkx - 1}{k^2 coshkl}\right) \tag{24}$$

$$\Delta T = T_f - T_i \tag{25}$$

$$\Delta\alpha = \alpha_1 - \alpha_3 \tag{26}$$

$$k = \sqrt{\frac{\lambda}{\kappa}} \tag{27}$$

$$\lambda = \frac{1 - v_1}{E_1 t_1} + \frac{1 - v_3}{E_3 t_3} + \frac{t^2}{4D} \tag{28}$$

$$\kappa = \frac{t_1}{3G_1} + \frac{2t_2}{3G_2} + \frac{t_3}{3G_3} \tag{29}$$

$$G_i = \frac{E_i}{2(1 + v_i)}, i = 1,2,3 \tag{30}$$

$$t = t_1 + t_2 + t_3 \tag{31}$$

$$D = D_1 + D_2 + D_3 \tag{32}$$

where $\mathrm{E}, \mathrm{G}, \mathrm{v}, \alpha, \mathrm{t}$ represent temperature-sensitive elastic modulus, shear modulus, Poisson's ratio, thermal expansion coefficient, and layer thickness respectively. $w(x)$ is the deflection along scan direction.

The presented model was investigated in PFMAM of Inconel 625. The temperature-dependent materials properties are given in Table 24. The room temperature, material melting temperature, and density are T_0= 20 ℃, T_m=1350 ℃, ρ=8440 kg/m^3, respectively. The process conditions and experimental deformation measurements are given in Table 25. Deflections were experimentally measured using a laser displacement sensor at x = 114.4 mm location.

Table 24 Temperature-sensitive material properties of Inconel 625 Alloy [112].

Temperature T [°C]	Thermal conductivity k [W/ (m· °C)]	Specific heat c [J/ (kg· °C)]	Elastic modulus E [GPa]	Thermal expansion coefficient α [μm/ (m· °C)]	Poisson's ratio v
21	9.8	410	208	12.8	0.278
93	10.8	427	204	12.8	0.28
204	12.5	456	198	13.1	0.286
316	14.1	481	192	13.3	0.29
427	15.7	511	186	13.7	0.295
538	17.5	536	179	14	0.305
649	19	565	170	14.8	0.321
760	20.8	590	161	15.3	0.34
871	22.8	620	148	15.8	0.336

Table 25 Process conditions and of powder feed metal additive manufacturing with unidirectional scan strategy.

Case number	1	2	3	4	5	6
Laser power P (kW)	1	1	1	1	2.5	2.5
Laser velocity V (m/s)	10.6	10.6	4.2	4.2	10.6	10.6
Track length L (mm)	132	132	135	135	127	127
Layer thickness t_L(mm)	0.5	0.5	1.2	1.2	1.1	1.1
Number of layers N	1	2	1	2	1	2
Absorption η (%)	38	38	41	41	62	62
Deflection w_{exp} (mm)	1.01	1.74	1.34	2.61	1.76	3.17

The calculated in-depth (z-direction) temperature distribution in build and substrate under process conditions in case 1 and case 2 were shown in Figure 84 (a) and (c)

respectively. The predicted deflection of build and substrate in case 1 and case 2 were shown in Figure 84 (b) and (d), respectively. The x-axis starts from 20mm to avoid the portion that is clamped. Similar temperature trends and similar deflection trends were observed for all other cases.

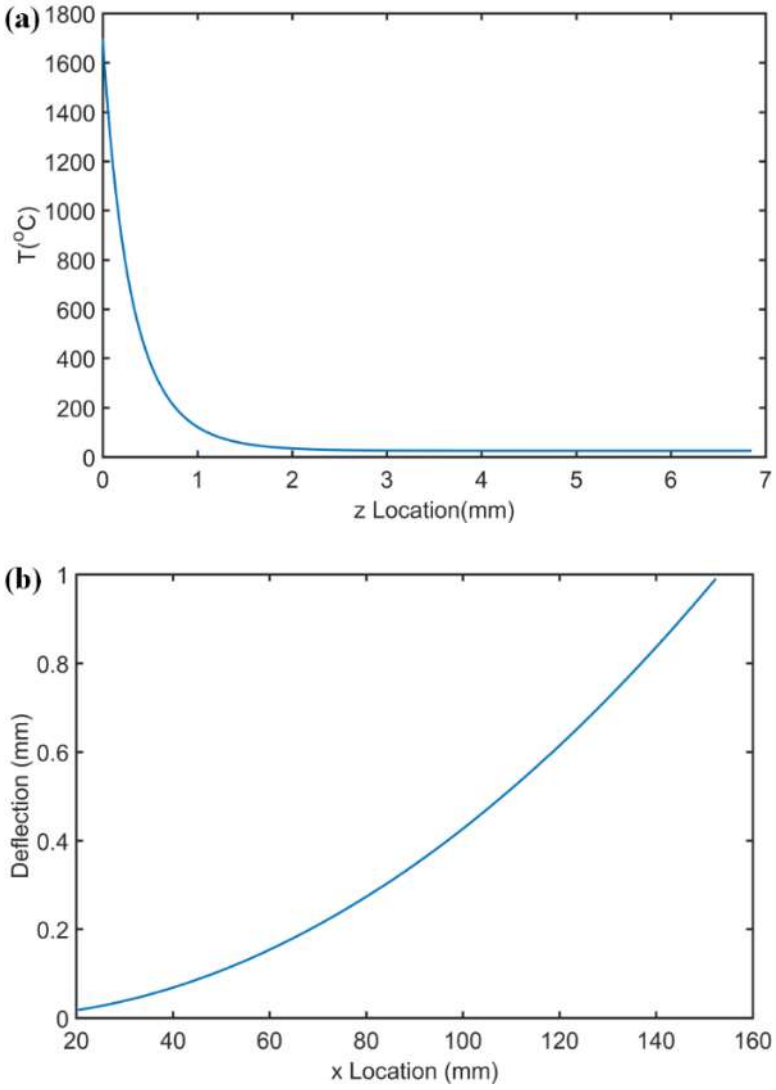

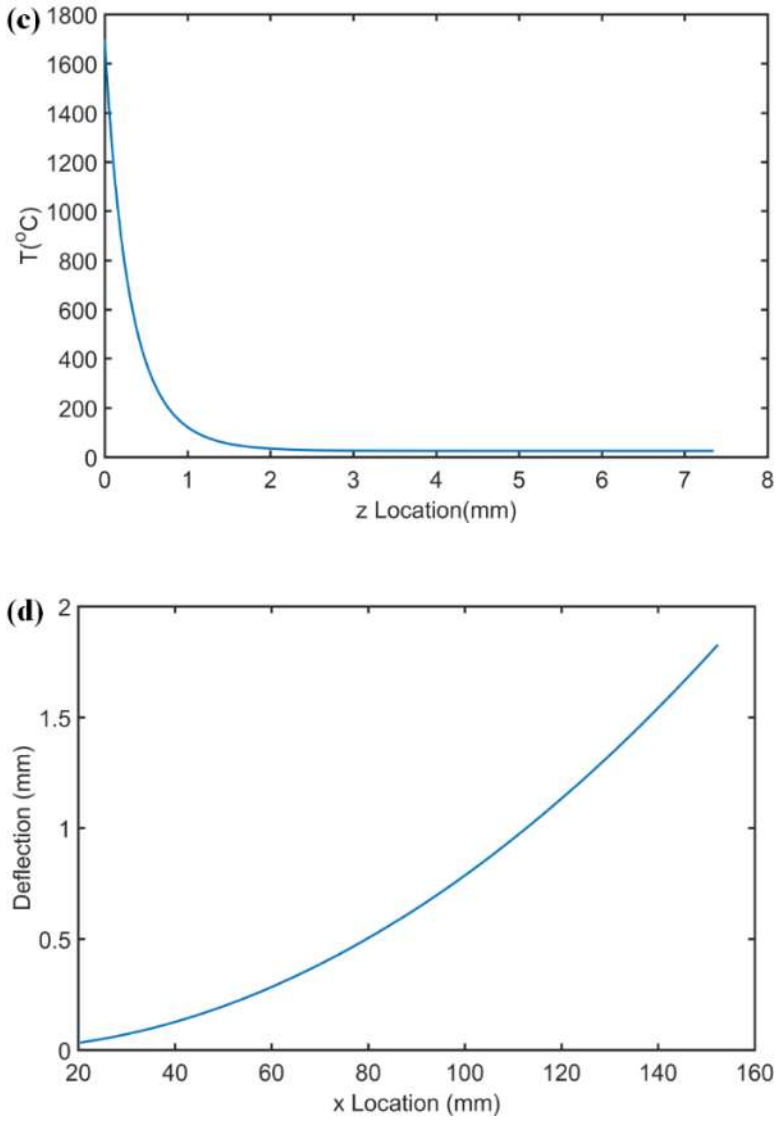

Figure 84 Calculated in-depth temperature distribution along z-direction for (a) case 1 and (b) case 2; Calculated deflection along the x-direction of the build and substrate for (c) case 1 and (d) case 2 [109].

The calculated deflections at x = 114.4 mm location were validated against experimental measurements, in which the deflections were measured using LDS at the fixed location of the substrate. Good agreements were observed between predictions and experimental measurements, as shown in Figure 85. The calculated deflections were smaller than the experimental values because of the neglection of the heat-affected zone in

previous scan and the assumption of uniform temperatures at the same in-depth location. The underestimated temperature distribution yielded an underestimated deflection.

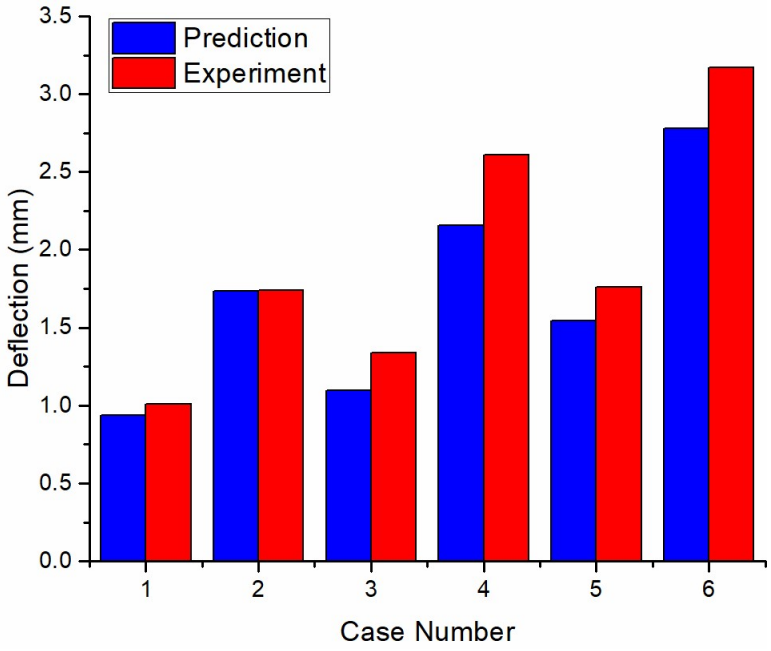

Figure 85 Calculated deflections and experimental deflections of build and substrate at x = 114.4 mm under various process conditions [109].

4.5 Analytical Modeling of Part Distortion in Powder Bed Additive Manufacturing

This section presented an analytical modeling methodology for the prediction of part distortion in PBMAM. The algorithm of the presented model is shown in Figure 86. The presented model consists of analytical thermal modeling, thermal stress modeling, residual stress modeling, and distortion modeling. It has promising short computational efficiency without resorting to finite element analysis or any iteration-based simulations. The temperature profile is calculated using a moving point heat source solution and heat sink solution with consideration of heat input from a moving laser and heat loss from boundary heat transfer. The thermal stress is calculated from the temperature calculation using a

thermal stress model considering thermal load, surface tension, and hydrostatic pressure. The residual stress is calculated from the thermal stress calculation using an elastic-plastic relaxation procedure. The residual stress-induced part distortion is finally calculated from the calculated residual stress and residual strain using a displacement model.

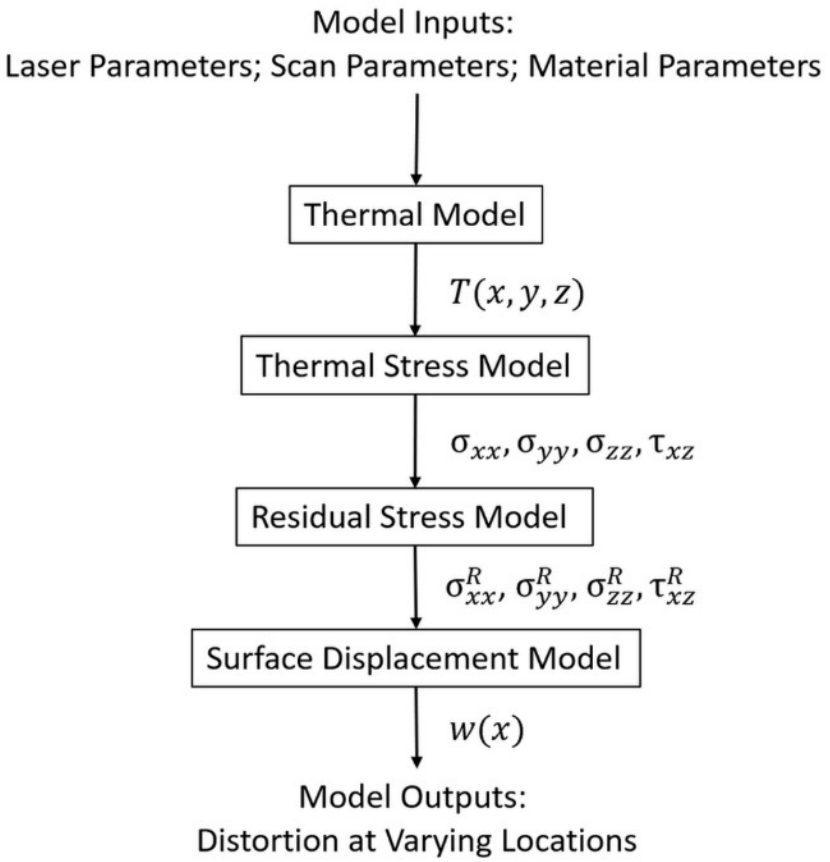

Figure 86 Algorithm in analytical modeling of part distortion in metal additive manufacturing [114].

The presented model was validated with distortion prediction of a twin-cantilever part produced by PBMAM with Ti6Al4V powders. The part geometry with saw tooth support structure is illustrated in Figure 87, where PL, PW, PH denote part length, part width, and part height respectively, red arrows denote unidirectional scan strategy. The

process parameters and part dimensions are given in Table 26. The saw tooth structure was designed with dimensions of 1 mm in thickness (x-direction), 5 mm in height (z-direction), and 10 mm in width (y-direction). The space between two adjacent teeth was 1 mm. The twin-cantilever part was printed by GPI Prototype (Lake Bluff, IL) with the EOS machine.

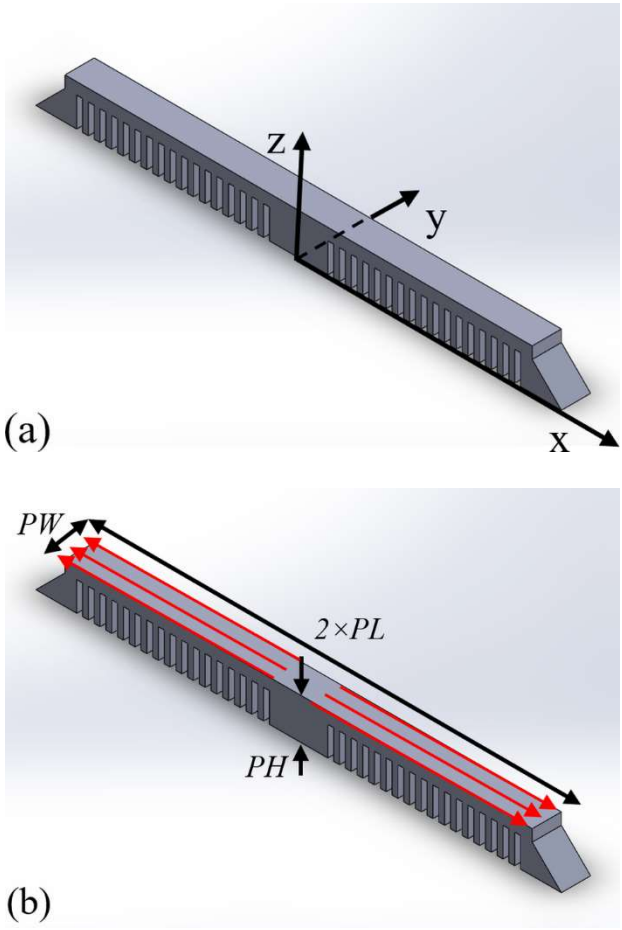

Figure 87 (a) Schematic drawing of the twin-cantilever part with the saw-tooth support structure. x, y, z denotes the Cartesian coordinate. (b) Part dimension and scan strategy [114].

Table 26 Process parameters in powder bed metal additive manufacturing of Ti6Al4V and part dimensions.

Parameter	Symbol	Value	Unit
Powder	P	200	W
Scan Velocity	V	1000	mm/s
Hatch Space	H	0.14	mm
Scan Strategy	Unidirectional Strip		
Part Length	PL	40	mm
Part Width	PW	10	mm
Part Height	PH	2	mm

As shown in Figure 88, the temperature distribution was calculated on the three-dimensional par for the implementation of heat sink solution for boundary heat transfer but the stresses were calculated on the cross-sectional area with the assumption of plane strain condition, which neglected the distortion in the transverse direction. The red arrow and green arrows denote the heat input from moving laser heat source, and boundary heat loss due to convection and radiation respectively. L, W, D are molten pool length, width, and depth respectively. σ_x, σ_z, τ_{xz}, τ_{zx} are normal stresses and shear stresses respectively.

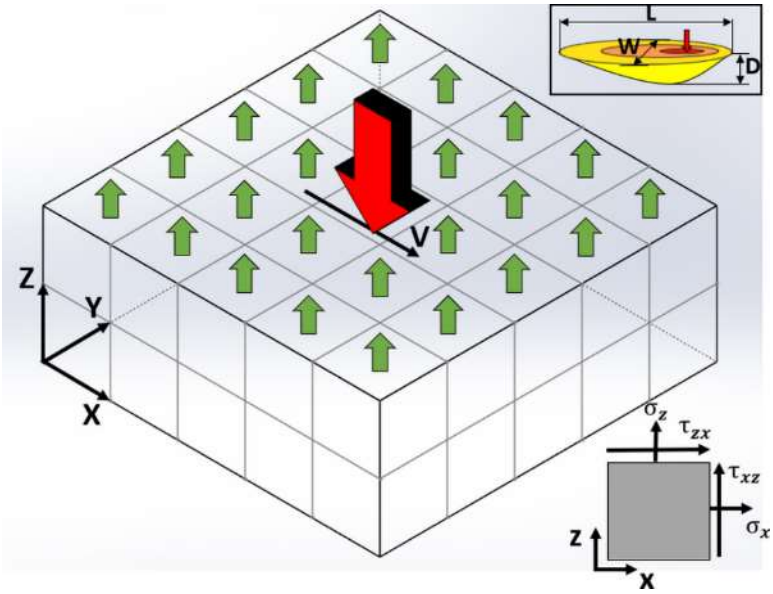

Figure 88 Heat transfer mechanism in laser-assisted metal additive manufacturing [114].

The thermal stress can be calculated from the thermoelasticity theory as the following.

$$\sigma_{xx}^{therm}(x,z) = -\frac{\alpha E}{1-2v}\int_0^{\infty}\int_{-\infty}^{\infty}\left(G_{xh}\frac{\partial T}{\partial x}(x',z') + G_{xv}\frac{\partial T}{\partial z}(x',z')\right)dx'dz' + \frac{2z}{\pi}\int_{-\infty}^{\infty}\frac{p(t)(t-x)^2}{((t-x)^2+z^2)^2}dt - \frac{\alpha E T(x,z)}{1-2v} \quad (33)$$

$$\sigma_{zz}^{therm}(x,z) = -\frac{\alpha E}{1-2v}\int_0^{\infty}\int_{-\infty}^{\infty}\left(G_{zh}\frac{\partial T}{\partial x}(x',z') + G_{zv}\frac{\partial T}{\partial z}(x',z')\right)dx'dz' + \frac{2z^3}{\pi}\int_{-\infty}^{\infty}\frac{p(t)}{((t-x)^2+z^2)^2}dt - \frac{\alpha E T(x,z)}{1-2v} \quad (34)$$

$$\sigma_{xz}^{therm}(x,z)$$

$$= -\frac{\alpha E}{1-2v}\int_0^\infty \int_{-\infty}^\infty \left(G_{xzh}\frac{\partial T}{\partial x}(x',z') + G_{xzv}\frac{\partial T}{\partial z}(x',z') \right) dx'dz' \tag{35}$$

$$+\frac{2z^2}{\pi}\int_{-\infty}^\infty \frac{p(t)(t-x)}{((t-x)^2+z^2)^2}dt$$

$$\sigma_{yy}^{therm}(x,z) = v(\sigma_{xx}^{therm} + \sigma_{zz}^{therm}) - \alpha E T(x,z) \tag{36}$$

$$p(t) = \frac{\alpha E T(x, z=0)}{1-2v} \tag{37}$$

where the thermal stress σ_{xx}^{therm}, σ_{yy}^{therm}, σ_{zz}^{therm}, σ_{xz}^{therm} are calculated with Green's functions under plane-strain conditions. The Green's functions (G_{xh}, G_{zh}, G_{xzh}, G_{xv}, G_{zv}, G_{xzv}) are derived in the reference [113] and provides an analytical solution for the calculation of thermal stress. α, E, v are thermal expansion coefficient, elastic modulus, and Poisson's ratio, respectively.

The residual stress can be calculated from the elastoplastic relaxation procedure with plane strain assumption as the following [115].

$$\dot{\varepsilon}_{xx} = \Psi \dot{\varepsilon}_{xx}^{\ *} \tag{38}$$

$$\psi = 1 - \exp\left(-\kappa \frac{3h}{2G}\right) \tag{39}$$

$$\dot{\varepsilon}_{yy} = 0 \tag{40}$$

where $\dot{\varepsilon}_{xx}, \dot{\varepsilon}_{yy}$ are elastic solutions, $\dot{\varepsilon}_{xx}{}^{*}$ is the elastoplastic solution, Ψ is the hybrid function with κ, h, G denoted model constant, plastic modulus, and shear modulus.

The above equation can be expanded as the following.

$$\begin{aligned}\dot{\varepsilon}_{xx} &= \frac{1}{E}\left[\dot{\sigma}_{xx} - v\left(\dot{\sigma}_{yy} + \dot{\sigma}^{*}_{zz}\right)\right] + \frac{1}{h}\left(\dot{\sigma}_{xx}n_{xx} + \dot{\sigma}_{yy}n_{yy} + \dot{\sigma}^{*}_{zz}n_{zz} + 2\tau^{*}_{xz}n_{xz}\right)n_{xx} \\ &= \psi\left(\frac{1}{E}\left[\dot{\sigma}^{*}_{xx} - v\left(\dot{\sigma}_{yy} + \dot{\sigma}^{*}_{zz}\right)\right] + \frac{1}{h}\left(\dot{\sigma}^{*}_{xx}n_{xx} + \dot{\sigma}_{yy}n_{yy} + \dot{\sigma}^{*}_{zz}n_{zz} + 2\tau^{*}_{xz}n_{xz}\right)n_{xx}\right)\end{aligned} \tag{41}$$

$$\dot{\varepsilon}_{yy} = \frac{1}{E}\left[\dot{\sigma}_{yy} - v(\dot{\sigma}_{xx} + \dot{\sigma}^{*}_{zz})\right] + \frac{1}{h}\left(\dot{\sigma}_{xx}n_{xx} + \dot{\sigma}_{yy}n_{yy} + \dot{\sigma}^{*}_{zz}n_{zz} + 2\tau^{*}_{xz}n_{xz}\right)n_{yy} = 0 \tag{42}$$

The relaxation procedure is used to calculate the residual stress as the non-zero components.

$$\Delta\sigma_{zz} = -\frac{\sigma^{R}_{zz}}{M}, \Delta\tau_{xz} = -\frac{\tau^{R}_{xz}}{M}, \Delta\varepsilon_{xx} = -\frac{\varepsilon^{R}_{xx}}{M} \tag{43}$$

The part thickness was assumed to be infinitesimal, and thus the part distortion can be calculated by the surface displacement model, in displacement of the discretized elements was integrated [116]. The surface displacement model can be expressed as the following.

$$w = 2\mu\sum_{n=1}^{N}\int_{\boldsymbol{\Omega}}\varepsilon^{R}_{ij,n}(M)\varepsilon^{R}_{ij,n}(A)d\boldsymbol{\Omega} = \sum_{\boldsymbol{n=1}}^{\boldsymbol{N}}\varepsilon^{R}_{ij,n}(M)K_{ij} \tag{44}$$

$$K_{ij} = \begin{Bmatrix} D_{ij}(a_1 + \Delta x_1, a_2 + \Delta x_2, a_3 + x_3,) - \\ D_{ij}(a_1 + \Delta x_1, a_2 + \Delta x_2, a_3 - \Delta x_3,) - \\ D_{ij}(a_1 + \Delta x_1, a_2 - \Delta x_2, a_3 + \Delta x_3,) + \\ D_{ij}(a_1 + \Delta x_1, a_2 - \Delta x_2, a_3 - \Delta x_3,) - \\ D_{ij}(a_1 - \Delta x_1, a_2 + \Delta x_2, a_3 + \Delta x_3,) + \\ D_{ij}(a_1 - \Delta x_1, a_2 + \Delta x_2, a_3 - \Delta x_3,) + \\ D_{ij}(a_1 - \Delta x_1, a_2 - \Delta x_2, a_3 + \Delta x_3,) - \\ D_{ij}(a_1 - \Delta x_1, a_2 - \Delta x_2, a_3 - \Delta x_3,) \end{Bmatrix} \tag{45}$$

$$D = \frac{1}{\pi}\begin{bmatrix} \left(-vxln(y+R) - (1-2v)ztan^{-1}\left(\frac{y+z+R}{x}\right)\right) \\ \left(-vyln(x+R) - (1-2v)ztan^{-1}\left(\frac{y+z+R}{y}\right)\right) \\ 2(1-v)\left(2ztan^{-1}\left(\frac{y+z+R}{z}\right) + xln(y+R) + yln(x+R) - \frac{z}{2}\theta\right) \\ (-2vR - (1-2v)zlnz(z+R)) \\ \left(2xtan^{-1}\left(\frac{y+z+R}{x}\right) + yln(z+R)\right) \\ \left(2ytan^{-1}\left(\frac{y+z+R}{y}\right) + xln(z+R)\right) \end{bmatrix} \tag{46}$$

$$\theta = -2tan^{-1}\left(\frac{xy}{zR}\right) \tag{47}$$

$$R = \sqrt{x^2 + y^2 + z^2} \tag{48}$$

where the $\varepsilon_{ij,n}^{R}$ is the residual strain at each discretized element, K_{ij} is the corresponding operation function.

The part distortion was assumed to be continuous and finally calculated as illustrated in Figure 89, where the part is mathematically discretized into many sections and the distortion is calculated for each section. The bold solid lines and the bold dashed line denotes the original part and distorted part.

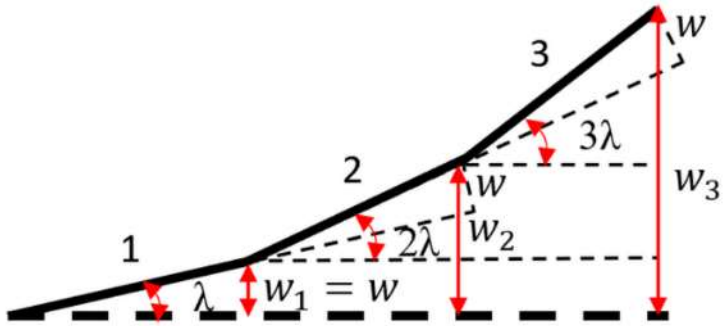

Figure 89 Schematic drawing of the part distortion calculation along the part length direction [114].

Experimental setup for the part distortion measurement is shown in Figure 90, where the part was mounted onto a fixture, a coordinate measurement machine (CMM) was employed to measure the part distortion on the top surface of the part. The CMM had dimensional accuracy of 1 μm. The distortion measurements were performed by a 3 mm stylus with 200 mN probing forces at 3 mm/s along x-direction with a spacing of 0.5 mm between two adjacent points. The distortion measurements were conducted at the center (y = 2.5 mm) and near two edges (y = 0.05 mm and y = 4.95 mm) of the part.

The distortion measurements were illustrated in Figure 91. Highly symmetric profiles were observed along part length direction (x-direction). The distortion in part transverse direction (y-direction) was negligible. The fluctuations in the measurement were caused by the rough surface finish. They were more observable near the center due to the low distortion value and worse surface finish (roughness to distortion ratio).

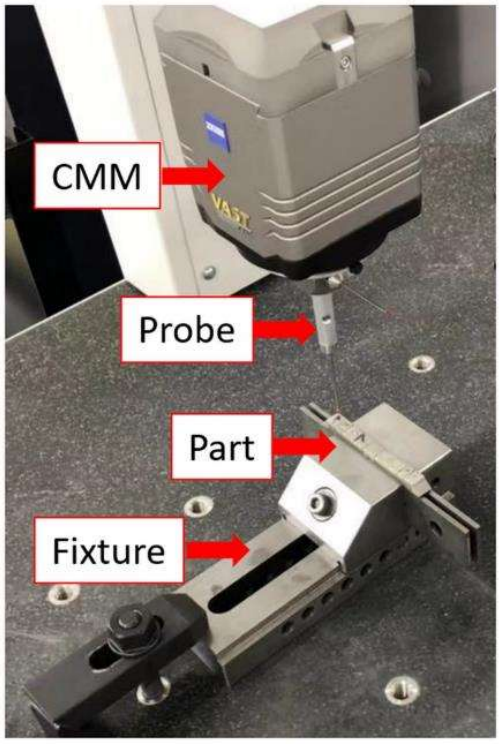

Figure 90 Experimental setup for distortion measurement using coordinate measurement machine [114].

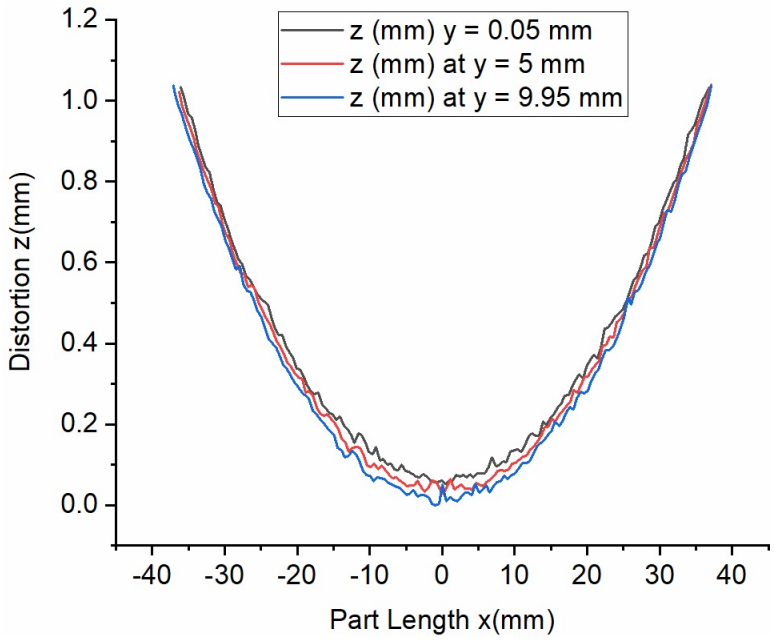

Figure 91 Part distortion measured along part length (x-direction) by coordinate measurement machine at y = 0.05 mm, y = 2.5 mm, y =4.95 mm [114].

The residual stress was calculated at the laser heat source location in the scan direction and transverse direction as shown in Figure 92, where the tensile residuals stress was observed at the near-surface location, followed by compressive residual stress was observed at a deeper location and then decreasing trend to zero. The part distortion values were calculated along the part length direction (x-direction) by mathematically discretize the part into many sections. The number of sections was determined with experience calibration by trial and error. Close agreements were observed upon validation to experimental measurement along x-directions at y = 2.5 mm as shown in Figure 93.

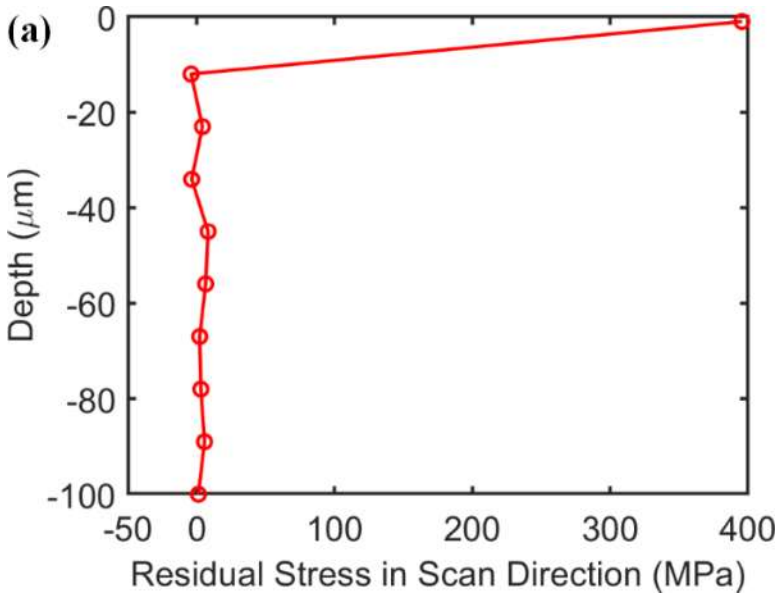

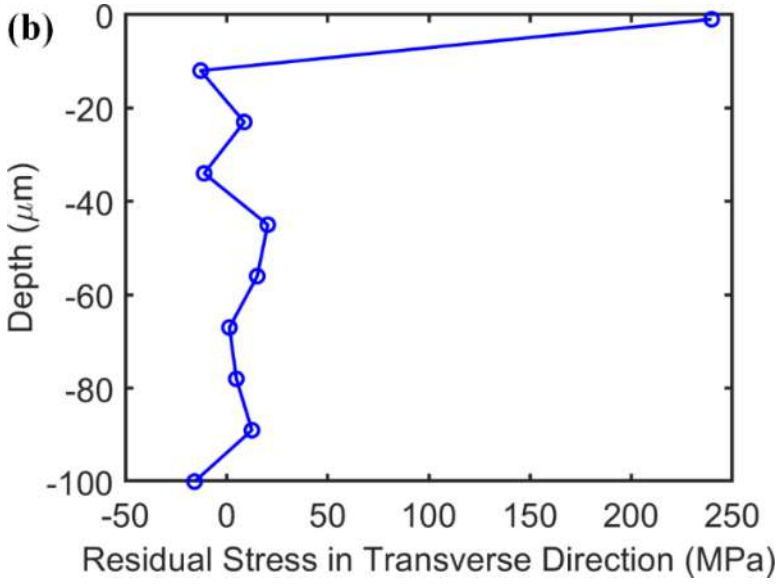

Figure 92 Calculated residual stresses in scan direction (x-direction) and transverse direction (z-direction). The depth value at 0 denotes the part top surface [114].

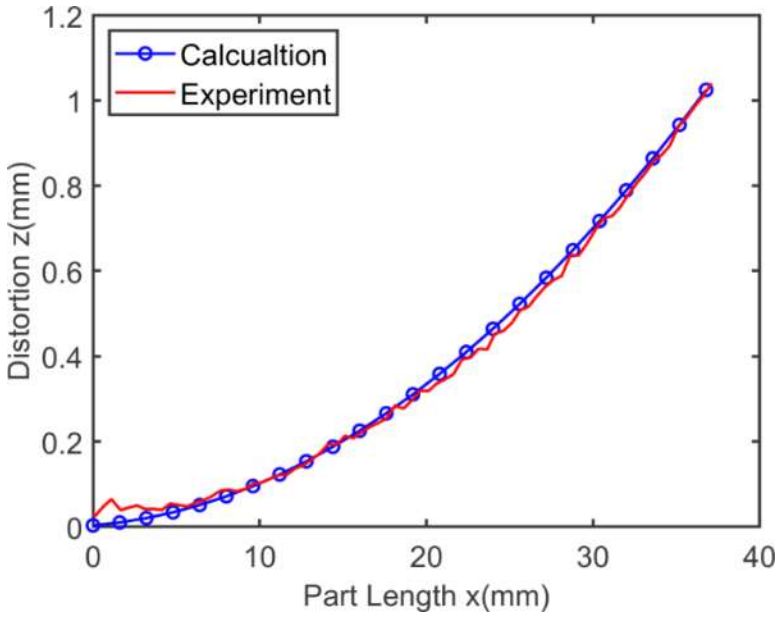

Figure 93 Calculated part distortion along the part length (x-direction) at y = 2.5 mm [114].

CHAPTER 5. CONCLUSION AND FUTURE WORKS

This work studied the subtractive and additive manufacturing processes through the analytical modeling approach and experimental investigation. The existing models and reported experimental techniques were studied through literature review. Analytical models were developed based on materials constitutive behaviors and process mechanics in precision machining and metal additive manufacturing.

In the modeling of precision machining, analytical models were developed to predict the machining temperatures and machining forces. An inverse modeling approach was developed based on the modeling of machining force and a gradient search method for the identification of material constitutive model constants, namely J-C model constants. The modified chip formation model was employed with a Kalman filter algorithm to inversely identify the J-C model constant when the difference between calculated machining forces and experimental forces was minimal. Analytical models were developed to predict the machining temperature through materials flow stress modeling using the J-C model and mechanics model. The machining temperatures were estimated by minimizing the calculated materials flow stress using the J-C model and mechanics model. The first temperature model used cutting force and chip thickness as inputs. This model was developed based on the constant material flow rate at the chip formation zone. The second temperature models used cutting force and thrust force as inputs. This model was developed based on the geometrical relationship between machining forces at the chip formation zone. The developed temperature models were evaluated with a quantitative and qualitative comparison to existing models, namely chip formation model, and heat source

model. Furthermore, UFG Ti was studied with the developed models because of its increasing usefulness in biomedical applications. UFG Ti has excellent mechanical strength and biocompatibility with human cells and tissues. The J-C model constants were inversely identified from the inverse analysis. The identified J-C model constants were employed in the calculations of machining forces and machining temperatures.

In the modeling of metal additive manufacturing, analytical models were developed to predict the temperature profile, thermal stress, residual stress, part porosity, in-situ thermal deformation and part distortion in PBMAM and PFMAM. The existing thermal model was further developed with considerations of scanning strategy, heat transfer boundary condition, statistical powder size distribution, and powder packing-related material properties. The developed models allow the temperature prediction of the dimensional part, which significantly improved the usefulness of analytical thermal models in real applications. With the predictive capability of temperature profile, the part porosity due to lack-of-fusion was calculated from thermal analysis on the part cross-sectional area. The porosity evolution and materials thermal behavior was correlated through regression analysis for the prediction of part porosity. The in-situ deformation was calculated using a die-substrate assembly model based on the difference of thermal stress in the part and substrate. The thermal stress, residual stress, and part distortion were calculated based on thermoelastic theory, an elastoplastic relaxation procedure, and surface displacement calculation.

The calculations were validated with the experimental measurement of various materials. Machining forces were measured using a piezoelectric dynamometer. Machining temperatures were investigated using infrared (IR) thermal camera, and tool-chip interface

thermocouple at the chip formation zone. Temperature profiles in metal additive manufacturing were investigated by the in-situ methods with thermocouple and IR thermal camera, and post-process method with the observation of solidified microstructure of molten pool. The part porosity and part distortion were investigated from the metallographic analysis on the part cross-sectional area and coordinate measurement machine (CMM), respectively. Good agreements were observed upon experimental validations under different process conditions.

The analytical models were developed without resorting to FEA or any iterative calculation-based simulations. Multiple factors were considered in the developed model with improving understanding. Therefore, the developed models have a significant computational advantage with high prediction accuracy. The high computational efficiency and high prediction accuracy allow the process-parameters planning and process optimization through inverse analysis. The developed analytical models have significantly improved the usefulness of analytical modeling in the subtractive and additive manufacturing and thus would facilitate the use of analytical models in real applications, and exploration of new manufacturing processes for new materials. In the future, the presented models in the current study can be further developed to eliminate the need for model assumptions, and the need for experimental calibrations. The developed models in precision machining could be applied to the machining with geometrically complex tool, and the machining processes under various cooling conditions with minimum quality lubrication (MQL), cryogenic coolant, green coolant, etc. The developed models in metal additive manufacturing could be applied to geometrical complex parts.

REFERENCES

1. Nee, A. Y. C. (2015). Handbook of manufacturing engineering and technology. Springer.

2. Thomas, D. S., & Gilbert, S. W. (2014). Costs and cost effectiveness of additive manufacturing. NIST Special Publication, 1176, 12

3. Laureijs, R. E., Roca, J. B., Narra, S. P., Montgomery, C., Beuth, J. L., & Fuchs, E. R. (2017). Metal additive manufacturing: cost competitive beyond low volumes. Journal of Manufacturing Science and Engineering, 139(8), 081010.

4. Zerilli, F. J., & Armstrong, R. W. (1987). Dislocation-mechanics-based constitutive relations for material dynamics calculations. Journal of applied physics, 61(5), 1816-1825.

5. Johnson, G. R., & Cook, W. H. (1985). Fracture characteristics of three metals subjected to various strains, strain rates, temperatures and pressures. Engineering fracture mechanics, 21(1), 31-48.

6. Kolsky, H. (1949). An investigation of the mechanical properties of materials at very high rates of loading. Proceedings of the physical society. Section B, 62(11), 676.

7. Jaspers, S. P. F. C., & Dautzenberg, J. H. (2002). Material behaviour in conditions similar to metal cutting: flow stress in the primary shear zone. Journal of Materials Processing Technology, 122(2-3), 322-330.

8. Khan, A. S., Suh, Y. S., & Kazmi, R. (2004). Quasi-static and dynamic loading responses and constitutive modeling of titanium alloys. International Journal of Plasticity, 20(12), 2233-2248.

9. Milani, A. S., Dabboussi, W., Nemes, J. A., & Abeyaratne, R. C. (2009). An improved multi-objective identification of Johnson–Cook material parameters. International Journal of Impact Engineering, 36(2), 294-302.

10. Majzoobi, G. H., Freshteh-Saniee, F., Khosroshahi, S. F. Z., & Mohammadloo, H. B. (2010). Determination of materials parameters under dynamic loading. Part I: Experiments and simulations. Computational Materials Science, 49(2), 192-200.

11. Majzoobi, G. H., Khosroshahi, S. F. Z., & Mohammadloo, H. B. (2010). Determination of materials parameters under dynamic loading: Part II: Optimization. Computational Materials Science, 49(2), 201-208.

12. Dorogoy, A., & Rittel, D. (2009). Determination of the Johnson–Cook material parameters using the SCS specimen. Experimental mechanics, 49(6), 881.

13. Shrot, A., & Bäker, M. (2012). Determination of Johnson–Cook parameters from machining simulations. Computational Materials Science, 52(1), 298-304.

14. Umbrello, D., M'saoubi, R., & Outeiro, J. C. (2007). The influence of Johnson–Cook material constants on finite element simulation of machining of AISI 316L steel. International Journal of Machine Tools and Manufacture, 47(3-4), 462-470.

15. Agmell, M., Ahadi, A., & Ståhl, J. E. (2014). Identification of plasticity constants from orthogonal cutting and inverse analysis. Mechanics of Materials, 77, 43-51.

16. Oxley, P. L. B. (1989). The mechanics of machining: an analytical approach to assesing machinability. Ellis Horwood.

17. Özel, T., & Zeren, E. (2006). A methodology to determine work material flow stress and tool-chip interfacial friction properties by using analysis of machining. Journal of manufacturing science and Engineering, 128(1), 119-129.

18. Tounsi, N., Vincenti, J., Otho, A., & Elbestawi, M. A. (2002). From the basic mechanics of orthogonal metal cutting toward the identification of the constitutive equation. International Journal of Machine Tools and Manufacture, 42(12), 1373-1383.

19. Lalwani, D. I., Mehta, N. K., & Jain, P. K. (2009). Extension of Oxley's predictive machining theory for Johnson and Cook flow stress model. Journal of materials processing technology, 209(12-13), 5305-5312.

20. Adibi-Sedeh, A. H., Madhavan, V., & Bahr, B. (2003). Extension of Oxley's analysis of machining to use different material models. Journal of manufacturing science and engineering, 125(4), 656-666.

21. Komanduri, R., & Hou, Z. B. (2000). Thermal modeling of the metal cutting process: Part I—Temperature rise distribution due to shear plane heat source. International Journal of Mechanical Sciences, 42(9), 1715-1752.

22. Komanduri, R., & Hou, Z. B. (2001). Thermal modeling of the metal cutting process—Part II: temperature rise distribution due to frictional heat source at the tool–chip interface. International Journal of Mechanical Sciences, 43(1), 57-88.

23. Komanduri, R., & Hou, Z. B. (2001). Thermal modeling of the metal cutting process—Part III: temperature rise distribution due to the combined effects of shear plane heat source and the tool–chip interface frictional heat source. International Journal of Mechanical Sciences, 43(1), 89-107.

24. Karpat, Y., & Özel, T. (2006). Predictive analytical and thermal modeling of orthogonal cutting process—part I: predictions of tool forces, stresses, and temperature distributions. Journal of manufacturing science and engineering, 128(2), 435-444.

25. Karpat, Y., & Özel, T. (2006). Predictive analytical and thermal modeling of orthogonal cutting process—part II: effect of tool flank wear on tool forces, stresses, and temperature distributions. Journal of manufacturing science and engineering, 128(2), 445-453.

26. Aydın, M. (2016). Cutting temperature analysis considering the improved Oxley's predictive machining theory. Journal of the Brazilian Society of Mechanical Sciences and Engineering, 38(8), 2435-2448.

27. Bai, W., Sun, R., Roy, A., & Silberschmidt, V. V. (2017). Improved analytical prediction of chip formation in orthogonal cutting of titanium alloy Ti6Al4V. International Journal of Mechanical Sciences, 133, 357-367.

28. Pan, Z., Feng, Y., Ji, X., & Liang, S. Y. (2018). Turning induced residual stress prediction of AISI 4130 considering dynamic recrystallization. Machining Science and Technology, 22(3), 507-521.

29. Fergani, O., Lazoglu, I., Mkaddem, A., El Mansori, M., & Liang, S. Y. (2014). Analytical modeling of residual stress and the induced deflection of a milled thin plate. The International Journal of Advanced Manufacturing Technology, 75(1-4), 455-463.

30. Feng, Y. (2019). Analytical performance analysis in laser-assisted and ultrasonic vibration-assisted milling (Doctoral dissertation, Georgia Institute of Technology).

31. Elias, C. N., Meyers, M. A., Valiev, R. Z., & Monteiro, S. N. (2013). Ultrafine grained titanium for biomedical applications: An overview of performance. Journal of Materials Research and Technology, 2(4), 340-350.re

32. Latysh, V., Krallics, G., Alexandrov, I., & Fodor, A. (2006). Application of bulk nanostructured materials in medicine. Current Applied Physics, 6(2), 262-266.

33. Stolyarov, V. V., Zhu, Y. T., Alexandrov, I. V., Lowe, T. C., & Valiev, R. Z. (2001). Influence of ECAP routes on the microstructure and properties of pure Ti. Materials Science and Engineering: A, 299(1-2), 59-67.

34. Morehead, M. D., & Zhu, Y. T. (2000). Experimental investigation of the machinability of equal channel angular pressing processed commercially pure titanium. Society of Manufacturing Engineers.

35. Lapovok, R., Molotnikov, A., Levin, Y., Bandaranayake, A., & Estrin, Y. (2012). Machining of coarse grained and ultra fine grained titanium. Journal of materials science, 47(11), 4589-4594.

36. Stolyarov, V. V., Zhu, Y. T., Lowe, T. C., & Valiev, R. Z. (2001). Microstructure and properties of pure Ti processed by ECAP and cold extrusion. Materials Science and Engineering: A, 303(1-2), 82-89.

37. Horita, Z., Fujinami, T., & Langdon, T. G. (2001). The potential for scaling ECAP: effect of sample size on grain refinement and mechanical properties. Materials Science and Engineering: A, 318(1-2), 34-41.

38. Stolyarov, V. V., Zhu, Y. T., Alexandrov, I. V., Lowe, T. C., & Valiev, R. Z. (2001). Influence of ECAP routes on the microstructure and properties of pure Ti. Materials Science and Engineering: A, 299(1-2), 59-67.

39. Stolyarov, V. V., Zhu, Y. T., Alexandrov, I. V., Lowe, T. C., & Valiev, R. Z. (2003). Grain refinement and properties of pure Ti processed by warm ECAP and cold rolling. Materials Science and Engineering: A, 343(1-2), 43-50.

40. Szost, B. A., Terzi, S., Martina, F., Boisselier, D., Prytuliak, A., Pirling, T., ... & Jarvis, D. J. (2016). A comparative study of additive manufacturing techniques: Residual stress and microstructural analysis of CLAD and WAAM printed Ti–6Al–4V components. Materials & Design, 89, 559-567.

41. Gong, H., Rafi, K., Gu, H., Starr, T., & Stucker, B. (2014). Analysis of defect generation in Ti–6Al–4V parts made using powder bed fusion additive manufacturing processes. Additive Manufacturing, 1, 87-98.

42. Heigel, J. C., Michaleris, P., & Palmer, T. A. (2015). In situ monitoring and characterization of distortion during laser cladding of Inconel® 625. Journal of Materials Processing Technology, 220, 135-145.

43. Dunbar, A. J., Denlinger, E. R., Gouge, M. F., & Michaleris, P. (2016). Experimental validation of finite element modeling for laser powder bed fusion deformation. Additive Manufacturing, 12, 108-120.

44. Roberts, I. A., Wang, C. J., Esterlein, R., Stanford, M., & Mynors, D. J. (2009). A three-dimensional finite element analysis of the temperature field during laser melting of metal powders in additive layer manufacturing. International Journal of Machine Tools and Manufacture, 49(12-13), 916-923.

45. Fu, C. H., & Guo, Y. B. (2014). Three-dimensional temperature gradient mechanism in selective laser melting of Ti-6Al-4V. Journal of Manufacturing Science and Engineering, 136(6), 061004.

46. Labudovic, M., Hu, D., & Kovacevic, R. (2003). A three-dimensional model for direct laser metal powder deposition and rapid prototyping. Journal of materials science, 38(1), 35-49.

47. Hao, M., & Sun, Y. (2013). A FEM model for simulating temperature field in coaxial laser cladding of TI6AL4V alloy using an inverse modeling approach. International Journal of Heat and Mass Transfer, 64, 352-360.

48. Criales, L. E., Arısoy, Y. M., & Özel, T. (2016). Sensitivity analysis of material and process parameters in finite element modeling of selective laser melting of Inconel

625. The International Journal of Advanced Manufacturing Technology, 86(9-12), 2653-2666.

49. Papadakis, L., Loizou, A., Risse, J., Bremen, S., & Schrage, J. (2014). A computational reduction model for appraising structural effects in selective laser melting manufacturing: a methodical model reduction proposed for time-efficient finite element analysis of larger components in Selective Laser Melting. Virtual and Physical Prototyping, 9(1), 17-25.

50. Bikas, H., Stavropoulos, P., & Chryssolouris, G. (2016). Additive manufacturing methods and modelling approaches: a critical review. The International Journal of Advanced Manufacturing Technology, 83(1-4), 389-405.

51. Schoinochoritis, B., Chantzis, D., & Salonitis, K. (2017). Simulation of metallic powder bed additive manufacturing processes with the finite element method: A critical review. Proceedings of the Institution of Mechanical Engineers, Part B: Journal of Engineering Manufacture, 231(1), 96-117.

52. Rosenthal, D. (1946). The theory of moving sources of heat and its application of metal treatments. Transactions of ASME, 68, 849-866.

53. Tan, H., Chen, J., Zhang, F., Lin, X., & Huang, W. (2010). Process analysis for laser solid forming of thin-wall structure. International Journal of Machine Tools and Manufacture, 50(1), 1-8.

54. Van Elsen, M., Baelmans, M., Mercelis, P., & Kruth, J. P. (2007). Solutions for modelling moving heat sources in a semi-infinite medium and applications to laser material processing. International Journal of heat and mass transfer, 50(23-24), 4872-4882.

55. Carslaw, H., & Jaeger, J. (1990) Conduction of Heat in Solids. Oxford Science Publication.

56. Peyre, P., Aubry, P., Fabbro, R., Neveu, R., & Longuet, A. (2008). Analytical and numerical modelling of the direct metal deposition laser process. Journal of Physics D: Applied Physics, 41(2), 025403.

57. Yang, Y., Knol, M. F., Van Keulen, F., & Ayas, C. (2018). A semi-analytical thermal modelling approach for selective laser melting. Additive Manufacturing, 21, 284-297.

58. Bruna-Rosso, C., Demir, A. G., & Previtali, B. (2018). Selective laser melting finite element modeling: Validation with high-speed imaging and lack of fusion defects prediction. Materials & Design, 156, 143-153.

59. Mukherjee, T., & DebRoy, T. (2018). Mitigation of lack of fusion defects in powder bed fusion additive manufacturing. Journal of Manufacturing Processes, 36, 442-449.

60. Wei, P., Wei, Z., Chen, Z., He, Y., & Du, J. (2017). Thermal behavior in single track during selective laser melting of AlSi10Mg powder. Applied Physics A, 123(9), 604.

61. Chen, Z., Xiang, Y., Wei, Z., Wei, P., Lu, B., Zhang, L., & Du, J. (2018). Thermal dynamic behavior during selective laser melting of K418 superalloy: numerical simulation and experimental verification. Applied Physics A, 124(4), 313.

62. Körner, C., Attar, E., & Heinl, P. (2011). Mesoscopic simulation of selective beam melting processes. Journal of Materials Processing Technology, 211(6), 978-987.

63. Xiang, Y., Zhang, S., Wei, Z., Li, J., Wei, P., Chen, Z., ... & Jiang, L. (2018). Forming and defect analysis for single track scanning in selective laser melting of Ti6Al4V. Applied Physics A, 124(10), 685.

64. Tan, J. L., Tang, C., & Wong, C. H. (2018). A computational study on porosity evolution in parts produced by selective laser melting. Metallurgical and Materials Transactions A, 49(8), 3663-3673.

65. Bayat, M., Mohanty, S., & Hattel, J. H. (2019). Multiphysics modelling of lack-of-fusion voids formation and evolution in IN718 made by multi-track/multi-layer L-PBF. International Journal of Heat and Mass Transfer, 139, 95-114.

66. AlFaify, A., Hughes, J., & Ridgway, K. (2019). Controlling the porosity of 316L stainless steel parts manufactured via the powder bed fusion process. Rapid Prototyping Journal, 25(1), 162-175.

67. Tapia, G., Elwany, A. H., & Sang, H. (2016). Prediction of porosity in metal-based additive manufacturing using spatial Gaussian process models. Additive Manufacturing, 12, 282-290.

68. Khanzadeh, M., Chowdhury, S., Tschopp, M. A., Doude, H. R., Marufuzzaman, M., & Bian, L. (2019). In-situ monitoring of melt pool images for porosity prediction in directed energy deposition processes. IISE Transactions, 51(5), 437-455.

69. Garg, A., Lam, J. S. L., & Savalani, M. M. (2015). A new computational intelligence approach in formulation of functional relationship of open porosity of the additive manufacturing process. The International Journal of Advanced Manufacturing Technology, 80(1-4), 555-565.

70. Tang, M., Pistorius, P. C., & Beuth, J. L. (2017). Prediction of lack-of-fusion porosity for powder bed fusion. Additive Manufacturing, 14, 39-48.

71. Fergani, O., Berto, F., Welo, T., & Liang, S. Y. (2017). Analytical modelling of residual stress in additive manufacturing. Fatigue & Fracture of Engineering Materials & Structures, 40(6), 971-978.

72. Denlinger, E. R., & Michaleris, P. (2016). Effect of stress relaxation on distortion in additive manufacturing process modeling. Additive Manufacturing, 12, 51-59.

73. Biegler, M., Graf, B., & Rethmeier, M. (2018). In-situ distortions in LMD additive manufacturing walls can be measured with digital image correlation and predicted using numerical simulations. Additive Manufacturing, 20, 101-110.

74. Afazov, S., Denmark, W. A., Toralles, B. L., Holloway, A., & Yaghi, A. (2017). Distortion prediction and compensation in selective laser melting. Additive Manufacturing, 17, 15-22.

75. Zaeh, M. F., & Branner, G. (2010). Investigations on residual stresses and deformations in selective laser melting. Production Engineering, 4(1), 35-45.

76. Afazov, S., Denmark, W. A., Toralles, B. L., Holloway, A., & Yaghi, A. (2017). Distortion prediction and compensation in selective laser melting. Additive Manufacturing, 17, 15-22.

77. Li, C., Fu, C. H., Guo, Y. B., & Fang, F. Z. (2016). A multiscale modeling approach for fast prediction of part distortion in selective laser melting. Journal of materials processing technology, 229, 703-712.

78. Paul, R., Anand, S., & Gerner, F. (2014). Effect of thermal deformation on part errors in metal powder based additive manufacturing processes. Journal of Manufacturing Science and Engineering, 136(3), 031009.

79. Ivester, R. W., Kennedy, M., Davies, M., Stevenson, R., Thiele, J., Furness, R., & Athavale, S. (2000). Assessment of machining models: progress report. Machining Science and Technology, 4(3), 511-538.

80. Everton, S. K., Hirsch, M., Stravroulakis, P., Leach, R. K., & Clare, A. T. (2016). Review of in-situ process monitoring and in-situ metrology for metal additive manufacturing. Materials & Design, 95, 431-445.

81. Mani, M., Feng, S., Lane, B., Donmez, A., Moylan, S., & Fesperman, R. (2015). Measurement science needs for real-time control of additive manufacturing powder bed fusion processes.

82. Slotwinski, J. A., Garboczi, E. J., & Hebenstreit, K. M. (2014). Porosity measurements and analysis for metal additive manufacturing process control. Journal of research of the National Institute of Standards and Technology, 119, 494.

83. Li, B., Wang, X., Hu, Y., & Li, C. (2011). Analytical prediction of cutting forces in orthogonal cutting using unequal division shear-zone model. The International Journal of Advanced Manufacturing Technology, 54(5-8), 431-443.

84. Moufki, A., Devillez, A., Dudzinski, D., & Molinari, A. (2004). Thermomechanical modelling of oblique cutting and experimental validation. International Journal of Machine Tools and Manufacture, 44(9), 971-989.

85. Ning, J., & Liang, S. Y. (2018). Model-driven determination of Johnson-Cook material constants using temperature and force measurements. The International Journal of Advanced Manufacturing Technology, 97(1-4), 1053-1060.

86. Ning, J., & Liang, S. Y. (2019). Inverse identification of Johnson-Cook material constants based on modified chip formation model and iterative gradient search using temperature and force measurements. The International Journal of Advanced Manufacturing Technology, 102(9-12), 2865-2876.

87. Ning, J., & Liang, S. (2018). Prediction of temperature distribution in orthogonal machining based on the mechanics of the cutting process using a constitutive model. Journal of Manufacturing and Materials Processing, 2(2), 37.

88. Ning, J., & Liang, S. Y. (2019). Predictive Modeling of Machining Temperatures with Force–Temperature Correlation Using Cutting Mechanics and Constitutive Relation. Materials, 12(2), 284.

89. Klocke, F., Lung, D., & Buchkremer, S. (2013). Inverse identification of the constitutive equation of Inconel 718 and AISI 1045 from FE machining simulations. Procedia Cirp, 8, 212-217.

90. Özel, T., & Karpat, Y. (2007). Identification of constitutive material model parameters for high-strain rate metal cutting conditions using evolutionary computational algorithms. Materials and manufacturing processes, 22(5), 659-667.

91. Ning, J., & Liang, S. (2018). Evaluation of an analytical model in the prediction of machining temperature of AISI 1045 steel and AISI 4340 steel. Journal of Manufacturing and Materials Processing, 2(4), 74.

92. Ning, J., & Liang, S. Y. (2019). A comparative study of analytical thermal models to predict the orthogonal cutting temperature of AISI 1045 steel. The International Journal of Advanced Manufacturing Technology, 102(9-12), 3109-3119.

93. Ning, J., Nguyen, V., Huang, Y., Hartwig, K. T., & Liang, S. Y. (2018). Inverse determination of Johnson–Cook model constants of ultra-fine-grained titanium based on chip formation model and iterative gradient search. The international journal of advanced manufacturing technology, 99(5-8), 1131-1140.

94. Ning, J., Nguyen, V., & Liang, S. Y. (2019). Analytical modeling of machining forces of ultra-fine-grained titanium. The International Journal of Advanced Manufacturing Technology, 101(1-4), 627-636.

95. Ning, J., Nguyen, V., Huang, Y., Hartwig, K. T., & Liang, S. Y. (2019). Constitutive modeling of ultra-fine-grained titanium flow stress for machining temperature prediction. Bio-Design and Manufacturing, 2(3), 153-160.

96. Ning, J., Sievers, D. E., Garmestani, H., & Liang, S. Y. (2019). Analytical Modeling of In-Process Temperature in Powder Bed Additive Manufacturing Considering Laser

Power Absorption, Latent Heat, Scanning Strategy, and Powder Packing. Materials, 12(5), 808.

97. Ning, J., Sievers, D. E., Garmestani, H., & Liang, S. Y. (2019). Analytical Thermal Modeling of Metal Additive Manufacturing by Heat Sink Solution. Materials, 12(16), 2568.

98. Dilip, J. J. S., Zhang, S., Teng, C., Zeng, K., Robinson, C., Pal, D., & Stucker, B. (2017). Influence of processing parameters on the evolution of melt pool, porosity, and microstructures in Ti-6Al-4V alloy parts fabricated by selective laser melting. Progress in Additive Manufacturing, 2(3), 157-167.

99. Ning, J., Mirkoohi, E., Dong, Y., Sievers, D. E., Garmestani, H., & Liang, S. Y. (2019). Analytical modeling of 3D temperature distribution in selective laser melting of Ti-6Al-4V considering part boundary conditions. Journal of Manufacturing Processes, 44, 319-326.

100. Ning, J., Sievers, D. E., Garmestani, H., & Liang, S. Y. (2019). Analytical modeling of in-process temperature in powder feed metal additive manufacturing considering heat transfer boundary condition. International Journal of Precision Engineering and Manufacturing-Green Technology. (Accepted)

101. Ning, J., Sievers, D. E., Garmestani, H., & Liang, S. Y. (2019). Analytical modeling of transient temperature in powder feed metal additive manufacturing during heating and cooling stages. Applied Physics A, 125(8), 496.

102. Ning, J., Sievers, D. E., Garmestani, H., & Liang, S. Y. (2019). Analytical thermal modeling of powder bed metal additive manufacturing considering boundary heat transfer and powder packing and size distribution. CIRP Journal of Manufacturing Science and Technology. (Under Review)

103. Feng, Y. T., Han, K., & Owen, D. R. J. (2003). Filling domains with disks: an advancing front approach. International journal for numerical methods in engineering, 56(5), 699-713.

104. Moser, D., Pannala, S., & Murthy, J. (2016). Computation of effective thermal conductivity of powders for selective laser sintering simulations. Journal of Heat Transfer, 138(8), 082002.

105. Ning, J., Wang, W., Zamorano, B., & Liang, S. Y. (2019). Analytical modeling of lack-of-fusion porosity in metal additive manufacturing. Applies Physics A. (Accepted)

106. Ning, J., Sievers, D. E., Garmestani, H., & Liang, S. Y. (2019). Analytical Modeling of Part Porosity in Metal Additive Manufacturing. International Journal of Mechanical Sciences. (Under Review)

107. Aboulkhair, N. T., Everitt, N. M., Ashcroft, I., & Tuck, C. (2014). Reducing porosity in AlSi10Mg parts processed by selective laser melting. Additive Manufacturing, 1, 77-86.

108. Mindt, H. W., Desmaison, O., Megahed, M., Peralta, A., & Neumann, J. (2018). Modeling of powder bed manufacturing defects. Journal of Materials Engineering and Performance, 27(1), 32-43.

109. Ning, J., Sievers, D. E., Garmestani, H., & Liang, S. Y. (2019). Analytical modeling of in-situ deformation of part and substrate in laser cladding additive manufacturing of Inconel 625. Journal of Manufacturing Processes. (Under Review)

110. Mishkevich, V., & Suhir, E. (1993). Simplified approach to the evaluation of thermally induced stresses in bi-material structures. Structural Analysis in Microelectronics and Fiber Optics, 563-572.

111. Tsai, M. Y., Hsu, C. H., & Han, C. N. (2004). A note on Suhir's solution of thermal stresses for a die-substrate assembly. Journal of Electronic Packaging, 126(1), 115-119.

112. INCONEL alloy 625, Special Metal Company, http://www.specialmetals.com/assets/smc/documents/alloys/inconel/inconel-alloy-625.pdf (Accessed October 2019).

113. Saif, M. T. A., Hui, C. Y., & Zehnder, A. T. (1993). Interface shear stresses induced by non-uniform heating of a film on a substrate. Thin Solid Films, 224(2), 159-167.

114. Ning, J., Praniewicz, M., Wang, W., Dobbs, J. R., & Liang, S. Y. Analytical Modeling of Part Distortion in Metal Additive Manufacturing. The International Journal of Advanced Manufacturing Technology. (Under Review)

115. McDowell, D. L. (1997). An approximate algorithm for elastic-plastic two-dimensional rolling/sliding contact. Wear, 211(2), 237-246.

116. Love, A. E. H. (2013). A treatise on the mathematical theory of elasticity. Cambridge university press.